

Ultrasonic Characterization and Defect Detection in Piezoelectric Materials

DISSERTATION

zur Erlangung des Grades eines Doktors
der Naturwissenschaften

vorgelegt von

M. Sc. Md. Anowarul Habib

eingereicht bei der Naturwissenschaftlich-Technischen Fakultät
der Universität Siegen

Siegen, 2012

Gutachter:

Prof. Dr. Ullrich Pietsch

Prof. Dr. Xin Jiang

Prüfer:

Prof. Dr.-Ing. Claus-Peter Fritzen

Prof. Dr. Otfried Gühne

Prof. Dr.-Ing. Peter Haring Bolívar

Tag der mündlichen Prüfung: 07.03.2013

Abstract

Aluminum nitride (AlN) is a piezoelectric semiconductor material used for optoelectronic devices, high-frequency acoustic filters, resonators, and piezoelectric transducers for structural health monitoring due to their wide band gap, chemical and mechanical stability, dielectric properties, and relatively large values of its elastic constants. On the other hand, lead zirconate titanate (PZT) ceramics are also used in excitation and detection of acoustic waves in aircraft integrated structures for structural health monitoring and nondestructive testing. Prior to any potential device application it is necessary to characterize the mechanical properties of those materials.

In addition to the polycrystalline materials AlN, PZT, and single crystal lithium niobate (LiNbO_3) has been studied in the present thesis in view of its piezoelectric and high-frequency elastic properties. LiNbO_3 is currently intensively used for piezoelectric, as well as electro-optic and nonlinear optical applications. Although the focusing of thermal phonon has been studied previously in LiNbO_3 and its elastic and piezoelectric constants have been determined in many previous studies, its acoustic properties are still not completely explored.

In the first part of the thesis scanning acoustic microscopy has been used to determine the mechanical properties of AlN thin films and PZT ceramics. AlN thin films were grown using the reactive RF-magnetron sputtering technique. The microstructure, surface morphology, and chemical composition of the AlN thin films were determined. Later on, the Coulomb coupling technique has been applied to determine the acoustic velocities and transport properties of ultrasonic waves in PZT and LiNbO_3 in order to assess the feasibility of this technique.

The longitudinal, skimming longitudinal, transversal, and surface acoustic wave velocities and the corresponding elastic constants were determined in AlN as well as in PZT ceramics. AlN does not grow as a single crystal so that LiNbO_3 single crystals have been employed to demonstrate the generation and detection of surface acoustic waves (SAW's) for defect characterization in piezoelectric materials.

In the second part of the thesis, the developed scheme has been applied to image the transport properties of bulk and guided acoustic waves travelling in PZT. A delta pulse, broad band signal excites both longitudinal and transverse bulk waves, and metamorphosis of bulk wave into Lamb waves was sequentially monitored.

In further studies, ultrasonic imaging with high temporal and spatial resolution was conducted on LiNbO_3 . The imaging is performed with switched sinusoidal excitation and quadrature detection from which the magnitude and phase are derived. The wavelengths of surface skimming longitudinal waves and SAW's are both determined from the observed phase rotation as a function of position. This technique also used to study the influence of a surface defects on the scattering of SAW propagating on the surface of the LiNbO_3 crystal. Artificial defects employed for interaction with the waves were produced by deposition of silver paint on the surface. These defects are both absorptive and scattering. The scattering and attenuation of SAW's are studied by imaging in vector contrast. The interaction allows a clear differentiation of volume waves skimming the surface and guided waves traveling at the surface. The thesis, hence, describes the use of the local electric field probe technique to study the structure of piezoelectric materials by acoustic methods.

Zusammenfassung

Aluminium-Nitrid (AlN) ist ein piezoelektrisches Halbleitermaterial, welches über eine große Bandlücke sowie über gute dielektrische Eigenschaften sowie hohe elastische Konstanten verfügt. Es ist chemisch und mechanisch stabil und findet Anwendungen in optoelektronischen Bauelementen, akustischen Hochfrequenz-Filtern sowie Sensoren für strukturelle Defekte. Neben AlN werden zunehmend auch Blei-Zirkonat-Titanat (PZT) Keramiken für die Erzeugung und Detektion von Oberflächenwellen auf empfindlichen Oberflächen, z.B. im Flugzeugbau, eingesetzt, um strukturelle Defekte zu detektieren. Vor der Anwendung in Bauelementen ist es jedoch erforderlich, die grundlegenden mechanischen Eigenschaften sowohl von AlN als auch PZT zu charakterisieren.

Zusätzlich zu den polykristallinen Materialien AlN und PZT wurde in der vorliegenden Arbeit auch Einkristall LiNbO_3 in Hinblick auf seine piezoelektrischen und hochfrequenten elastischen Eigenschaften untersucht. LiNbO_3 wird gegenwärtig intensiv genutzt unter anderem für piezoelektrische, sowie elektrooptische und nichtlinear-optische Anwendungen. Obwohl die Fokussierung thermischer Phononen in anisotropen Kristallen schon früher anhand von LiNbO_3 untersucht wurde und seine elastischen und piezoelektrischen Konstanten in vielen früheren Studien bestimmt wurden, sind seine akustischen Eigenschaften noch immer nicht vollständig erforscht.

Der erste Teil der Arbeit befasst sich mit der Untersuchung der mechanischen Eigenschaften von dünnen AlN Schichten und PZT-Keramiken mittels akustischer Mikroskopie (engl. Scanning Acoustic Microscopy, SAM). Die verwendeten AlN Schichten wurden mittels reaktivem RF-Magnetron Sputtern hergestellt. Untersuchungen zur Bestimmung der Mikrostruktur, Oberflächenmorphologie und der chemischen Zusammensetzung wurden durchgeführt. Anschließend werden zunächst die Schallgeschwindigkeiten und Transporteigenschaften von Ultraschallwellen mittels Coulomb-Kopplung an PZT und LiNbO_3 untersucht, um die Einsatzmöglichkeiten dieser Technik zu validieren.

Für PZT und AlN werden so die Schallgeschwindigkeiten der longitudinalen, transversalen und streifend propagierenden (englisch "skimming") longitudinalen Volumenwellen sowie der Oberflächenwellen und aus diesen wiederum die elastischen Konstanten der Materialien bestimmt. Da AlN nicht als einkristalline Schicht abgeschieden

werden kann, wurde anhand eines LiNbO_3 Einkristalls demonstriert, dass Oberflächendefekte mittels Oberflächenwellen in Piezoelektrika detektiert werden können.

Im zweiten Teil der Arbeit wird die entwickelte Methode angewandt, um die Transporteigenschaften von Volumen- wie auch geführten akustischen Wellen in PZT sichtbar zu machen. Ein Delta-Puls Signal mit breitem Frequenzspektrum regt sowohl longitudinale als auch transversale Volumen-Wellen an. Deren Umwandlung in Lamb-Wellen wird dokumentiert.

In weiteren Untersuchungen wurden Ultraschallaufnahmen mit hoher zeitlicher und räumlicher Auflösung an LiNbO_3 -Kristallen erstellt. Dazu dient gepulste sinusförmige Anregung und Quadratur-Detektion, sodass Magnituden- und Phasenbilder generiert werden können. Die Wellenlänge der oberflächennahen Longitudinalwellen und Oberflächenwellen können beide anhand der Phasenrotation als Funktion der Position bestimmt werden. Diese Technik wird ebenfalls verwendet, um den Einfluss oberflächennaher Fehlstellen auf die Zerstreuung von Oberflächenwellen bei LiNbO_3 Einkristallen zu untersuchen. Künstliche Fehlstellen wurden mit Hilfe von Silberpaste, die auf die Oberfläche aufgebracht wurde, erzeugt. Diese Fehlstellen wirken sowohl absorbierend als auch zerstreud. Die Zerstreuung und das Abklingverhalten der Oberflächenwellen wurden anhand des aufgezeichneten Vektorkontrastes untersucht. Die Wechselwirkung erlaubt die eindeutige Unterscheidung von oberflächennahen Körperwellen und geführten Wellen auf der Oberfläche. Die vorliegende Arbeit zeigt somit neue Ansätze zur Untersuchung realer Strukturen piezoelektrischer Materialien mittels akustischer Methoden.

Table of Contents

Abstract.....	ii
Zusammenfassung.....	i
Scope and Outline of the Thesis	5
Introduction.....	7
1 Theory.....	11
1.1 Stress and Strain.....	11
1.2 Christoffel Equation	15
1.3 Normal modes in Unbounded Media	15
1.4 Plane Waves in Unbounded Isotropic Media.....	17
1.5 Plane Waves in Unbounded Anisotropic Media (in contracted notation).....	18
1.6 Acoustic wave equation in piezoelectric media	19
2 Methodology: Scanning Acoustic Microscope.....	21
2.1 Scanning Acoustic Microscope.....	22
2.2 Principles of Scanning Acoustic Microscopy	25
2.3 Theory of Acoustic Material Signature Curve	26
2.4 Ultrasonic Characterization of c-axis Oriented Polycrystalline AlN Film Using Scanning Acoustic Microscopy.....	29
2.4.1 Introduction.....	29
2.4.2 Experiment.....	31
2.4.3 Sample Preparation and Scanning Electron Microscopy.....	31
2.4.4 Atomic Force Microscopy	32
2.4.5 X-ray Diffraction	33
2.4.6 Nanoindentation.....	34
2.4.7 Results of Scanning Acoustic Microscopy	36
2.4.8 Acoustic Dispersion Relation for AlN Film	39
2.4.9 Conclusions.....	41

2.5	Mechanical Characterization of Sintered Piezoelectric Ceramic Material Using Scanning Acoustic Microscope.....	42
2.5.1	Introduction.....	42
2.5.2	Experimental Technique	45
2.5.3	Scanning Acoustic Microscopy	45
2.5.4	Scanning Electron Microscopy Analysis	46
2.5.5	Energy Dispersive X-ray Spectroscopy	49
2.5.6	Results and Discussions.....	49
2.5.7	Conclusions.....	55
3	Methodology: Coulomb Coupling.....	56
3.1	Coulomb Coupling	57
3.2	Experimental Setup for Coulomb Coupling Excitation and Detection.....	58
3.3	Quadrature Detection Scheme.....	60
3.4	Experimental Setup for Local Electrical Field Probe Technique.....	61
4	Imaging of Acoustic Waves in Piezoelectric Ceramics by Coulomb Coupling.....	65
4.1	Introduction	65
4.2	Experimental Results and Discussion	66
4.3	Conclusion.....	72
5	Vector Contrast Imaging of Surface Acoustic Waves by Local Electric Field Probes	73
5.1	Introduction	73
5.2	Results and Discussions	75
5.3	Conclusions.....	81
6	Scattering and Attenuation of Surface Acoustic Waves and Surface Skimming Longitudinal Polarized Bulk Waves Imaged by Coulomb Coupling	82
6.1	Introduction	82
6.2	Experimental Setup	83
6.3	Results and Discussions	86

Table of Contents

6.4	Conclusion.....	89
7	Conclusion and Outlook	90
	Acknowledgements.....	96
	Eidesstattliche Erklärung	109

List of Abbreviations

Structural health monitoring	SHM
Surface skimming longitudinal waves	SSLW
Leaky surface acoustic waves	LSAW
Surface acoustic wave	SAW
Fast transversal	F-T
Slow transversal	S-T
Acoustic material signature curves	AMS
Inter-digital transducer	IDT
Aluminum nitride	AlN
Lead zirconate titanate	PZT
Atomic force microscopy	AFM
Scanning electron microscopy	SEM
Scanning acoustic microscopy	SAM
Nondestructive testing	NDT
Scanning laser Doppler vibrometers	SLDV
Energy dispersive X-ray spectroscopy	EDX
Radio frequency	RF

Scope and Outline of the Thesis

The ultimate thrust of this thesis is to demonstrate the propagation of acoustic waves in piezoelectric materials by scanning acoustic microscopy and surface excitation and detection via the Coulomb field associated with those waves. The elastic properties of the piezoelectric materials are evaluated using scanning acoustic microscopy. On the other hand, a scanning contact excitation and similar detection scheme have been employed for imaging of the propagation of acoustic waves in piezoelectric materials. The samples investigated in this thesis are drawn from different crystal classes, showing piezoelectric influence is a widespread phenomenon and not restricted to any particular crystal symmetry. This recipe is then explicitly applied to generate and detect bulk and surface acoustic waves in piezoelectric materials. The chapters of the thesis are organized as follows.

Chapter I: The first chapter of this manuscript describes a brief general introduction into acoustic waves in piezoelectric materials, which serves as a preliminary preview of the research performed.

Chapter II: Chapter II contains a digest of acoustic wave propagation in piezoelectric isotropic and anisotropic media. The main scope is to document those formulae which are essential ingredients to understand the acoustic wave propagation in piezoelectric media.

Chapter III: This chapter begins with a brief introduction into scanning acoustic microscopy, their aspects in material science and theoretical formulation of acoustic material signature curve followed by results obtained on aluminum nitride thin films and lead zirconate titanate samples.

Chapter IV: This chapter delivers the basic operational principle of the quadrature detection scheme and local electrical field probe technique which is used in excitation and detection of bulk and surface acoustic waves in piezoelectric materials. This recipe is then explicitly applied in the two different kinds of sample: i) Lead zirconate titanate (PZT) ii) LiNbO_3 single crystal.

Chapter V: Chapter V represents the method which was developed to study the generation and evolution of acoustic waves propagating in lead zirconate titanate sintered material using the Coulomb coupling technique.

Chapter VI: Here the vector contrast imaging of surface acoustic waves by local electric field probes will be explained. This chapter will also establish the link between the generation and detection of surface acoustic waves and their scattering and attenuation of surface acoustic waves due a surface flaw on the sample surface.

Chapter VII: This chapter demonstrates the effect of the surface wave propagation due to surface defect on the LiNbO_3 single crystal.

Chapter VIII: Conclusions and outlook.

1 Introduction

The development of piezoelectric thin films has been used for fabrication of surface acoustic waves devices, electron emission devices, photonic application and structural health monitoring (SHM) at high temperatures and many others potential application. There is considerable need for *in situ* material property change inspections, process monitoring and characterization of function of resonators, filters and transformers at high temperature above 400°C.

In order to achieve the above application, the research project was designed to develop such a multi layer thin film (AlN / Nanodiamond / γ -TiAl) system which can also act as a diffusion barrier, corrosion protection, and thermal insulation and has a potential to be used as a sensor for detecting surface aberration like fatigue, cracking, and delamination. This acoustic sensor will be employed for detecting any kind of surface flaws on the surface or delamination on the multi layer films. Use of diamond film, as a substrate / interlayer for acoustic wave devices are very desirable because of their high acoustic waves velocity (~11,000 m/s, for the Rayleigh wave), the highest observed among all materials (Benetti *et al.*, 2005).

Aluminum nitride (AlN) is one of the best candidate in piezoelectric materials for novel optoelectronic devices, high bit-rate wireless communication, and in SHM applications due to their wide band-gap, chemical and mechanical stability, dielectric properties, and excellent thermal stability in high temperature (Bergman & Nemanich, 1996). For operating at high temperature, maintaining the temperature stability of the resonance frequency in high temperature is essential for high temperature applications. For piezoelectric thin films, AlN is the most suitable candidate for high temperature applications because it can maintain its piezoelectric properties up to 1150 °C. Thin films of AlN are flexible in implementing acoustic wave devices onto non piezoelectric substrates (like silicon or diamond) with the advantage of the compatibility with electronic and sensoric integration (Okano *et al.*, 1994). In terms of acoustic velocity it is well known that the conventional piezoelectric materials, such as quartz, lithium niobate, and lithium tantalate, suffers from limited SAW propagation velocity (3000–4500 m/s) and are incompatible with monolithic integration technology (Slobodnik, 1973).

It is challenging to grow the high-quality thin, highly c-axis oriented, and low-stressed AlN films on most substrates and on diamond as well. On the other hand, generation and detection of the acoustic waves on AlN films, the thicknesses have to be at least a quarter of the acoustic wavelength. Thinner samples lead to higher operating frequency and restricted to the fabrication of interdigital transducer (IDT) and the misorientation of the crystallites are increasing with the thickness which can hamper the acoustic velocity (Habib *et al.*, 2012c). The film thickness has to be optimized in such a way that the IDT fabrication obstacle can be overcome. The generation and propagation of the acoustic waves are more demanding in SHM due to the fact that high-quality films are necessary for the efficient excitation of the transverse waves, and to exhibit an epitaxial film to preserve both the shearing and extensional motions. Otherwise, the acoustic properties of the films are seriously degraded, which can lead to the annihilation of the piezoelectric activity in the transverse direction. Thin film characterization is necessary to detect surface cracks and determine their size and location for evaluating the functionality of the resonators.

Before the any device applications, it is essential to characterize the mechanical properties of AlN thin films. So that, the present thesis is concerned with determining the elastic properties of AlN thin films and lead zirconate titanate using scanning acoustic microscopy. Surface acoustic waves (SAW) are a prominent tool in the field of surface and interface science for the investigation of surface flaws and delamination on the multi layer film. Later on, the Coulomb coupling technique has been employed for imaging of the ultrasound flux through piezoelectric materials by direct electrical excitation and detection of the waves on the surfaces of lithium niobate single crystals and PZT. This method is also suitable for determining the transport properties of ultrasonic waves traveling in piezoelectric crystals and scattering and attenuation of surface acoustic waves due to defect on the surface of the crystal.

List of publications

All the results presented in this manuscript have been published before as separate articles in scientific journals. The following publication list gives an overview of the articles related to this thesis as well as other articles which are not directly covered here or related to other topics.

Journal publications:

- I. **A. Habib**, A. Shelke, M. Vogel, S. Brand, U. Pietsch, Xin Jiang, and T. Kundu, “Ultrasonic characterization of c-axis oriented polycrystalline AlN film using scanning acoustic microscopy” (under review in Ultrasonics) **(Chapter 3.4)**
- II. **A. Habib**, A. Shelke, U. Pietsch, T. Kundu, “Mechanical characterization of sintered piezo-electric ceramic material using scanning acoustic microscope” Ultrasonics 52(8), 989–995, 2012 **(Chapter 3.5)**
- III. **A. Habib**, A. Shelke, M. Pluta, T. Kundu, U. Pietsch, and W. Grill “Imaging of acoustic waves in piezoelectric ceramics by Coulomb coupling” Japanese Journal of Applied Physics, vol. 51 no. 7, 2012 **(Chapter 5)**
- IV. **A. Habib**, M. Pluta, U. Amjad, A. Shelke, U. Pietsch, T. Kundu, R. Wannemacher, and W. Grill, “Vector contrast imaging of surface acoustic waves by local electric field probes” (not published yet) **(Chapter 6)**
- V. **A. Habib**, A. Shelke, M. Pluta, U. Pietsch, T. Kundu, and W. Grill “Scattering and attenuation of surface acoustic waves and surface skimming longitudinal polarized bulk waves imaged by Coulomb coupling”, AIP Conf. Proc. 1433, 247-250, 2012 **(Chapter 7)**

Papers in conference proceeding:

- I. **A. Habib**, A. Shelke, T. Kundu, U. Pietsch, and W. Grill, “Determination of the transport properties of ultrasonic waves traveling in piezo-electric crystals by imaging with Coulomb coupling” SPIE 8348-40, 2012

- II. A. Shelke, **A. Habib**, U. Amjad, M. Pluta, T. Kundu, U. Pietsch, and W. Grill”
Metamorphosis of bulk waves to Lamb waves in anisotropic piezoelectric crystals”,
SPIE, vol. 7984, 798415, 2011

- III. **A. Habib**, A. Shelke, M. Pluta, T. Kundu, U. Pietsch, and W. Grill, “Holographic
imaging of acoustic waves in piezoelectric ceramics by local electric field probes”,
Proc. of Symposium on Ultrasonic Electronics, 32, 311-312, 2011

- IV. **A. Habib**, U. Amjad, M. Pluta, U. Pietsch, W. Grill. “Surface acoustic wave
generation and detection by Coulomb excitation” SPIE, vol. 7650, 76501T, 2010

- V. **A. Habib**, U. Amjad, M. Pluta, U. Pietsch, W. Grill, Determination of the velocity
of surface acoustic waves with excitation and detection by local electric field probes,
Proc. 20th Int. Congress on Acoustics ICA 2010, 23-27 August, Australia.

2 Theory

In this section the fundamental concepts of stress and strain, and the equations describing the static deformation of an elastic object (Wolfe, 1998, Auld, 1993).

2.1 Stress and Strain

The linear relationship between stress and strain in an elastic solid (see below) can be thought of as a generalization of Hooke's law $f = -kx$ to three dimensional deformable objects. The most straightforward generalization would be to state that stretching or compressing an object in any direction results in an elastic force in the same direction which is proportional to the extension. However, in three dimensions a stretch in one direction changes the dimensions in the perpendicular directions. Moreover, the stretch or compression, as well as the stresses, have to be described by tensors, instead of vectors. Deformations in isotropic solids are characterized using only two constants: Young's modulus, denoted E or Y , and Poisson's ratio, and denoted as ν . The Poisson ratio is the ratio of lateral to axial strain. In order to formulate the equations of balance for elastic objects and define the linear material law more precisely, we start with a discussion of the counterparts of forces and displacements in the equations of elasticity: strain and stress tensors.

There are two kinds of forces acting on a small volume of a body:

a) Volume forces

- f is the volume force density;
- $dF_{vol} = fdV$ is the differential volume force, where dV is the differential volume element.

b) Surface forces

- $\vec{t}(n)$ the vector surface force density, where n is the normal to the differential surface element dA
- $\vec{t}(n)$ is also called the *stress vector*;
- $dF_{surf} = t(\vec{n})dA$ is the differential surface force, acting on the differential surface element dA

Stress tensor

The stress vector, i.e. the force acting on a surface element dA with normal \vec{n} can be expressed in the special form $\vec{t}(n) = \vec{T} \cdot \vec{n}$ where \vec{T} is called the Cauchy stress tensor. 2D tensors are matrices which follow certain transformation rules when we change a coordinate system. Typically these rules follow from the definition of the quantity described by the matrix. In the case of the stress tensor, this can be seen as follows. Let A be the matrix representing a coordinate transformation $\vec{x}' = A\vec{x}$. Under an arbitrary linear change of coordinates, normals are not generally transformed as points or displacement vectors. The correct transformation rule for normals can be derived if we keep in mind that if \vec{n} is the normal to a plane P the transformed normal \vec{n}' should remain perpendicular to the transformed plane P' . Then it is easy to derive that $\vec{n}' = A^{-T}\vec{n}$. Note that in the case of rigid transformations we have $A^{-1} = A^T$, so $A^{-T} = A$. On the other hand force vectors are transformed as all other vectors. Using these considerations (Auld, 1993), we have

$$\begin{aligned}\vec{t}'(n) &= \vec{T}'\vec{n}' \\ A\vec{t}(n) &= \vec{T}A^{-T}\vec{n} \\ \vec{t}(n) &= A^{-1}\vec{T}'A^{-T}\vec{n}\end{aligned}$$

Which implies that $\vec{T} = A^{-1}\vec{T}'A^{-T}$ or $\vec{T}' = A\vec{T}A^T$ so the stress tensor is transformed using $\vec{T}' = A\vec{T}A^T$

Back to the stress tensor.

$$\vec{T} = \begin{pmatrix} \sigma_{11} & \sigma_{12} & \sigma_{13} \\ \sigma_{21} & \sigma_{22} & \sigma_{23} \\ \sigma_{31} & \sigma_{32} & \sigma_{33} \end{pmatrix}, \quad (2.1)$$

Which means that, for example,

$$\vec{T}\vec{i} = \begin{pmatrix} \sigma_{11} & \sigma_{12} & \sigma_{13} \\ \sigma_{21} & \sigma_{22} & \sigma_{23} \\ \sigma_{31} & \sigma_{32} & \sigma_{33} \end{pmatrix} \begin{pmatrix} 1 \\ 0 \\ 0 \end{pmatrix} = \begin{pmatrix} \sigma_{11} \\ \sigma_{21} \\ \sigma_{31} \end{pmatrix} \quad (2.2)$$

We assume that the volume torques will balance, i.e. the volume forces create no net torque. This is generally assumed in elasticity. One can derive from this constraint that T is symmetric and has only six distinct elements.

Symmetric matrices: As an aside, some properties of a general symmetric matrix S are:

- The eigen values are always real (and as a consequence the eigenvectors have real components);
- $R^T S R$ is diagonal for some (rotation) matrix R , which means that $S = R^T D R$, where D is a diagonal matrix with the eigen values of S along its diagonal.

This means that we can always find some change of basis that transforms T into a diagonal form

$$\vec{T} = \begin{pmatrix} \sigma_1 & & \\ & \sigma_2 & \\ & & \sigma_3 \end{pmatrix} \quad (2.3)$$

The σ_i 's are called the principal stresses. Choosing these coordinates brings us closer to our goal of defining the generalization of Hooke's law for 3D materials. The second ingredient that we need is the measure of the deformation.

Strain tensor

The strain tensor measures the change of distances between close points in the deformed state with respect to the distances in the un-deformed state. Let $\varphi: \Omega \rightarrow \mathfrak{R}^3$ be the mapping from the un-deformed state to the deformed state. Compare the distance between two points that are close together in the reference frame, $\|(\vec{x} + d\vec{x}) - \vec{x}\|^2$, with the distance between them in the deformed frame $\|\varphi(\vec{x} + d\vec{x}) - \varphi(\vec{x})\|^2$. We have

$$\|(\vec{x} + d\vec{x}) - \vec{x}\|^2 = \|d\vec{x}\|^2 = d\vec{x}^T d\vec{x} \quad (2.4)$$

in the reference frame and

$$\|\varphi(\vec{x} + d\vec{x}) - \varphi(\vec{x})\|^2 = (\varphi(\vec{x} + d\vec{x}) - \varphi(\vec{x}))^T (\varphi(\vec{x} + d\vec{x}) - \varphi(\vec{x})) \quad (2.5)$$

In the deformed frame. For small deformation, we can approximate $\varphi(\vec{x} + d\vec{x})$ with $\varphi(\vec{x}) + \nabla \varphi d\vec{x}$, so

$$(\varphi(\vec{x} + d\vec{x}) - \varphi(\vec{x}))^T (\varphi(\vec{x} + d\vec{x}) - \varphi(\vec{x})) \approx (\nabla \varphi d\vec{x})^T (\nabla \varphi d\vec{x}) = d\vec{x}^T \nabla \varphi^T \nabla \varphi d\vec{x} \quad (2.6)$$

Aside: the gradient of a vector matrix. Specifically, if $\varphi(z) = (\varphi_1(z), \varphi_2(z), \varphi_3(z))^T$, then

$$\nabla \boldsymbol{\varphi} = \begin{pmatrix} \nabla \varphi_1 \\ \nabla \varphi_2 \\ \nabla \varphi_3 \end{pmatrix} \quad (2.7)$$

The dyadic product $\nabla \boldsymbol{\varphi}^T \nabla \boldsymbol{\varphi}$ is called the Cauchy-Green deformation tensor. Finally, if we take the difference between the reference and deformed squared distances, we will get

$$dx^T \nabla \boldsymbol{\varphi}^T \nabla \boldsymbol{\varphi} dx - dx^T dx = dx^T (\nabla \boldsymbol{\varphi}^T \nabla \boldsymbol{\varphi} - I) dx \quad (2.8)$$

The quantity $\nabla \boldsymbol{\varphi}^T \nabla \boldsymbol{\varphi} - I$ is twice the strain tensor. Note that strain is non-dimensional and it is easy to derive the transformation rules for this matrix under coordinate transformations, which end up to be the same as for the stress tensor. It follows directly from the definition that this tensor is symmetric.

$$\boldsymbol{\varepsilon} = \begin{pmatrix} \varepsilon_{11} & \varepsilon_{12} & \varepsilon_{13} \\ \varepsilon_{12} & \varepsilon_{22} & \varepsilon_{23} \\ \varepsilon_{13} & \varepsilon_{23} & \varepsilon_{33} \end{pmatrix} \quad (2.9)$$

It can also be chosen a coordinate system in which the strain is diagonal:

$$\boldsymbol{\varepsilon} = \begin{pmatrix} \varepsilon_1 & & \\ & \varepsilon_2 & \\ & & \varepsilon_3 \end{pmatrix} \quad (2.10)$$

The diagonal elements are called principal strains. This mathematical fact has important physical meaning: any deformation locally can be regarded as a simple stretch/compression along three perpendicular directions. For getting a better idea about the meaning of the principal strains, let us consider the change in length along a principal direction; according to the definition of strain, the new squared length is given by

$(dx_1, 0, 0)(2\varepsilon + 1)(dx_1, 0, 0)^T$, i.e.

$$(dx_1 \ 0 \ 0) \begin{pmatrix} 2\varepsilon_1+1 & & \\ & 2\varepsilon_2+1 & \\ & & 2\varepsilon_3+1 \end{pmatrix} \begin{pmatrix} dx_1 \\ 0 \\ 0 \end{pmatrix} = (2\varepsilon_1+1)dx_1^2 \equiv dx_1'^2. \quad (2.11)$$

Assuming small strain $\sqrt{2\varepsilon_1+1} \approx 1 + \varepsilon_1$, so $\frac{|dx_1'| - |dx_1|}{|dx_1|} = \varepsilon_1$, where the first quantity is the relative change in length in the x_1 direction.

2.2 Christoffel Equation

The field equations of linear elastodynamics are:

The equations of motion

$$\bar{\nabla} \cdot \hat{\sigma} = \rho \frac{\partial^2 \bar{u}}{\partial t^2} \leftrightarrow \sigma_{ij,j} = \rho \frac{\partial^2 u_i}{\partial t^2} \quad (2.12)$$

The constitutive relations:

$$\hat{\sigma} = \hat{C} \cdot \hat{S} \leftrightarrow \sigma_{ij} = C_{ijkl} S_{kl} \quad (2.13)$$

and the strain-displacement relation:

$$\hat{S} = \frac{1}{2} \{ \bar{\nabla} \bar{u} + (\bar{\nabla} \bar{u})^T \} \leftrightarrow S_{kl} = \frac{1}{2} \{ u_{k,l} + u_{l,k} \} \quad (2.14)$$

Where $\hat{\sigma}$ is the stress 2-tensor field, \hat{S} is the strain 2-tensor field, \hat{C} is the elasticity 4-tensor, \bar{u} is the displacement vector field, and ρ is the material density. The traction across any surface with normal \hat{n} is given by: $\hat{\sigma} \cdot \hat{n} \leftrightarrow \sigma_{ij} n_j$ general tractions and displacements must be continuous across boundaries. From angular momentum balance considerations of non-polar media, we know that the stress tensor $\hat{\sigma}$ is symmetric, i.e.: $\sigma_{ij} = \sigma_{ji}$. From its definition, the strain tensor is symmetric as well: $S_{ij} = S_{ji}$. It follows therefore, that the elasticity 4-tensor has the following *minor* symmetries: $C_{ijkl} = C_{jikl}$; $C_{ijkl} = C_{ijlk}$ from thermodynamic considerations, the elasticity 4-tensor also has the following *major* symmetry: $C_{ijkl} = C_{klij}$. In view of these symmetries, there are at most 21 independent elastic stiffness constants for the most anisotropic materials. With increasing levels of material symmetry, the number of independent elastic stiffness constants decreases, with only 3 for cubic crystals, and only 2 for isotropic materials.

2.3 Normal Modes in Unbounded Media

Let us first consider a homogenous unbounded linear elastic anisotropic medium and figure out whether we can propagate plane harmonic waves in these. In an unbounded medium we do not have to worry about boundary conditions and so we just have to satisfy the above field equations. Let us seek plane harmonic waves given by the following displacement field:

$$\vec{u}(r,t) = \vec{U} \exp\{jk(\hat{l} \cdot \vec{r} - vt)\} \quad (2.15)$$

Where \vec{U} is the displacement *amplitude* vector, \hat{l} is a unit vector along the propagation direction of the wave, $\vec{r} = x_1\hat{e}_1 + x_2\hat{e}_2 + x_3\hat{e}_3$ is the position vector, $k = 2\pi/\lambda$ is the wave number, λ is the wavelength, and v is the phase velocity of the wave. The angular frequency of the harmonic wave is related to the wave number and phase velocity through: $\omega = kv = 2\pi v/\lambda$. The \hat{e}_i 's are unit vectors along the 1, 2 and 3 Cartesian axes, and we use the symbol $i = \sqrt{-1}$ for the imaginary number.

Putting the above in equations (2.13), we get:

$$C_{ijkl}l_jl_kU_i = \rho\omega^2U_i \quad (2.16)$$

Which, after dividing both sides by k^2 , we can re-write as:

$$\{\Gamma_{ik} - \delta_{ik}\rho v^2\}U_k = 0 \quad (2.17)$$

where

$$\Gamma_{ik} = C_{ijkl}l_jl_l \quad (2.18)$$

is called the Christoffel matrix, and equation (2.17) is called the Christoffel equation. If we consider that equation (2.17) is an eigen value problem, it is independent of the frequency (and there are no boundary conditions to be satisfied). Therefore we can expect non-dispersive plane waves in unbounded anisotropic media.

Now we can easily see that the Christoffel matrix is symmetric, and under some non-restrictive conditions on the elastic stiffness's, that it is from the spectral theorem for positive-definite symmetric matrices, there are three positive, real eigen values for Γ_{ik} . It means that the wave phase velocities v , which are just the square roots of these eigen values divided by the density, are guaranteed to be real and so will represent propagating modes. The eigen values are obtained by solving the secular equation:

$$\det\{\Gamma_{ik} - \delta_{ik}\rho v^2\} = 0 \quad (2.19)$$

Again from the spectral theorem, corresponding to each of these eigen values $v^{(n)}$ there is at least one real eigenvector and, also can find three orthogonal eigenvectors which are denoted by: $\vec{U}^{(n)}$. Therefore, what we find is that in any homogeneous anisotropic material always *three* types of plane harmonic waves along any chosen propagation direction \vec{l} can propagate. In general, these three waves will have different phase velocities $v^{(n)}$, and the

corresponding particle displacement vectors $\vec{U}^{(n)}$ will be mutually orthogonal. Each of these modes is called a normal mode of propagation. We can call the direction of the displacement vector, the *polarization* direction of the wave. Note, however, that the particle displacement vector needs not to be parallel or perpendicular to the propagation direction in general. If it happens that the polarization direction of a wave is parallel to the propagation direction, we call it a *pure longitudinal* wave. Waves with polarization direction normal to the propagation direction are *pure shear* waves. If the polarization directions are neither parallel nor perpendicular to the propagation direction, the waves are neither pure longitudinal nor pure shear. In such cases, the mode whose polarization makes the smallest angle to the propagation direction is called a *quasi-longitudinal* wave, and the other two are called *quasi-shear* waves.

Contracted Voigt notation

Due to symmetries of tensors it is possible to apply the contracted notation, that allows to write fourth rank tensors C_{ijkl} in form of 2D matrix c_{IJ} . The contraction rules are

$$\begin{aligned} 11 &\leftrightarrow 1, & 22 &\leftrightarrow 2, & 33 &\leftrightarrow 3, \\ 12, 21 &\leftrightarrow 6, & 13, 31 &\leftrightarrow 5, & 23, 32 &\leftrightarrow 4, \end{aligned}$$

While contracted indexes allow 2D notation of fourth rank tensors and is useful in publications, the standard indexes are more convenient when read as algorithms of numerical calculations. That's why in the following we apply both of them.

2.4 Plane Waves in Unbounded Isotropic Media

For an isotropic material, as all directions are equivalent, we are free to chose a convenient propagation direction such as $I = \hat{e}_1$, so that the Christoffel matrix readily simplifies to:

$$\Gamma_{ij} = \begin{bmatrix} c_{11} & 0 & 0 \\ 0 & c_{44} & 0 \\ 0 & 0 & c_{44} \end{bmatrix} \quad (2.20)$$

Where contracted notation is applied.

The secular or characteristic equation resulting from solving for the eigen values of the above then becomes:

$$\{c_{11}-\rho v^2\}\{c_{44}-\rho v^2\}\{c_{44}-\rho v^2\}=0 \quad (2.21)$$

The three roots $v^{(n)}$ of this equation are:

$$v^{(1)} \equiv v_L = \sqrt{\frac{c_{11}}{\rho}} \quad (2.22)$$

With the corresponding polarization parallel to the propagation direction and which therefore represents a longitudinal wave; and two degenerate roots:

$$v^{(2)} = v^{(3)} \equiv v_T = \sqrt{\frac{c_{44}}{\rho}} \quad (2.23)$$

with the corresponding polarization along any direction on the plane perpendicular to the propagation direction, and which therefore represent shear waves.

2.5 Plane Waves in Unbounded Anisotropic Media (in contracted notation)

For a general anisotropic material, it is not easy to simplify the secular equation analytically for arbitrary propagation directions, even though it may be possible to obtain analytically tractable expressions for special cases of propagation along certain material symmetry directions. In general, however, one seeks numerical solutions for the anisotropic problem. Note that the Christoffel matrix is most readily calculated using contracted notation by defining a 3×6 propagation direction–cosine matrix (Auld, 1993):

$$[L] = \begin{bmatrix} l_1 & 0 & 0 \\ 0 & l_2 & 0 \\ 0 & 0 & l_3 \\ 0 & l_3 & l_2 \\ l_3 & 0 & l_1 \\ l_2 & l_1 & 0 \end{bmatrix} \quad (2.24)$$

By direct expansion we can show that $\hat{\Gamma} = \hat{L}^T \hat{C} \hat{L}$, ie:

$$\Gamma = \begin{bmatrix} l_1 & 0 & 0 & 0 & l_3 & l_2 \\ 0 & l_2 & 0 & l_3 & 0 & l_1 \\ 0 & 0 & l_3 & l_2 & l_1 & 0 \end{bmatrix} \begin{bmatrix} c_{11} & c_{12} & c_{13} & c_{14} & c_{15} & c_{16} \\ c_{12} & c_{22} & c_{23} & c_{24} & c_{25} & c_{26} \\ c_{13} & c_{23} & c_{33} & c_{34} & c_{35} & c_{36} \\ c_{14} & c_{24} & c_{34} & c_{44} & c_{45} & c_{46} \\ c_{15} & c_{25} & c_{35} & c_{45} & c_{55} & c_{56} \\ c_{16} & c_{26} & c_{36} & c_{46} & c_{56} & c_{66} \end{bmatrix} \begin{bmatrix} l_1 & 0 & 0 \\ 0 & l_2 & 0 \\ 0 & 0 & l_3 \\ 0 & l_3 & l_2 \\ l_3 & 0 & l_1 \\ l_2 & l_1 & 0 \end{bmatrix} \quad (2.25)$$

That is a contracted notation equivalent of (2.18)

2.6 Acoustic wave equation in piezoelectric media

The basic equations describing vibrations in piezoelectric anisotropic media are

$$\sigma_{ij} = C_{ijlm}^E S_{lm} - e_{ijr} E_r \quad (2.26)$$

$$D_r = e_{ijr} S_{ij} + \epsilon_{rl}^S E_l \quad (2.27)$$

σ denotes the elastic stress tensor, \vec{E} the electric field, \vec{D} the electric displacement, C^E the elastic modulus tensor at constant electric field, e the piezoelectric stress tensor, and ϵ^S the permittivity tensor at constant strain.

The equations of motion can be written as: Einstein summation of conservation is applied.

$$\rho \frac{\partial^2 u_i}{\partial t^2} = \frac{\partial \sigma_{ij}}{\partial x_j} = C_{ijlm}^E \frac{\partial S_{lm}}{\partial x_j} - e_{ijr} \frac{\partial E_r}{\partial x_j} \quad (2.28)$$

If a plane-wave solution in the form $\vec{u} = \vec{U} e^{i(\omega t - \vec{k} \cdot \vec{x})}$ and a similar dependence of the scalar electric potential $\phi = \phi_0 e^{i(\omega t - \vec{k} \cdot \vec{x})}$ are assumed, the electric field becomes

$$E_l = (-\nabla \phi)_l = ik_l \phi_0 e^{i(\omega t - \vec{k} \cdot \vec{x})}, \quad (2.29)$$

that is $\vec{E} \parallel \vec{k}$. From the absence of free charges it follows that:

$$\frac{\partial D_r}{\partial x_r} = e_{ijr} \frac{\partial S_{ij}}{\partial x_r} + \epsilon_{rl}^S \frac{\partial E_l}{\partial x_r} = e_{ijr} \frac{\partial^2 u_i}{\partial x_r \partial x_j} + \epsilon_{rl}^S \frac{\partial E_l}{\partial x_r} = 0, \quad (2.30)$$

and, hence

$$\phi_0 = \frac{e_{ijr} k_j k_r U_i}{\epsilon_{pq}^S k_p k_q}. \quad (2.31)$$

Equation (2.28) then becomes

$$\rho \omega^2 U_i = C_{ijlm}^E k_j k_m U_l + k_j k_m \frac{e_{ijr} k_r e_{lms} k_s}{(\epsilon_{pq}^S k_p k_q)} U_l \quad (2.32)$$

After dividing by k^2 and introducing the Cartesian components n_l of the unit vector in the direction of \mathbf{k} this leads to the modified Christoffel equation

$$\{\Gamma_{il} - \delta_{il} \rho v^2\} U_l = 0 \quad (2.33)$$

with the sound velocity v ,

$$\Gamma_{il} = C'_{ijlm} n_m n_j \quad (2.34)$$

and stiffened elastic constants

$$C'_{ijlm} = C_{ijlm}^E + \frac{e_{ijr} n_r e_{lms} n_s}{\epsilon_{pq}^S n_p n_q} \quad (2.35)$$

The solution yields three modes of propagation with phase velocities $v^{(n)}$ and polarizations $\vec{U}^{(n)}$ for each mode n and with appropriate slowness and group velocity vectors related to them.

3 Methodology: Scanning Acoustic Microscope

3.1 Scanning Acoustic Microscope

Optical and the electron microscope have provided us extraordinary insights into the world of the nano-scale and are continuing to enjoy widespread application in the future. Microscopes are well introduced: infrared microscope (Okano et al., 1994), scanning Auger microscope (Benetti et al., 2005), Raman microscope (Bergman & Nemanich, 1996), scanning laser microscope (PI), ion microscope (Kino, 1987), X-ray microscope (Farnell, 1970), tunneling microscope (Briggs, 1992), and their application is continue to grow. All of these microscopes have their special characteristics, their particular advantages and limitations, and they should be viewed as a complementary collection. However, most of the optical techniques are limited towards investigation of surface topology and chemical composition evaluation. The measurement of the elastic property of material using above microscopic techniques still remains an open question.

In order to address this issue, the potential of sound waves are explored for evaluation of elastic properties of materials using the scanning acoustic microscope (SAM). The key role in SAM is played by Rayleigh waves (consists a mixture of longitudinal and shear waves). These are surface acoustic waves whose existence was discovered theoretically by Lord Rayleigh in 1885 (Rayleigh, 1885). The main idea of the acoustic microscopy was first introduced by Sokolov in 1949 (Sokolov, 1949). It is similar to other forms of radiation; an acoustic wave interacts directly with the elastic properties of the material through which it propagates. At high frequency (2.4 GHz) the wavelength of sound is small (0.7 μm), and resolution is comparable to that of the optical microscope. Based, on the Abbe criteria, for the opening angle of 180° , the lateral resolution is approximately given as $\Delta x \approx \lambda/2$, where Δx is the lateral resolution and λ is the wavelength.

In SAM, ultrasonic waves are excited through piezoelectric transducer (ZnO) with short delta pulse. The ultrasonic waves are transmitted through the spherical lens rod with high impedance and are focused on the specimen (figure 3.1). The ultrasonic waves transmit through an acoustic duct possessing large acoustic impedance and are then focused with the aid of a spherical recess (lens) at the other duct end in an immersion material (distilled water) filling the space between the lenses and objects examined. The size of the focal spot of the lens depends on the material of lens rod and frequency of excitation and governs the spatial and temporal resolution. Usually the dimension of focal spot is 0.8 μm at 1 GHz.

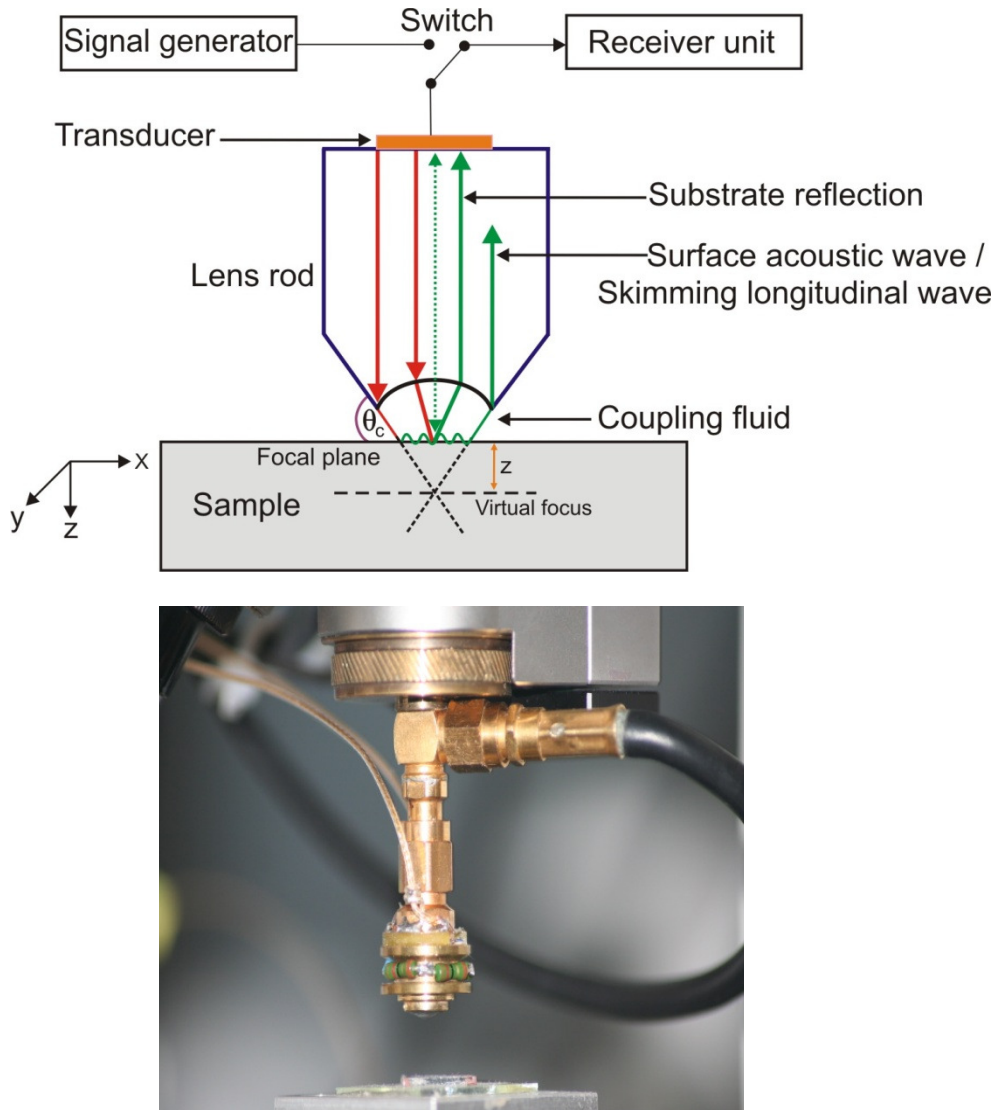


Figure 3.1: a) Schematic of a scanning acoustic microscope lens with a focal point defocused at depth z from the sample surface. b) Image of the lens of a scanning acoustic microscope

The immersion liquid provides a large refractive index for the acoustic lens and good acoustic coupling fluid in between the duct and specimen under investigation. The focused beam interacts with the object, and the waves undergo direct reflection from surface, reflection from the subsurface layers and scattered by the specimen.

SAM operates in two independent modes: reflection of echo signal and transmission of pulse signal. When the transmitted acoustic flux is recorded with the aid of the second lens, then it's a transmission acoustic microscope. Resolution of the instrument and depth of radiation penetration are the most important characteristics in SAM. The penetration ability of a SAM can be estimated as equal to the penetration of excited surface waves. It is about

the same magnitude as the wavelength of the surface waves. The practical penetration depth depends on the elastic parameters of the object, the signal-to-noise ratio, and the operating frequency of the SAM (PI). As the spatial resolution increases, the depth of ultrasound penetration in the object reduces due to attenuation. Therefore, the ultrasound frequency is judiciously selected considering the elastic and acoustic properties of the specimen.

SAM has emerged as a tool for the noninvasive micro-structural characterization of materials. It can be used to determine surface and subsurface mechanical properties of thin films. In 1970s, C. F. Quate (Lemons & Quate, 1974) developed the first prototype of the scanning acoustic microscopy for material evaluation. A comprehensive review of the principles of SAM can be found elsewhere (Briggs & Kolosov, 2009). SAM excites longitudinal, transversal and surface acoustic waves in the material during the defocusing. Surface acoustic waves (SAWs) are frequently for surface detection of abnormalities as the wavelength is spatially confined to the surfaces and the phase is sensitive to surface inhomogeneities.

Researcher have used the SAM for measuring acoustic velocity and attenuation of surface waves in material in an attempt to obtain the elastic properties of the material (Kushibiki *et al.*, 1983) and thin films (Kushibiki *et al.*, 1982, Achenbach, 2004) and anisotropy property in materials (Kushibiki *et al.*, 1981). Also, coating thickness of the material and inherent stresses induced are investigated using SAM (Sasaki *et al.*, 1992). SAM is also capable of visualizing the stress inside materials (Drescher-Krasicka & Willis, 1996). In order to detect the delaminations in electronic integrated circuit chips (Gilmore, 1996) SAM is the best option. It provides a combination of features that makes it valuable for such a wide range of applications. It is possible to use wide range of ultrasonic frequencies, hence providing access to multi-scale properties of materials. The elastic constants of bulk materials, and the group velocity and attenuation of longitudinal and surface acoustic waves excited on the surface of specimens can be quantitatively evaluated through the acoustic material signature (AMS) curve. Despite this abundant literature, scanning acoustic microscopy has had limited scientific impact in the thin film technology and surface science community.

In the present investigation, the capabilities of SAM are utilized for mechanical characterization of piezoelectric sensors. The brief theoretical and numerical aspects related to SAM evaluation are discussed. Two main focus of study using SAM are: i) ultrasonic

characterization of AlN thin films and ii) mechanical characterization of sintered piezoelectric ceramics.

3.2 Principles of Scanning Acoustic Microscopy

The scanning acoustic microscope was equipped with a broad band acoustic transducer (figure 3.1) excited at central frequency of 1.2 GHz (PVA TePla Analytical systems GmbH, Westhausen, Germany). The signal acquisition was sampled with a resolution of 8 bit at 250 kHz sampling rate (Brand *et al.*, 2007). The experiments were performed in double distilled water as coupling medium at room temperature (22°C) exhibiting the bulk acoustic sound velocity of 1496 m/s (Encyclopedia, 1999). Figure 3.1 shows the schematic diagram and image of a SAM. The transducer (typically made of ZnO) is mounted on a sapphire buffer rod which is typically made of sapphire for high-frequency microscopes. The acoustic lens with the focal point (F) placed at defocus depth, z and a lateral focus width of 0.8 μm . The AMS curve was generated by recording the signal amplitude as a function of z starting from the focal point coinciding with the top surface of the sample to $z=60 \mu\text{m}$ with an increment $\Delta z=1 \mu\text{m}$. Both the surface skimming longitudinal and the surface acoustic waves were excited for different critical angles of incidence.

A tone burst signal generated by a pulser unit at the operating frequency (1.2 GHz) excited the transducer (marked in figure 3.1). It converts the burst into a plane sound wave that propagates through the lens rod down to the lens surface which is in contact with the coupling liquid on top of the sample surface. The concave spherical lens located at the end of the sapphire lens rod focuses the ultrasonic energy into a point. The sample placed in between the lens and the focal point of the converging rays reflects the incoming wave in different manners back to the transducer. The component of the ultrasonic energy which propagates near the central axis of the lens and parallel to the central lens axis is reflected back to the transducer without much interaction with the sample. The part of the incoming convergent ultrasonic beam energy which strikes the sample at Rayleigh critical angle (Kundu *et al.*, 1985, Every & Deschamps, 2003) generates leaky Rayleigh waves along the sample surface and within the immersed coupling fluid before they leaked back to the coupling fluid and received by transducer. Thus the transducer mounted on top of the lens rod receives two reflected waves separated by a phase difference. This phase difference changes as the defocus distance z is varied because of the constructive and destructive interference between these

two reflected beams. These interferences are visualized by the AMS curve which shows the variation of receiver voltage (V) as function of the defocus distance (z). The AMS curve contains fingerprints of normally reflected waves, surface skimming longitudinal acoustic waves (SLAW) and leaky surface acoustic waves (LSAW) (Every & Deschamps, 2003, Kushibiki *et al.*, 1989) as discussed in detail in following sections.

3.3 Theory of Acoustic Material Signature Curve

The AMS curve is obtained by plotting the total energy (E) of the transient signal (measured by the voltage of the receiver) at each step of defocusing distance z, as shown in figure 3.1. This energy is calculated from the formula $E = \sum_{n=-\infty}^{\infty} |A(n)|^2$ where n are the sampling points and A(n) is the amplitude of the nth sampling point. Surface acoustic waves, surface skimming longitudinal acoustic waves and their interference contribute to AMS. For a point focused acoustic beam striking an anisotropic solid, the acoustic material signature curve V(z) is given by

$$V(z) = \int_0^{\theta_m} P(\theta) \overline{R(\theta)} \exp(-2ikz \cos \theta) d\theta \quad (3.1)$$

where $P(\theta)$ is the pupil function of the point focus lens. For a point focused transducer, the reflection coefficient, $R(\theta, \varphi)$ depends on the polar angle θ and the sagittal plane of orientation averaged over azimuth angle of φ ,

$$\overline{R(\theta)} = \frac{1}{2\pi} \int_0^{2\pi} R(\theta, \varphi) d\varphi \quad (3.2)$$

$k = \frac{2\pi f}{C_f}$ is the wave number and C_f is the velocity of the acoustic wave in the coupling fluid at the excitation frequency f , z is the distance of the focal point between lens and sample surface (Kundu & Jørgensen, 2002, Every & Deschamps, 2003, Kushibiki *et al.*, 1989). A typical V(z) curve shows a peak at $z=0$ and decaying if the focal point z is moving in either positive or negative directions. However, this decay is not monotonic. It oscillates due to the interference between the centrally reflected beam and the reflected beam generated by the surface skimming waves (Kundu & Jørgensen, 2002, Kundu *et al.*, 1985, Every & Deschamps, 2003, Weglein, 1979, Habib *et al.*, 2012b). Hirsekorn and Pangraz have shown excellent aspects of material characterization using interference of acoustic wave derived

through material signature curve (Hirse Korn & Pangraz, 1994). The Fourier transform of the AMS curve shows the existing wave mode including the surface skimming longitudinal acoustic wave (SLAW) and the surface acoustic wave (SAW) at a spatial separation of $\Delta z = 1/k$. The corresponding velocities C_{SAW} and C_{SLAW} of the SAW and SLAW are given (Kundu & Jørgensen, 2002)

$$C_{SAW} = \frac{C_f}{\sqrt{\frac{C_f}{2\Delta z_{SAW} f} - \left(\frac{C_f}{4\Delta z_{SAW} f}\right)^2}} \quad (3.3)$$

$$C_{SLAW} = \frac{C_f}{\sqrt{\frac{C_f}{2\Delta z_{SLAW} f} - \left(\frac{C_f}{4\Delta z_{SLAW} f}\right)^2}} \quad (3.4)$$

Rearrangement of equation (3.3) gives the distance between two successive peaks corresponding to SAW

$$\Delta z_{SAW} = \frac{1}{2f \left[\frac{1}{C_f} - \left(\frac{1}{C_f^2} - \frac{1}{C_{SAW}^2} \right)^{1/2} \right]} \quad (3.5)$$

If the Fourier spectrum of the AMS curve displays two distinct peaks corresponding to SAW and SLAW, the material elastic constants can be obtained by

$$\left(2 - \frac{C_{SAW}^2}{C_T^2} \right)^2 - 4 \left(1 - \frac{C_{SAW}^2}{C_{SLAW}^2} \right)^{1/2} \left(1 - \frac{C_{SAW}^2}{C_T^2} \right)^{1/2} = 0 \quad (3.6)$$

Here C_T represents the shear wave velocity in the material. Knowing C_{SLAW} and the material density ρ and the Poisson's ratio ν , the shear modulus G , can be obtained considering equations 3.7- 3.9, respectively

$$C_T = C_{SLAW} \sqrt{\frac{1-2\nu}{2(1-\nu)}} \quad (3.7)$$

$$C_l = \sqrt{\frac{E(1-\nu)}{\rho(1+\nu)(1-2\nu)}} \quad (3.8)$$

$$C_T = \sqrt{\frac{G}{\rho}} \quad (3.9)$$

The expression of the ultrasonic wave potential for linear elastic materials is given by (Weglein, 1979, Kundu, 1992)

$$\phi_i(x, 0) = rT_{sf}(\theta_s) \exp \left[ik_s r(1 - \cos \theta_s) + \frac{ik_f \left\{ \frac{r}{\cos \theta_f - \mu \cos \theta_s} - \sqrt{x^2 + z^2} \right\}}{(\cos \theta_f - \mu \cos \theta_s) \sqrt{x^2 + z^2}} \right] \quad (3.10)$$

where, $\phi_i(x, y)$ is the amplitude of the incident wave at the interface between the coupling fluid and the solid specimen at $y=0$. The radius of curvature of the lens is given by r and T_{sf} is the plane wave transmission coefficient at the solid-fluid interface between the acoustic lens and the coupling fluid. k_f and k_s are the wave numbers in fluid and solid media, respectively and θ_s is the incident angle of the wave at the lens-coupling fluid interface and $\mu = \frac{C_f}{C_{SLAW}}$.

Surface skimming longitudinal acoustic waves (SLAW) also propagate through the sample's surface radiating or leaking the acoustic energy into the coupling fluid.

3.4 Ultrasonic Characterization of c-axis Oriented Polycrystalline AlN Film Using Scanning Acoustic Microscopy

Summary

Polycrystalline aluminum nitride (AlN) films for applications in high frequency surface acoustic wave (SAW) devices were prepared by RF-magnetron sputtering of a high purity aluminum target material in nitrogen atmosphere with 6.6 μm thickness and preferential c-axis orientation. The surface dominated elastic modulus and hardness of AlN film were evaluated using nanoindentation. Detailed mechanical characterization of AlN film was conducted by scanning acoustic microscopy (SAM) in reflection mode using an excitation frequency of 1.2 GHz. Acoustic material signature curves (AMS) were recorded in order to measure the surface and bulk wave velocities in the film. These values were determined from the Fourier transform of the AMS curve as 11063 ± 171 m/s for the longitudinal, 6046 ± 18 m/s for the transversal or shear and 4677 ± 33 m/s for the surface acoustic wave. From the derived material properties and thickness of the film, the Lamb wave dispersion and the bulk angular dispersion relationship were computed.

3.4.1 Introduction

Aluminum nitride (AlN) is piezoelectric semiconductor material developed for optoelectronic devices because of their wide-band-gap, chemical and mechanical stability, dielectric properties and relatively high elastic constants. Its excellent thermal stability at high temperatures and the high surface acoustic wave velocity make the material attractive for electro-mechanical applications (Bergman & Nemanich, 1996). Piezoelectric AlN thin films have been used to fabricate a variety of radio frequency (RF) resonators and filters, such as surface acoustic wave (SAW) devices (Pearce *et al.*, 1981), contour mode resonators (Piazza *et al.*, 2006), bulk acoustic resonators (Wang & Lakin, 1982), and Lamb wave resonators (Bjurström *et al.*, 2005). Also it was shown that AlN maintains its piezoelectric properties up to a temperature of 1150°C which gives it an advantage over conventional piezoelectric crystals, such as quartz, lithium niobate and lithium tantalite (Slobodnik, 1973).

AlN does not grow as a single crystal but using various sputtering techniques it can be prepared as polycrystalline films with preferential c-axis orientation. AlN deposition onto single crystalline (111) silicon substrates was found to increase the quality factor of

piezoelectric resonant devices (Pearce et al., 1981). Attempts have been made to grow AlN films by metal organic chemical vapor deposition (MOCVD) at elevated temperatures of 1200°C (Liu *et al.*, 1975). Earlier works show c-axis growth of poly-crystalline AlN film using DC and RF sputtering techniques (Liaw & Hickernell, 1995, Penza *et al.*, 1995).

Before the device applications, it is essential to characterize the mechanical properties of AlN thin films. Often the elastic properties of thin films differ from those of the corresponding bulk material due to the specifics of the respective deposition process. The determination of SAW velocity is important for application of AlN in optoelectronics. However, an inter digital transducer (IDT) could not be used due to low film thickness and periodicity of the IDTs, exaggerating the effects from the substrate. Liaw et al. 1995, investigated microstructure characterization of AlN films (grown by DC and RF sputtering) using X-ray diffraction, atomic force microscopy, and transmission electron microscopy to show the quality of AlN films at various deposition conditions.

Determination of the elastic properties of thin AlN films is challenging due to the contribution of the substrate. Kopycinska *et. al* 2003 have devised an effective near-field microscopy technique using enhanced AFM in tapping mode in combination with ultrasonic piezo-mode (Kopycinska *et al.*, 2003). The mechanical properties of thin film samples and multilayered thin film (TiN / NbN) and fused silica can be obtained by SAM and nanoindentation (Bamber *et al.*, 2001, Oliver & Pharr, 1992). In order to avoid the substrate influence, an indentation depth of less than 10% of film thickness is required (Tsui & Pharr, 1999). However, nanoindentation is an invasive technique and those measurements are restricted to selective regions of the sample. Earlier Carlotti *et al.*, 1997 (Carlotti *et al.*, 1997), has determined elastic properties of AlN using Brillouin light scattering (BLS). However, the BLS technique requires an optically polished transparent film with relatively low surface roughness. Also, the delamination of the thin film from the substrate is difficult to quantify using the BLS technique.

Scanning acoustic microscopy (SAM) has emerged as a tool for the noninvasive micro-structural characterization of materials. It can be used to determine surface and subsurface mechanical properties of thin films. A comprehensive review of the principles of SAM can be found elsewhere (Briggs & Kolosov, 2009). Researchers have applied 1 GHz SAM analysis for quantitative evaluation of anodized and coated aluminum (Sklar *et al.*, 1995). In the past, no detailed study has been conducted to evaluate holistically all micro-

structural and mechanical properties of c-axis orientated poly-crystalline aluminum nitride (AlN) which is presented here.

First we grew highly c-axis orientated poly-crystalline aluminum nitride (AlN) using reactive RF-magnetron sputtering of high purity aluminum target material in a nitrogen atmosphere. We conducted X-ray diffraction, atomic force microscopy, and scanning electron microscopy for micro-structural analysis. The main objective is to determine the elastic constants of the thin film that is achieved by the scanning acoustic microscopy (SAM) at 1.2 GHz. The results of SAM are validated with invasive nanoindentation test to study the feasibility of the methodology. The scanning acoustic microscopy was used as a major tool for this research in this chapter.

3.4.2 Experiment

3.4.3 Sample Preparation and Scanning Electron Microscopy

AlN films have been prepared by reactive RF-magnetron sputtering of high purity aluminum target material in a nitrogen atmosphere. An overview of relevant process parameters can be found in table 3.1.

Table 3.1: Process parameters for AlN film preparation using RF-magnetron sputtering

Process parameter	
Target power density:	3.82 W/cm ²
Substrate temperature:	162 °C
Base pressure:	1.7×10 ⁻⁵ Pa
Process pressure (N ₂):	0.43 Pa
Deposition rate:	16.15 nm/min

Crack-free, uniform, and highly c-axis oriented AlN polycrystalline films of 6.6 μm thickness were grown on (111) silicon substrates. Thickness and lateral homogeneity of the sputtered AlN film were characterized by scanning electron microscopy (SEM). Figure 3.2 shows the cross sectional SEM micrograph of an AlN film. The image indicates the homogeneous and columnar morphology of the film. The preferential c-axis oriented fibrous grains have lateral dimensions in the range of 10 nm to 20 nm from its roots to the film's surface. The average

film thickness is determined to be about $6.6\ \mu\text{m}$ by measuring the cross sectional SEM micrograph. The micrograph shows the absence of delaminating layers and the perfect connection between the film and the substrate. Although the SEM micrograph and the other applied characterization techniques does not show any hints of misaligned grains, one should consider such kind of defects in a sputtered, relatively thick film. The existence of such misaligned grains is usually accompanied by other structural defects that may significantly reduce the piezoelectric response of the films. These defects could stimulate the growth of grains with a polarization direction opposite to that of the majority of other grains. Such effects have been reported recently even for highly c-axis-textured films providing poor piezoelectric activity (Olivares *et al.*, 2007).

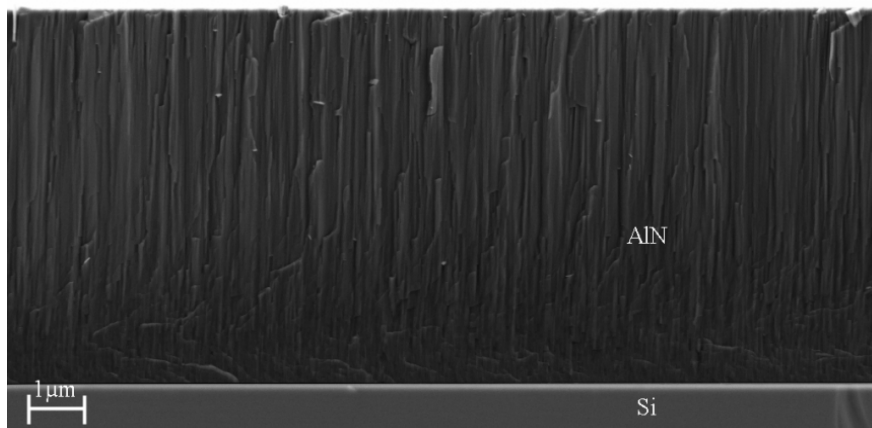


Figure 3.2: Cross sectional scanning electron microscopy image of AlN film. The film is uniform and highly c-axis oriented of $6.6\ \mu\text{m}$ thickness

Thus, the overall piezoelectric activity in polycrystalline films must be considered as the combination of the individual responses of different grains and is, hence, influenced by the crystal quality of the film. The irregular, stepwise broken structures near the substrate-film interface and misalignment of individual particles causes scattering of ultrasonic waves. Therefore, SEM images provide an estimate of the film quality and help to explain the heterogeneity of elastic properties in the sample.

3.4.4 Atomic Force Microscopy

Atomic force microscopy (AFM) (PSIA XE-100) experiments in non-contact mode using NCHR 20 (NanosensorsTM) tips have been performed to investigate the surface morphology of the AlN films. The topography appeared rather homogeneous as shown in

Figure 3.3. Within a scan area of $2.5 \times 2.5 \mu\text{m}^2$ the root mean square roughness R_a was measured to be 6.5 nm which is 0.4 percent of the exciting wave length of the AMS experiment. The AFM shows spots of typical diameter of 10 to 20 nm which we associate with the diameters of c-axis columns of AlN as stated in previous section. The column height fluctuation can be characterized by a root mean square roughness mentioned above.

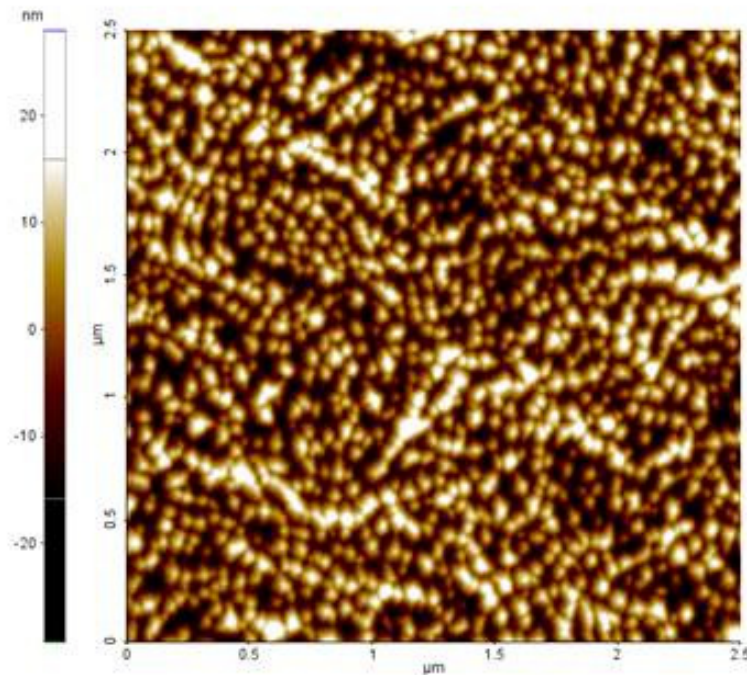


Figure 3.3: AFM image of the AlN film. Scan area $2.5 \times 2.5 \mu\text{m}^2$

Surface roughness plays a vital role for acoustical characterization of thin films. Major height variations originated by the AlN column and acting as particle like defects can significantly alter the local piezoelectric properties of the film. The ultrasonic signal strength decays during its propagation through such a material because of scattering at these defective particles. Rayleigh scattering is proportional to the third power of the grain size and fourth power of the frequency for wavelengths greater than particle size (Glegg, 1980). Therefore the defect scattering becomes significant if the particle size exceeds one-hundredth of the wavelength. Because the characteristic roughness of the AlN is smaller than the acoustic wavelength, significant wave attenuation and scattering was not expected.

3.4.5 X-ray Diffraction

The crystal structure and orientation of the AlN films were analyzed using X-ray diffraction technique with the help of a GE (XRD) machine, equipped with a sealed Cu

source (X-ray wave length $\lambda = 1.5416 \text{ \AA}$ running at 40 kV and 45 mA) X-ray tube. The size of the X-ray beam was 1 mm in diameter. The resolution of the experimental setup is in the order of 0.001° . The sample was mounted on a goniometer and aligned in Bragg geometry.

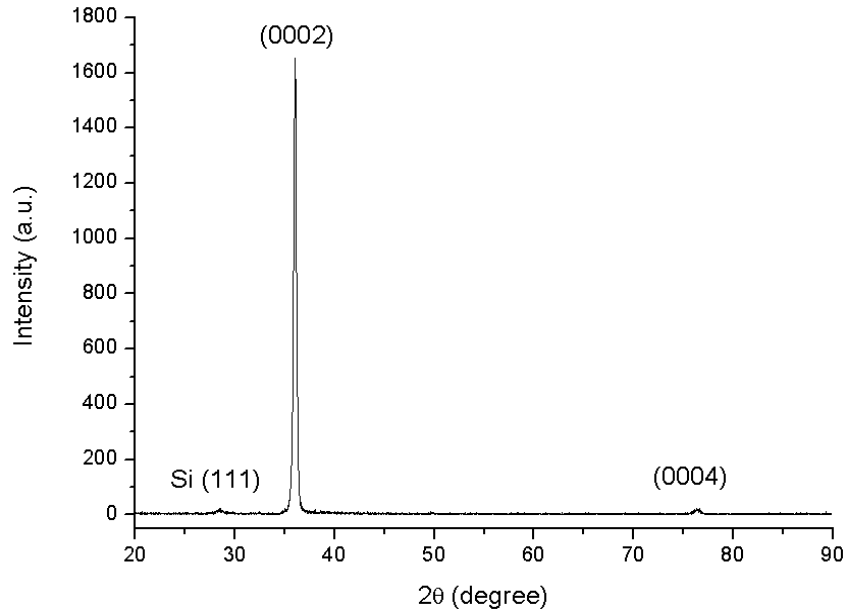


Figure 3.4: X-rays diffraction patterns of AlN thin films deposited on Si (111)

Figure 3.4 shows the X-ray diffraction pattern of the as-grown AlN film. The intense (0002) and its higher orders (0004) of reflections envisages the growth of c-axis oriented AlN films. Rather than those two reflections and the substrate peak (Si (111) centered at 28.4°) we could not observe any reflection which confirms the growth of uniaxial orientated film growth. The result present here are in good agreement with literature (Lin *et al.*, 2010).

3.4.6 Nanoindentation

Nanoindentation was used to probe the local mechanical properties like Young's modulus and hardness of the thin film. One measurement contains 50 indents (grid of 5×10 indents) with distance of $20 \mu\text{m}$ on an area of $80 \times 80 \mu\text{m}^2$ with increasing loads from 200 to 10,000 μN in steps of 200 μN . A linear load function was used with a maximum force holding time of 3 seconds (Yonenaga *et al.*, 2002). For the present samples nanoindentation was carried out utilizing a scanning nanoindenter (TriboIndenter, Hysitron) equipped with a Berkovich diamond tip. The environmental condition was kept constant (RT, 40% RH) during all tests. A method proposed by Oliver and Pharr (Oliver & Pharr, 1992, Thokala &

Chaudhuri, 1995) was used to calculate the mechanical properties - hardness H and elastic modulus E_r from equations 3.11 and 3.12, respectively.

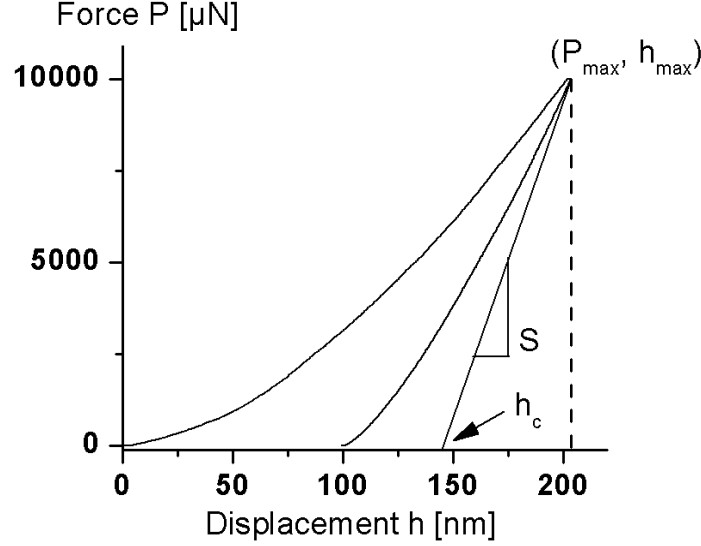


Figure 3.5: A typical force-displacement curve (Here: $P_{\max}=10$ mN)

The method is based on fitting the unloading segment of the force-displacement curve (P-h curve) to a power law and from that extracting the slope of the unloading segment at maximum load. Figure 3.5 shows the force-displacement curve at $P=10,000$ μN with maximum displacement ($h_{\max}=203.28$ nm) and fitting curve for determining the contact depth ($h_c=144.81$ nm)

$$H = P_{\max} / A \quad (3.11)$$

$$S = \frac{dp}{dh} = 2E_r \sqrt{\frac{A}{\pi}} \quad (3.12)$$

In this context, the stiffness S is defined as $S = \frac{dP}{dh}$ and A denotes the projected contact area between the sample and the indenter tip. A is calibrated as a function of the contact depth h_c . The films presented in the present study feature a hardness of about (18.5 ± 1.2) GPa. The reduced modulus is defined by

$$\frac{1}{E_r} = (1 - \nu_f^2) \frac{1}{E_s} + (1 - \nu_i^2) \frac{1}{E_i} \quad (3.13)$$

Where E_i is the isotropic elastic modulus (1141 GPa) and ν_i is the Poisson's ratio (0.07) of the diamond indenter, respectively. The Young's modulus (E_s) of the thin film is

evaluated using equation 3.13. The Poisson's ratio (ν_f) of AlN was taken from some older work as 0.287 (Thokala & Chaudhuri, 1995). Consequently we estimate a Young's modulus of 304 ± 3 GPa for the films studied here. This is in good agreement with the literature (Gerlich *et al.*, 1986). The wavelength of the excited bulk wave was approximately $1.4 \mu\text{m}$ and is smaller than a quarter of thickness of the AlN film. Since the penetration depth of surface skimming Rayleigh wave is about 1.5 times the wavelength, the silicon substrate at a depth more than 4 times the wavelength has insignificant influence on the elastic properties of the AlN thin film.

3.4.7 Results of Scanning Acoustic Microscopy

Prior to acoustic experiment the film density was measured by X-ray reflectometry using the angular position of critical angle of total external reflection (Als-Nielsen & McMorrow, 2001). In the present case it was determined to be $3.26 \pm 0.12 \text{ g/cm}^3$. The obtained value is in agreement with the literature (Yu, 2001). Surface acoustic waves are excited when the acoustic beam strikes the interface between the coupling fluid and the reflecting solid at a

critical angle obtained from Snell's law, $\sin \theta_c = \frac{C_f}{C_{SAW}}$. In the AMS or V(z) curve several

peaks and valleys correspond to the constructive and destructive interferences between SLAW, LSAW and centrally reflected beam. Figure 3.6 shows the acoustic material signature (AMS) curve derived from scanning acoustic microscope at an excitation frequency of 1.2 GHz. It clearly shows two distinct wave modes-presumably SLAW and SAW. The distance between first and second peaks of the interference pattern is $20 \mu\text{m}$ and is contributed from SLAW. The distance between second and third peaks is $13 \mu\text{m}$ and is contributed by SAW. The peaks at higher defocusing distance are due to multiply reflected interference modes. In the V(z) curve sometimes identification of individual wave modes is a challenging task. The V(z) curve is a periodic curve and therefore Fourier transform of this curve can accurately identify the individual wave mode by capturing the dominant frequency or spacing between the two successive peaks.

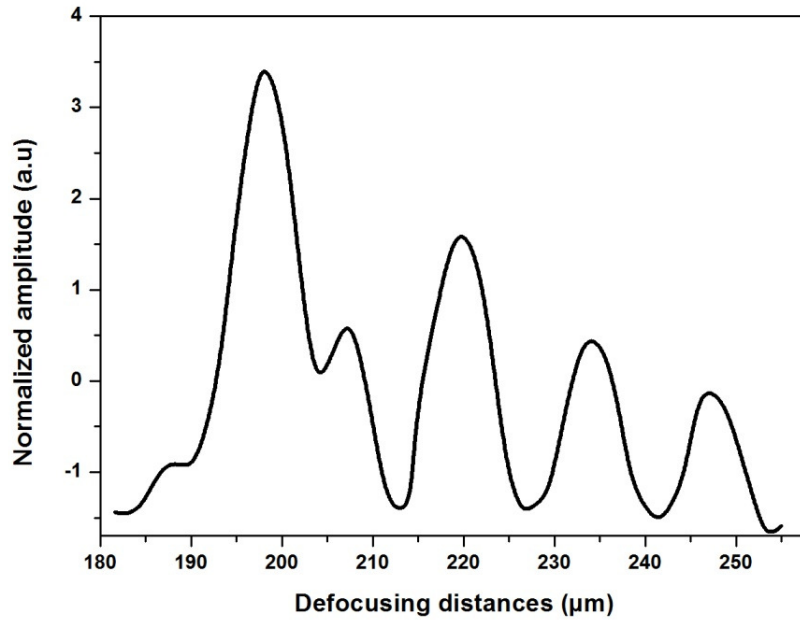


Figure 3.6: Acoustic Material signature (AMS) curve for 6.6 μm thick AlN film at 1.2 GHz excitation frequency the peaks show contributions from SLAW, SAW and multiple interference

The absolute distance between the SLAW and SAW wave modes, between SAW and higher order interference varies between 21 and 23 μm , respectively depending on the position of the acoustic lens on the sample surface. Similarly, the spacing between the primary SAW mode and its higher order interference pattern is $13 \pm 1 \mu\text{m}$.

Substituting the AMS curve parameters in equation 3.4, the group velocity of the SLAW is determined as $V_g = (6354 \pm 130) \text{ m/s}$. The group velocity of the SAW wave mode is calculated from the average distance between two successive peaks or dips. For the SAW wave mode (ΔZ_{SAW}) is $13 \pm 1 \mu\text{m}$ (determined from Figure 3.6) in the AMS curve as $V_{\text{SAW}} = (4883 \pm 152) \text{ m/s}$. The transversal wave velocity of the thin film as determined from equation 3.7 is $V_T = (6085 \pm 28) \text{ m/s}$. The speed of longitudinal wave velocity is derived from equation 3.8 as $11065 \pm 52 \text{ m/s}$. It was obtained using the modulus of rigidity $304 \pm 3 \text{ GPa}$, determined from nanoindentation test as mentioned above. From the speed of transversal waves, the shear modulus is calculated as $119 \pm 2 \text{ GPa}$.

The summary of the velocities and material parameters determined from nanoindentation and scanning acoustic microscopy tests are tabulated in Table 3.2

Table 3.2: Characteristic velocities derived from material parameters

Material properties	Bulk Velocities (m/s)	AMS(m/s)	FT(m/s)
$C_{11} = 399 \pm 3$ GPa	Longitudinal bulk mode	11065±52	11063±171
Density = 3.26 ± 0.12 g/cm ³	Skimming Longitudinal	6354±130	7091±10
$C_{44} = 119 \pm 2$ GPa	Transversal bulk mode	6085±28	6046±18
Hardness= 18.5 ± 1.2 GPa	Surface acoustic wave	4883±152	4677±33

From various numerical and experimental investigations Kushibiki *et al.*, 1989, and Kundu *et al.*, 2002, have suggested that more reliable prediction of wave velocity can be obtained from the Fourier transform of the AMS curves. The Fourier transform of the measured AMS curve is plotted in figure 3.7.

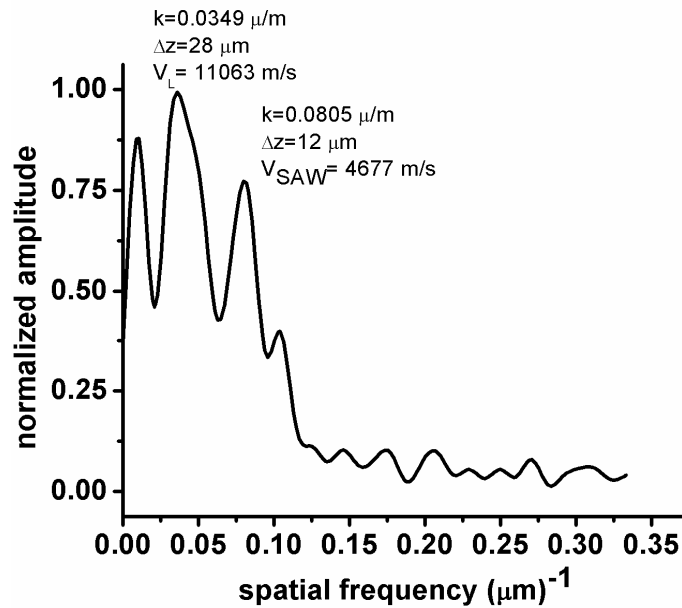


Figure 3.7: Fourier spectrum of the AMS curve of Figure 3.6 showing presence of multiple wave modes

The spatial frequency for longitudinal wave is observed at wave number $k=0.0349 \mu\text{m}^{-1}$ corresponding to $\Delta z=28 \mu\text{m}$. Substituting the distance between two successive peaks (Δz) and frequency in equation 3.4, the speed of SLAW is determined as 7091 ± 10 m/s. Similarly, numerical exercise is carried out for SAW generated peaks. The spatial frequency of SAW wave is $0.0805 \mu\text{m}^{-1}$ corresponding $\Delta z=12 \mu\text{m}$, from which the wave velocity is calculated as 4677 m/s. The values of SLAW obtained directly from the AMS curve and Fourier transform of AMS curves are 6354 ± 130 m/s and 7091 ± 10 m/s, respectively. Since

AMS does not show a large number of peaks and dips for accurately computing Δz from successive dips for SAW and SLAW the results obtained from the Fourier Transform of the AMS curve are more reliable. Table 3.2 summarizes the velocities obtained from the Fourier transform values. The velocity of ultrasonic waves in AlN determined from scanning acoustic microscopy is compared with the acoustic velocity determined from Brillouin light scattering (Carlotti *et al.*, 1995). In both experiments reactive RF-magnetron sputtering in a Nitrogen atmosphere was used for thin film preparation. Due to experimental variations and different constraint conditions some difference (within $\pm 10\%$) in the determined longitudinal wave velocity was observed when compared with the values reported in other publications.

3.4.8 Acoustic Dispersion Relation for AlN Film

It is important to study the acoustic angular wave dispersion and Lamb wave dispersion relationship in AlN for multilayered systems. The dispersion relation facilitates the study of interaction of bulk and Lamb wave modes in thin AlN films. The dispersion relationship helps in controlling fabrication processes of the AlN to achieve the required material properties and corresponding velocities for its potential application as bulk wave resonators.

In order to study the angular wave velocity dependence on the material parameter, Christoffel's equation is solved. The constitutive relationship for the anisotropic solid is given by (Pensala *et al.*, 2002)

$$\sigma_{ij}(y) = C_{ijkl}(y)\epsilon_{kl}(y) \quad (3.14)$$

The equation of motion of isotropic material is given as

$$\rho \frac{\partial^2 u_i}{\partial t^2} = \frac{\partial \sigma_{ij}}{\partial x_j} \quad (3.15)$$

The displacement field generated by a plane-wave is given by $\vec{u} = Ue^{i(\omega t - \vec{k}\vec{r})}$, where ρ is the density, t is time, ω is the angular frequency, k is wave number and u is displacement field. Christoffel's equation is solved for eigen values of aluminum nitride. Angular velocity of longitudinal wave mode and two quasi-transversal wave modes are plotted in figure 3.8. For isotropic solids, two quasi-transversal wave modes propagate with the same velocity.

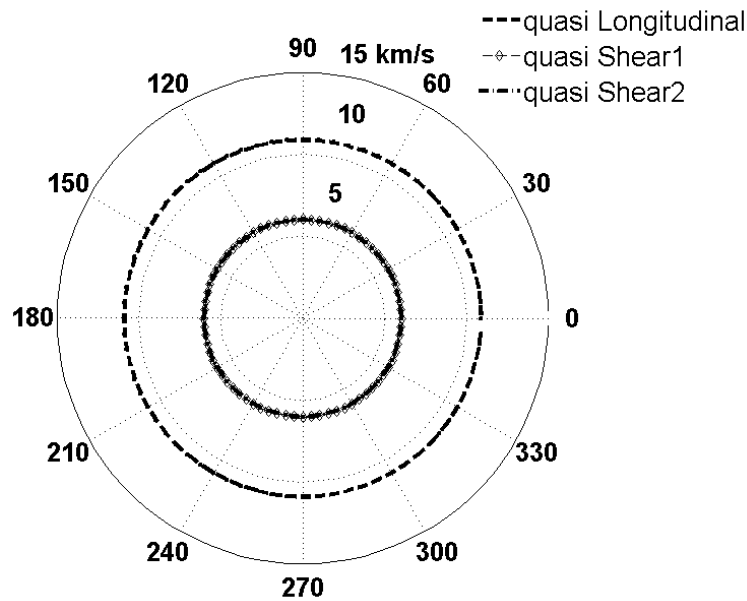


Figure 3.8: Angular dependence of ultrasonic bulk wave velocities (in km/s) for Aluminum nitride

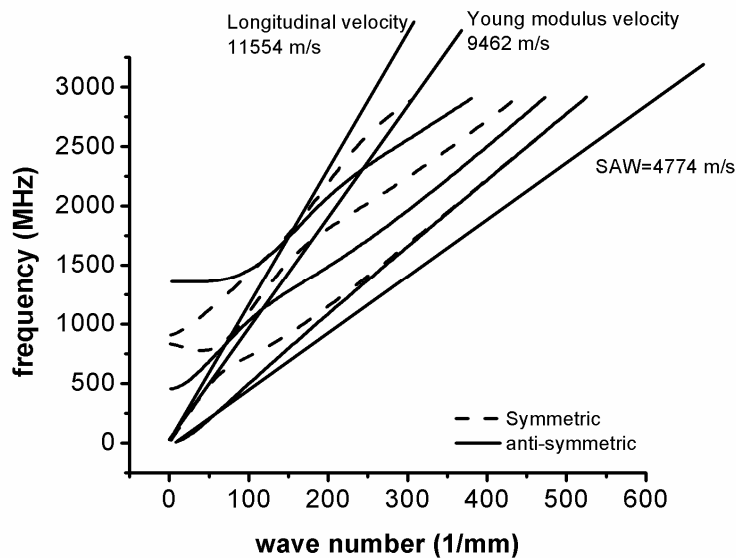


Figure 3.9: Dispersion relations for symmetric and anti-symmetric wave modes in 6.6 μm thick AlN film. Continuous lines indicate anti-symmetric modes and dotted lines are symmetric modes. The slope of lines represents SAW, Young's modulus wave (or bar wave) velocity and longitudinal wave velocity.

Based, on the material parameters determined from SAM and nanoindentation the dispersion relationship for the investigated AlN film is plotted in figure 3.8 (Pensala et al., 2002). The dispersion relationship indicates the dependence of ultrasonic wave velocity with excitation frequencies, thickness and material properties. In figure 3.9, the continuous lines

show anti-symmetric Lamb wave modes and dotted lines show symmetric Lamb wave modes. These dispersion relations are linear since both group and phase velocities do not depend on frequency for the displayed range. They are indicated as limit values for the Lamb wave modes. The asymptotic line along the fundamental anti-symmetric mode represents the speed of the surface acoustic waves estimated to be 4774 m/s. At large wave-numbers (low wavelength) and high frequency the velocities of SAW and transversal wave converge. The tangent to the fundamental symmetric Lamb wave mode represents bar wave velocity (square root of E/ρ), where E is Young's modulus or elastic stiffness ρ is the material density. Sometimes the bar wave velocity is also known as the Young's modulus wave velocity. It is the speed supported by AlN film in the uni-axial stressed state, which is determined to be 9462 m/s. The slope of the line connecting the branching of the anti-symmetric and symmetric wave modes indicates the longitudinal wave velocity.

3.4.9 Conclusions

The morphology, crystalline structure, and crystalline orientation of the AlN film significantly affect the acoustic velocities. The AlN film has a wurtzite structure with a highly preferred c-axis orientation. The surface roughness, thickness and orientation of the thin film were determined using atomic force microscopy and scanning electron microscopy. The mechanical property of the AlN was determined using scanning acoustic microscopy at 1.2 GHz and nanoindentation test (Young's modulus of 304 GPa). The longitudinal and surface acoustic wave velocities were experimentally determined using the defocusing of the lens and thus obtaining the acoustic material signature curve. Analyzing SAM and nanoindentation results, the material properties were obtained. The Lamb wave dispersion relation and bulk wave angular dispersion relationship are then numerically obtained to investigate the behavior of the acoustic wave mode propagation within the thin AlN films.

3.5 Mechanical Characterization of Sintered Piezoelectric Ceramic Material Using Scanning Acoustic Microscope

Summary

Lead zirconate titanate (PZT) is a piezo-electric ceramic material that needs to be characterized for its potential use in microelectronics. Energy dispersive X-ray spectroscopy (EDX) analysis is conducted to determine the chemical composition of the PZT ceramics. The scanning electron microscope (SEM) is performed to study the surface morphology, grain structure and grain boundaries. The SEM image helps us to understand the surface wave propagation and scattering phenomena by the PZT and the reason for its anisotropy and inhomogeneity due to the grain structure. In this paper scanning acoustic microscopy at 100 MHz excitation frequency is conducted for determining mechanical properties of PZT. Earlier works reported only the longitudinal wave speed in PZT while in this paper longitudinal, shear and surface acoustic wave speeds of sintered PZT are measured from its acoustic material signature (AMS) curves, also known as $V(z)$ curves. AMS or $V(z)$ curve is the variation of the output voltage as a function of the distance between the acoustic lens focal point and the reflecting surface. The average velocities of longitudinal, shear and surface acoustic waves in a PZT specimen are determined from its $V(z)$ curve generated at 100 MHz excitation frequency and found to be over 5000 m/s, over 3000 m/s and between 2500 and 3000 m/s, respectively. From these velocities all elastic constants of the specimen are obtained.

3.5.1 Introduction

Lead zirconate titanate $Pb(Zr_xTi_{1-x})O_3$ (PZT) crystals are increasingly used in excitation and detection of Lamb waves in aircraft integrated structures for structural health monitoring and nondestructive testing (NDT) (Haertling, 1999, Jaffe *et al.*, 1971, Shelke *et al.*, 2011b). Bulk wave resonators are manufactured from phase matching PZT layers. PZT layers are used for the generation and detection of surface and bulk acoustic waves because they have unique ferroelectric and electromechanical properties (Foster *et al.*, 1991, Fujii *et al.*, 1995, Maeder *et al.*, 1996). Sintering of thin PZT films is a challenging task due to the difficulty in achieving uniform density of fine sintered ceramics. Also, the evaporation of

PbO above 850°C degrades the piezo-electric material, affects its mechanical properties, and causes cracking due to thermal and acoustical mismatch (Gebhardt *et al.*, 2007).

During sintering and compaction processes inhomogeneity and anisotropy are inherently induced in the sample. Electrical and mechanical properties of PZT are determined from its orientation in the ferromagnetic domain. In order to obtain nano-scale resolution thin PZT films are characterized by, scanning electron microscopy (Maeder *et al.*, 1996), double beam laser interferometry (Chen *et al.*, 1995), neutron diffraction (Corker *et al.*, 1998), X-ray diffraction (Griswold *et al.*, 1995), Raman spectroscopy (Rouquette *et al.*, 2006), electron diffraction measurements (Glazer *et al.*, 2004), and many other techniques. However, none of the above techniques provides quantitative measurement of the elastic properties of the PZT ceramics. The near field atomic force microscopy with ultrasonic vibrations on the tip of a cantilever has been exploited for topographic characterizations and also to determine the resonance and localized elastic characterizations (Rabe *et al.*, 2002). Double beam interferometer is widely accepted for determination of longitudinal piezoelectric coefficient for thin piezoelectric films. Recently, scanning laser Doppler vibrometers (SLDV) have been used to characterize composite thick films (Wang *et al.*, 2005). Friend *et al.*, (Friend *et al.*, 2001) have characterized the poling in lead zirconate titanate ceramics using scanning acoustic microscope at 50 MHz and 100 MHz frequencies. They only calculated the longitudinal wave speed from the time of flight difference between the echoes from the two surfaces of the specimen. Average longitudinal wave velocity thus calculated was 4233 m/s. The resonating frequency of 1 mm thick PZT was determined by point source excitation and detection using Coulomb coupling (Habib *et al.*, 2012a). The excitation was done by 25 ns short rectangular pulse using 1.57 mm diameter steel sphere and resonance was observed at 4.85 MHz (Habib *et al.*, 2012a). Rabe *et al.*, (Rabe *et al.*, 2002) have characterized the elastic stiffness of the surface of PZT ceramic specimens using acoustic force microscopy. The technique was suitable only for plotting the stiffness variation image of the ceramic surface and does not reveal information of the bulk of the material. So far bulk properties of sintered PZT specimens are mostly unknown. Most of the ultrasonic characterization techniques are localized in space and does not provide reasonable estimate of the bulk mechanical properties of the PZT. The proposed methodology determines the quality of the poling and distribution from the acoustic wave velocity of longitudinal as well as slow and fast transversal wave modes. The estimate of Young's modulus of elasticity, shear modulus and Poisson's ratio are

evaluated from single measurement unlike any other technique. The proposed methodology is equally suitable for both thin and thick composite PZT transducers. Furthermore, the aim of the study was not just to characterize the PZT but also to propose an alternative methodology to determine longitudinal, slow and fast transverse wave speeds from a single measurement.

In order to quantify the particle size distribution and geometrical dimensions of piezo-sintered particles scanning electron microscope (SEM) generated images of PZT are analyzed. Scattering at the grain boundaries and damages at the grain level cause attenuation of the acoustic waves propagating through sintered PZT. Also, SEM images demonstrate the relative compaction and damage state of the piezo-sintered materials.

In the present study the longitudinal bulk wave speed, the quasi-transversal bulk wave speed and the surface wave speed of sintered PZT are calculated from its acoustic material signature (AMS) curve. In this manner its complete elastic properties are quantified. Since the sintering and compaction process of manufacturing of piezo-ceramic materials has a lot variability, it is not surprising that the longitudinal wave speed reported in the present study is higher than that reported by (Friend et al., 2001).

In the present study a scanning acoustic microscope (SAM) with a point focused transducer (focal length 5.9 mm) was used in the reflection mode on a 1 mm thick PZT ceramic specimen. The transducer was excited with a narrow pulse of width 18 ns at 100 MHz central frequency. For characterization of isotropic solids point focus (Every & Deschamps, 2003) lens is used while for anisotropic solids line focus beams (Kushibiki et al., 1989, Kushibiki & Chubachi, 1985, Briggs & Kolosov, 2009), non-coaxial symmetric (Briggs & Kolosov, 2009, Hildebrand & Lam, 1983, Grill *et al.*, 1996) and inclined probes are preferred to excite direction dependent mode selective surface acoustic waves. The acoustic lens with spherical concavity can produce point focused beam. Varying the defocusing distance by moving the lens focal point away from the reflecting surface of the specimen one can produce acoustic material signature (AMS) curves. Normally reflected rays, surface skimming longitudinal acoustic waves (SLAW) and leaky surface acoustic waves (LSAW) (Every & Deschamps, 2003, Kushibiki et al., 1989, Briggs & Kolosov, 2009, Hildebrand & Lam, 1983) contribute to AMS. The AMS or $V(z)$ curves show the variation of the output voltage (V) as a function of the lens focal point distance (z) from the reflecting surface of the specimen under inspection. An oscillating $V(z)$ curve is the manifestation of

surface acoustic waves and/or surface skimming longitudinal waves (Every & Deschamps, 2003, Briggs & Kolosov, 2009).

3.5.2 Experimental Technique

3.5.3 Scanning Acoustic Microscopy

Different piezoelectric ceramic materials have been characterized by others (Grill et al., 1996, Shelke et al., 2011b). In this investigation a piezoelectric ceramic plate of dimension $(20 \times 20 \times 1) \text{ mm}^3$ is studied. The conducting electrode in the form of silver paint was etched from the PZT surface with 1:3 solution of nitric acid (70%, 15 molar) and distilled water. The piezoelectric plate has relative ease of mobility of ferro-electric components and polarization. Properties of the piezoelectric material are given in Table 3.3 (PI). The piezoelectric ceramic has high curing temperature, high permittivity, high coupling factor, and low coefficient of thermal expansion which is desirable for low power non-resonating broadband ultrasonic applications (Shelke et al., 2011b).

Table 3.3: Electromechanical and Acoustical Mechanical Properties of the PZT

Elastic Constant (Compliance) (S_{11}) m^2/N	16.1×10^{-12}
Piezo-electric charge constant (d_{33}) C/N	400×10^{-12}
Frequency constant (Hzm) N_A	2000
Frequency constant (Hzm) N_R	1450
Piezo-electric Voltage constant (10^3) Vm/N	25
Density (g/cm^3)	7.8
Curie Temperature ($^\circ\text{C}$)	350
Permittivity (in direction of polarization) (ϵ_{33} / ϵ)	1750

The scanning acoustic microscope was equipped with a broad band acoustic transducer excited at central frequency of 100 MHz (PVA TePla Analytical systems GmbH, Westhausen, Germany). The low frequency (wide opening angle) lens was not used in the study as it suffers from the problem of predominant generation of leaky surface waves from the lens edges. Also, at low frequency lens, the ultrasonic waves experience interference pattern. Due to interference, it is difficult to identify individual longitudinal mode, transversal

modes (fast and slow) and surface acoustic wave mode in the transient signal. Additionally, the methodology at 100 MHz would also be suitable for mechanical characterization of thick and thin PZT composites as well.

3.5.4 Scanning Electron Microscopy Analysis

Scanning electron microscopy experiments were performed to investigate the surface morphology of the PZT. The microstructure and the phase purity of the ceramic were determined from the scanning electron microscopy (SEM, CamScan). Figure 3.10 shows the SEM micrograph of the PZT ceramic and figure 3.11 shows a similar image with 10 times more magnification compared to figure 3.10. The SEM images indicate the possibility of inhomogeneous and anisotropic behavior of the sintered PZT ceramic material. The impedance mismatch arises due to the changes in the density, material property and geometric property which causes ultrasonic wave scattering. During the compaction process of PZT ceramic, the sintered particles are crushed and damaged. The localized changes in density during compaction and breakage of grains together causes changes in localized impedance of the PZT resulting in pronounced effect on ultrasonic wave scattering.

Along the surface of the specimen the isolated pockets show significant damage of some particles. Such damages can significantly alter the piezoelectric properties within the crystal and generate noise. In this manner SEM images provide a qualitative estimate of the PZT quality and help to explain the heterogeneity of elastic properties in the ceramic specimen.

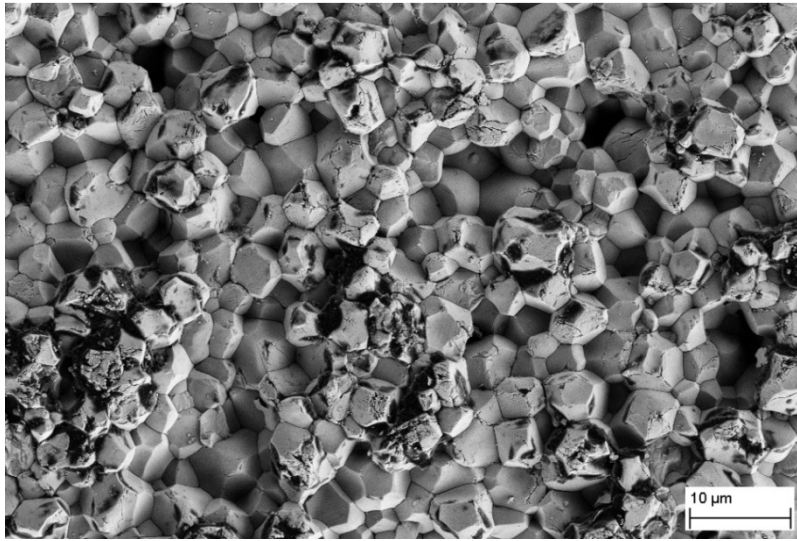


Figure 3.10: Scanning electron micrograph of 1 mm thick PZT sintered ceramic specimen

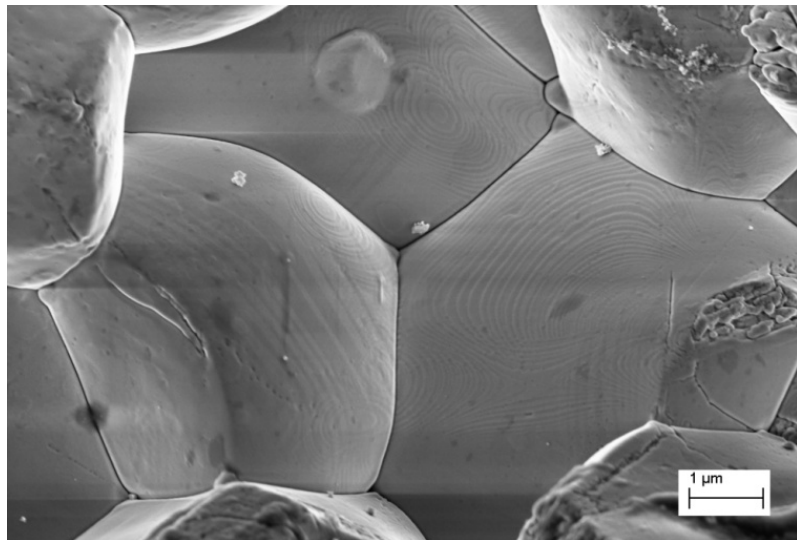


Figure 3.11: Scanning electron micrograph of 1 mm thick PZT sintered ceramic specimen (Magnification: 10 times that of Figure 3.10)

Figure 3.12 shows the particle size distribution of the piezo-sintered particles. The y axis shows the number of particles and the x axis shows the average particle diameter in μm . The mean diameter of the sintered particles is $4.29 \mu\text{m}$ and the standard deviation is $0.67 \mu\text{m}$.

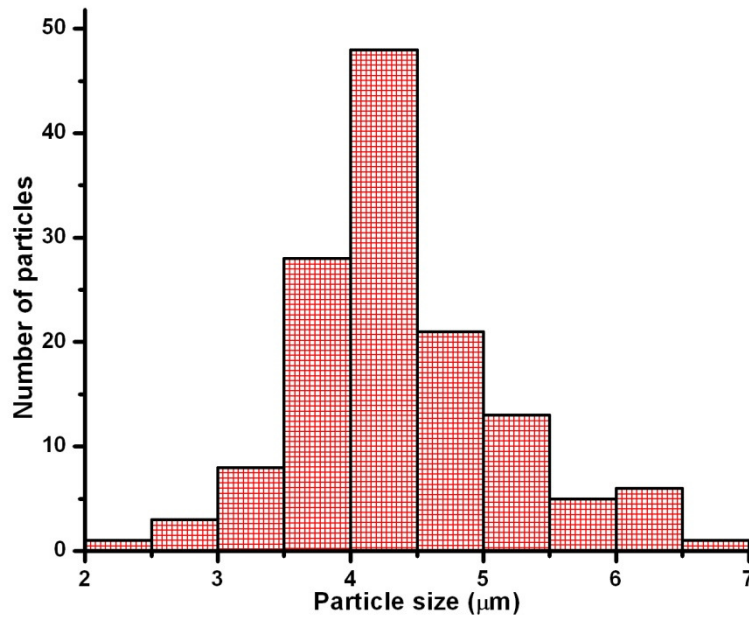


Figure 3.12: Particle size distribution of 1 mm thick PZT ceramic specimen - average diameter of the sintered particle was in the range 4.0–4.5 μm

Surface acoustic waves are strongly affected by the particle size and the roughness of the sintered material. The ultrasonic waves are usually scattered by the asperities of the relatively rough surface of the PZT specimen. The particle diameter of the sintered material was determined between 3.5 and 5 μm (Figs. 3.10-3.12). Since the characteristic roughness of the sintered material and the particle size distribution are comparable to the acoustic wavelength, significant wave attenuation due to scattering is expected. The focal spot dimension was around 15 μm and therefore ultrasonic wave scattering plays a major role in acoustic characterization of PZT.

The ultrasonic signal strength decays during its propagation through a PZT specimen due to scattering. Scattering is significant, if the particle size exceeds one-hundredth of the wavelength. Rayleigh scattering is proportional to the third power of the grain size and fourth power of the frequency for wavelengths greater than the particle size (Glegg, 1980). Detailed investigation of the effect of the particle size on the scattering of ultrasonic waves is outside the scope of this work and is not discussed any more.

3.5.5 Energy Dispersive X-ray Spectroscopy

The chemical composition and purity of PZT ceramics is determined using energy dispersive X-ray spectroscopy (EDX) analysis. Figure 3.13 shows the presence of Pb, Ti, Zr, and O with an average atomic percentage, which is rich in lead and oxygen.

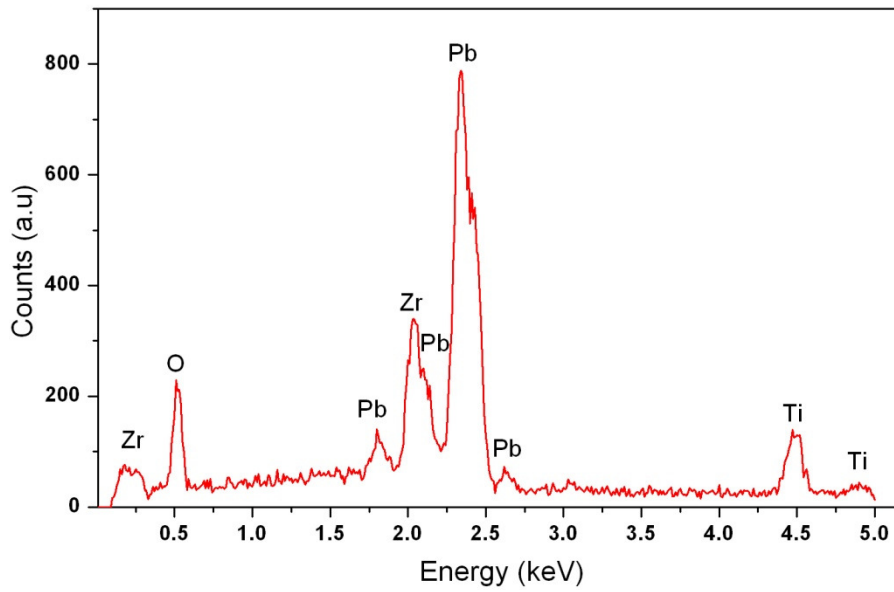


Figure 3.13: EDX spectrum of the PZT ceramics

According to the EDX analysis, the main elements detected are Pb (58.58 %), O (22.56%), Zr (12.82%), and Ti (6.04%). Table 3.4 shows a complete list of the elements in atomic percentage and their uncertainties that closely agreed with the values reported in the literature (Huang *et al.*, 2006).

Table 3.4: Chemical composition of PZT

Elements	Percentage composition (%)	Error in % (\pm)
Pb	58.58	1.05
O	22.56	0.57
Zr	12.82	0.35
Ti	6.04	0.35

3.5.6 Results and Discussions

Figure 3.14 shows the transient signal of the echo from the scanning acoustic microscope at an excitation frequency 100 MHz. The excitation pulse and the multiple echoes

due to lens reverberations were suppressed. The transient signal shows arrivals of different waves. The transient signal strength is shown in arbitrary units. The first arrival time of the wave packet generated by the surface skimming longitudinal acoustic wave was identified at $12.07 \mu\text{s}$ and denoted as SLAW in figure 3.14. The second peak in the transient signal was observed at $12.53 \mu\text{s}$ and identified as fast transversal wave (denoted as F-T). The peak arriving at time $12.73 \mu\text{s}$ represents slow transversal wave (S-T). At $12.79 \mu\text{s}$ the leaky surface acoustic waves were observed and denoted as LSAW.

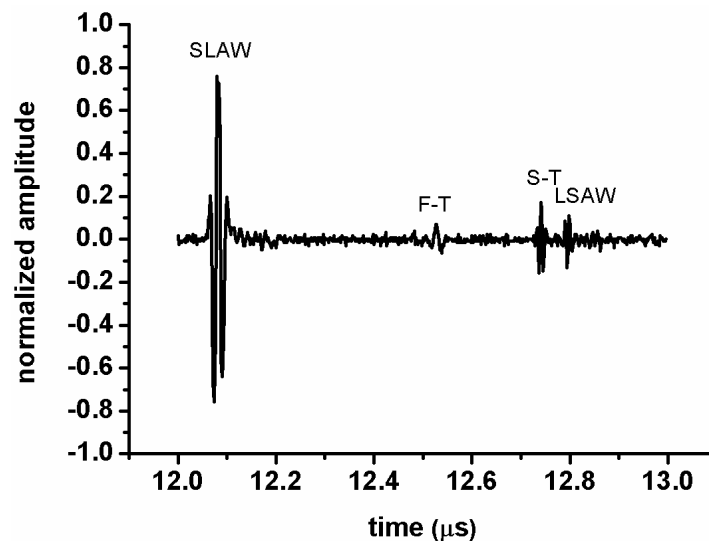


Figure 3.14: Normalized transient signal amplitudes recorded with focal point on the surface of the 1 mm thick piezo-sintered ceramic specimen. Four peaks correspond to the surface skimming longitudinal acoustic waves (SLAW), the fast transversal (F-T), the slow transversal (S-T) and the leaky surface acoustic waves (LSAW)

The time difference between the SLAW and F-T, F-T and S-T, and S-T and LSAW were 460 ns, 200 ns, and 60 ns, respectively. The peak of the frequency spectrum of SLAW wave packet was observed at 90 MHz and plotted in figure 3.15. The peak frequencies for the F-T and S-T wave packets were observed at 45 MHz and 55 MHz, respectively. The peak of the frequency spectrum of the LSAW wave packet in the transient signal shown in figure 3.14 was observed at 100 MHz (figure 3.16). The clear difference in the dominant frequency content in different wave packets ensures that they correspond to different wave modes as identified in figure 3.14 and are not generated by multiple reflections of the same wave packet between the sample and the acoustic lens.

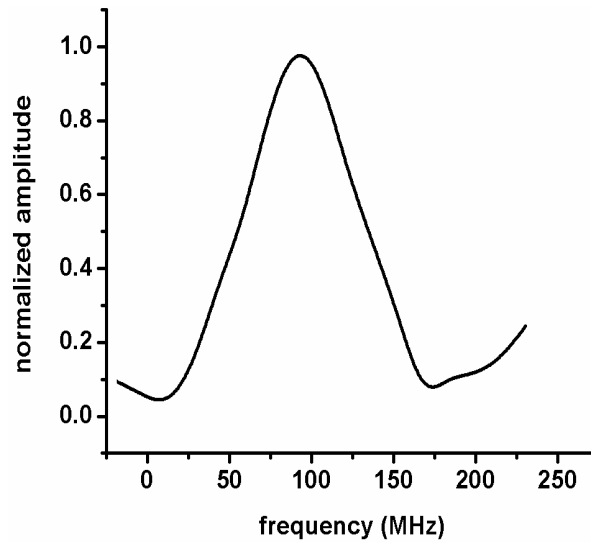


Figure 3.15: Fourier transform of the echo of SLAW wave packet of the transient signal shown in Figure 3.14 - the peak of the spectrum was observed at 90 MHz

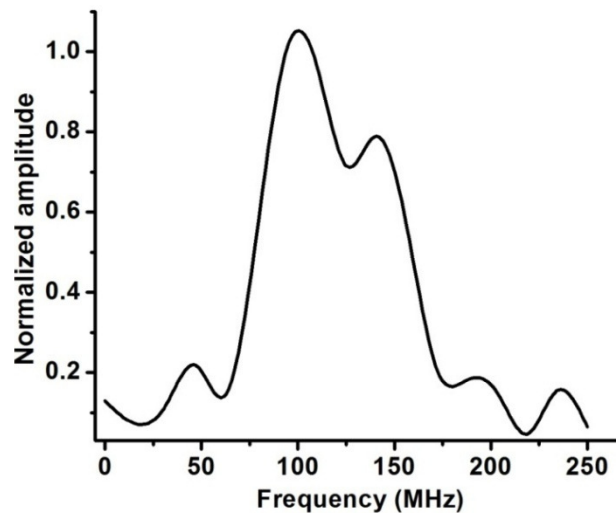


Figure 3.16: Fourier transform of the echo of LSAW wave packet in the transient signal shown in figure 3.14 - the peak of the spectrum was observed at 100 MHz

Figure 3.17 shows the experimental acoustic material signature curve generated by a point focused acoustic beam. The AMS curve (figure 3.17) is obtained by plotting the total energy (E) of the transient signal at each step of increment of the z value, as the lens focal point is moved within the sample (figure 3.1a). This energy is calculated from the formula $E = \sum_{n=-\infty}^{\infty} |A(n)|^2$, where n are the sampling points and $A(n)$ is the amplitude of the n^{th} sampling point. Surface acoustic waves, surface skimming longitudinal acoustic waves and their interference contribute to AMS.

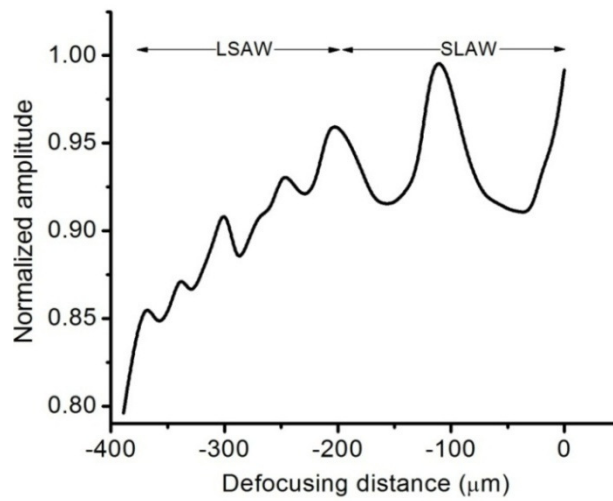


Figure 3.17: Acoustic Material signature (AMS) curve for 1 mm thick piezo-sintered ceramics at 100 MHz excitation frequency

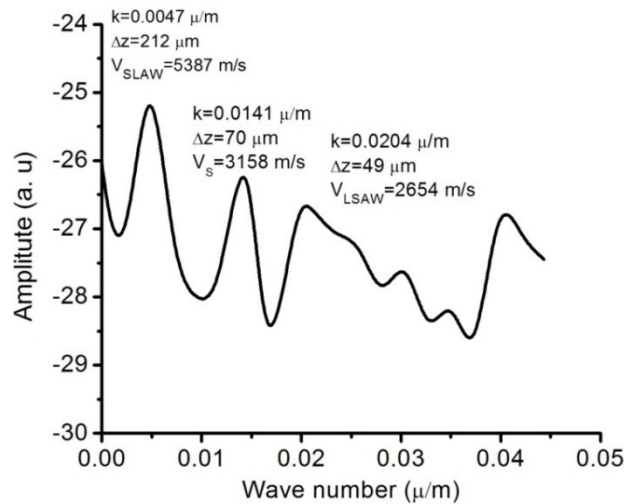


Figure 3.18: Fourier spectrums of the AMS curve of figure 8 showing the presence of multiple wave modes

Surface acoustic waves are excited when the acoustic beam strikes the interface between the coupling fluid and the reflecting solid at a critical angle obtained from Snell's law, $\sin\theta_c = \frac{c_f}{c_{LSAW}}$. In the AMS or $V(z)$ curve several peaks and valleys correspond to interference between SLAW, F-T, S-T, LSAW and centrally reflected beam. The AMS curve of figure 3.17 clearly shows two distinct wave modes-presumably SLAW and LSAW. Two complete oscillations can be observed in the defocusing distance between 0 and 210 μm . The distance between two successive peaks or dips for the SLAW wave mode (ΔZ_{SLAW}) is 105 μm at central frequency 90 MHz (from figure 3.15). Substituting the AMS curve parameters in equation 3.4, the group velocity of the SLAW is determined as 5359 m/s.

Similarly, the average distance between two successive peaks or dips for the LSAW wave mode (ΔZ_{SLAW}) is 48 μm (determined from figure 3.17). The central frequency of Fourier transform of LSAW wave mode was 100 MHz (figure 3.16). The group velocity of the LSAW wave mode is calculated from the AMS curve as 2784 m/s.

The Fourier spectrum of the AMS curve helps one to resolve the presence of multiple wave modes. Figure 3.18 shows the Fourier transform of the AMS curve. In this curve three distinct peaks are visible and identified as SLAW, shear wave speed and LSAW, respectively. The Fourier spectrum of AMS represents the wave number in the spatial domain. The spatial frequency (wave number k) for SLAW is observed at $0.0047 \mu\text{m}^{-1}$ corresponding to $\Delta z=212 \mu\text{m}$ ($1/0.0047$). Substituting the distance between two successive peaks (Δz) and frequency in equation 3.2, the speed of SLAW is determined as 5387 m/s. Similar, numerical exercise is carried out for shear wave and LSAW generated peaks. The spatial frequency of shear wave is $0.0141 \mu\text{m}^{-1}$ corresponding $\Delta z=70 \mu\text{m}$ ($1/0.0141$), from which the wave velocity is obtained as 3158 m/s. For LSAW, $k=0.0204 \mu\text{m}^{-1}$, so $\Delta z=49 \mu\text{m}$ and corresponding wave velocity is 2654 m/s.

The two values of SLAW (5359 m/s and 5387 m/s) obtained directly from the AMS curve and from the Fourier transform of the AMS curves raise the issue about accuracy of either of the two computed values. Kushibiki *et al.*, (Kushibiki et al., 1989) and Kundu *et. al.*, (Kundu, 1992) have proposed from various numerical and experimental investigations that better reliability of wave velocity could be obtained from the Fourier transform of the AMS curves rather than the AMS curve itself.

If the calculated SLAW and LSAW are substituted in equation 3.6 then the shear wave velocity is calculated as $C_s=3019 \text{ m/s}$ which is close to the shear wave velocity calculated from the Fourier transform of the AMS curve 3158 m/s. This is the fast transversal wave. From the shear wave and longitudinal wave velocities the Poisson's ratio is calculated as 0.26 ± 0.03 . The Young's modulus and shear modulus of the PZT are calculated from equations 3.8 and 3.9 as $183 \pm 12 \text{ GPa}$ and $71 \pm 6 \text{ GPa}$, respectively.

The similar procedure is repeated at a central point and 0.5 mm, 1 mm, 2 mm and 4 mm away from the central point at $\pi/2$ intervals. Such localized arrangement of points is selected in space for easy interpretation of wave velocity in the isotropic sintered piezo-ceramic. Since the sintered PZT is isotropic and heterogeneous the variation in wave velocity

arises only due to localized changes in relative compaction of grains of ceramics. The average group velocity in a given area would not be strongly affected by the selection of random points on the heterogeneous surface of PZT.

The speed of SLAW and LSAW waves are determined and reported in Table 3.5. F-T wave velocity, Poisson's ratio, Young's modulus and shear modulus are computed from equation 3.6-3.9, respectively in table 3.5. A total of 17 data points (16 points are on the periphery of 4 circles and the 17th point is the central point as shown in tables 3.5 and 3.6) were used for the evaluation of elastic mapping of ceramics. The mean velocities of the leaky surface acoustic waves and the surface skimming longitudinal acoustic wave at 17 distinct points were determined as 2784 ± 122 m/s and 5359 ± 190 m/s, respectively.

Table 3.5: Sample summary of experimental results

Spatial or radial distance (mm) from centre	SLAW (m/s)				LSAW (m/s)				F-T (m/s)			
	0°	90°	180°	270°	0°	90°	180°	270°	0°	90°	180°	270°
0.5	5103	5373	5604	5503	2505	2654	2391	2620	2698	2860	2549	2814
1	5136	5458	5590	5487	2555	2589	2333	2669	2759	2779	2485	2870
2	5149	5396	5626	5500	2487	2745	2419	2668	2675	2965	2580	2870
3	5054	5329	5578	5478	2557	2668	2375	2575	2760	2880	2532	2760
0	5359				2784				3019			

Table 3.6: Calculated values of the elastic constant

Spatial or radial distance (mm) from centre	v (unitless)				E (GPa)				G (GPa)			
	0°	90°	180°	270°	0°	90°	180°	270°	0°	90°	180°	270°
0.5	0.3	0.3	0.36	0.32	150	167	145	165	56.7	63.8	50.6	61.7
1	0.29	0.32	0.37	0.31	157.0	162.3	137.8	169.4	59.3	60.2	48.1	64.2
2	0.31	0.28	0.36	0.31	149.1	177.6	146.9	170.2	55.8	68.5	51.9	64.2
3	0.28	0.29	0.37	0.32	155.8	169	137.2	163.57	59.4	64.6	50.06	59.4
0	0.26				183				71			

3.5.7 Conclusions

Velocities of leaky surface acoustic wave, surface skimming longitudinal acoustic wave and transversal waves in sintered PZT are measured for the first time using a 100 MHz point focused transducer in scanning acoustic microscopy. In acoustic microscopy, the defocusing of the focused beam within the sample produces Acoustic Material Signature (AMS) or $V(z)$ curve from which these velocities are obtained. The AMS curve exhibits the interference of the waves due to defocusing. Using a point focused acoustic lens in SAM detailed information of surface and subsurface elastic properties of a material can be obtained in this manner with the help of $V(z)$ curve. The qualitative knowledge derived through SEM and quantitative information from SAM coupled together provides the propagating and scattering behavior of the acoustic waves in PZT. The technique could well be adopted for deriving anisotropic behavior of piezo-crystals and ceramics with high resolution in the lateral direction.

4 Methodology: Coulomb Coupling

4.1 Coulomb Coupling

Acoustic waves propagation in anisotropic materials is a complicated and fundamental problem, mainly as group and phase velocity directions often differ from each other (Auld, 1993, Kino, 1987). Excitation and detection of acoustic waves in piezoelectric materials relies on a gradient in the piezoelectric properties respectively a gradient in the electric field. The relatively weak coupling is usually enhanced for established practical applications by mechanical, geometrical and electrical resonances. In this respect, wave excitation and detection from conductive point sources offer an interesting physical phenomena insight into crystal properties, as special directions may exist in which acoustic energy are focused.

In the Coulomb field of scanned electrically conductive local probes and similar detection has been employed for imaging of the transport properties of acoustic waves in piezoelectric materials including single piezoelectric crystal. In piezoelectric crystals the coupling between elastic and electric variables influences the acoustic modes and their propagation. Through this coupling the strain field of an acoustic wave is accompanied by an electric field, which in turn increases the stress field. The crystal thus appears elastically stiffened, and the phase velocity, the group velocity, and the polarization of the wave are altered. The transfer of energy between an electromagnetic field or wave and acoustic waves by piezoelectric coupling is governed by the gradient of the electric field and the grading of the piezoelectric properties.

Conductive tips in contact or near the surface of piezoelectric materials can act as approximate point sources of acoustic waves in the material, if they are driven with an AC voltage of appropriate frequency. This is true, because the oscillatory electric field can be generated with an effective lateral extension below the diffraction limit for the generated acoustic waves. Similarly, such point probes can also be used for detection with a spatial resolution close to or exceeding the diffraction limit for the generated acoustic waves. By employing two such tips on the same surface or opposite surfaces of piezoelectric sample the acoustic wave's propagation can be observed with the aid of a two-dimensional scan of one of the tips. Gated sinusoidal generation and transient quadrature detection yields temporal resolution far below the propagation time in the crystal and allows to distinguish different acoustic modes propagating in the crystal.

4.2 Experimental Setup for Coulomb Coupling Excitation and Detection

The experimental set-up for the Coulomb coupling excitation and detection of bulk waves in LiNbO₃ single crystal and in PZT has been reported in detail previously (figure 4.1) (Habib *et al.*, 2006, Habib *et al.*, 2012a). Two motor-driven translation stages were used in order to position the probe used for excitation in two dimensions parallel to the sample surface. The motors were controlled by a computer via a serial interface. Two small pieces of glass fibers (diameter about 100 μm) were glued together with epoxy, such that the fibers form an angle of approximately 60°. A steel sphere of 1.57 mm diameter was then glued to the contact point of the two glass fibers and electrical contact was established with a thin wire. The other ends of the glass fibers were glued to an aluminum holder and were mounted to the translation stage. The scanner moved the probe across the sample surface, while the transient ultrasound was registered and averaged for each position. The typical scan area was 5×5 mm², which was centered relative to the detector tip below the sample.

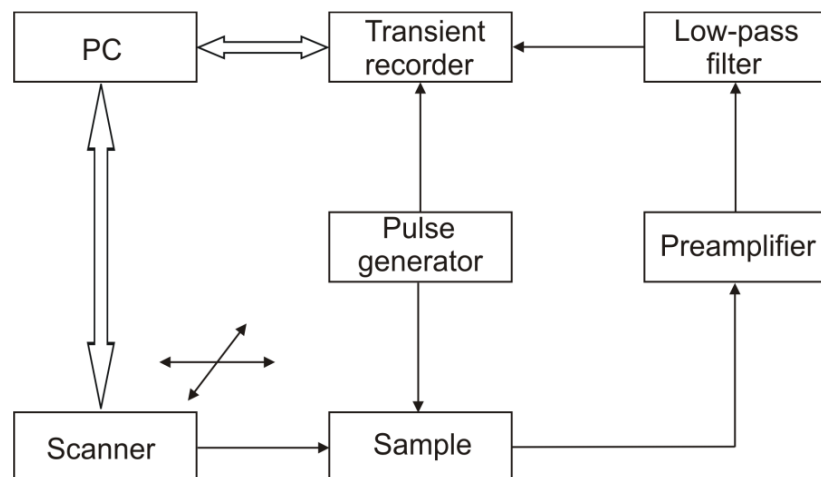


Figure 4.1: Schematic diagram of the signal generation and detection through Coulomb coupling in 1 mm thick piezo-sinter plate

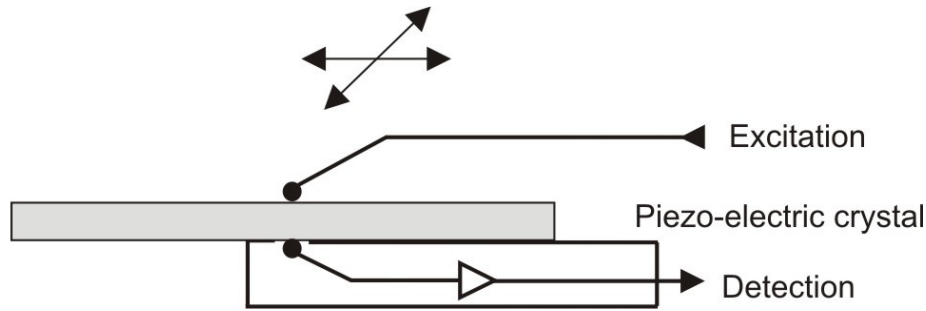


Figure 4.2: Schematic diagram of piezoelectric excitation and detection of ultrasound

In figure 4.2 the electrical fields at both tips with the black dots represent small spheres couple to acoustic waves via the piezo-effect and respective inverse effect at both surfaces in a highly localized way due to sideways restrictions by the rapidly dropping approximate Coulomb (electric) field. Imaging is performed by 2D scanning of the probe used for excitation and recording of the extended time dependent signal for any pixel of the image.

A short pulse, Dirac like excitation was delivered for excitation with a duration of 25 ns (approximately, 2 oscillations), then used to drive the probe for excitation of the acoustic waves in the piezoelectric sample. During the scan, signal was picked up from the other side of the PZT plate with the aid of another steel sphere (1.57 mm) probe. In the receiving side, an amplifier amplifies the signal and then delivered into a low-pass filter. After filtering out the high frequency, the low frequency component was digitized by an 8 bit 100 MHz maximum sampling rate of the transient recorder. The respective analysis is performed by post-experimental processing of the acquired three-dimensional (position in two dimensions and time) data set. The transient signal was acquired at 512×512 pixel points for the acquisition time of 22 μ s in 5×5 mm² scan area. As compared to the time-selective boxcar technique, it enables one to record multiple time delay images in one scan allowing variable gating of the recorded signal by processing of the stored data. The described data acquisition technique has been used previously with conventional focusing ultrasound transducers (Twerdowski *et al.*, 2006). As compared to the time-selective boxcar technique (Grill *et al.*, 1996), it enables one to record multiple time delay images in one scan allowing variable gating of the recorded signal by processing stored data.

4.3 Quadrature Detection Scheme

Quadrature detection is a phase sensitive demodulation. It is also called quadrature demodulation, phase quadrature technique, vector detection, or phase quadrature heterodyne demodulation technique. Quadrature detection is almost universally used in both magnetic resonance imaging (MRI) and Doppler ultrasound (Medcyclopaedia). Basically, it's a technique to filter components out of a measured signal, which are of the same frequency as a pure sine wave reference (or "carrier") signal and either in phase with the reference signal (0° component) or out of phase with it (90° component). This method is completely based on multiplication of the measured signal with such a reference signal of arbitrary phase and a reference signal whose phase is shifted by 90° relative to the first reference signal. The output of the multiplier is then delivered into a low-pass filter in order to remove the high-frequency components generated during multiplication. The cut-off frequency of the filter, f_c (or ω_c , for angular frequency) should be chosen below the frequency of the reference signal, but such that the remaining bandwidth is sufficient in order to observe changes of the signal amplitude at the reference frequency on the required time scale. Quadrature detection gives all the necessary information such as amplitude, phase and frequency.

The concept of modulation comes from the simple trigonometric identity:

$$\cos(x)\cos(y) = \frac{1}{2}\cos(x+y) + \frac{1}{2}\cos(x-y) \quad (4.1)$$

If we assume that the message signal is a pure tone of frequency (f_m), then the message can be mathematically represented as $\cos(2\pi f_m t)$. The same assumption can be made about the carrier signal, thereby expressing it as $\cos(2\pi f_c t)$. Assumption of the "pure tone" makes the mathematics much more tractable. However, it is also necessary to keep in mind that the message signal is rarely a pure tone. Typically, it is composed of time variations in amplitude, frequency, phase, or any combination thereof. Even the carrier need not necessarily be a pure sinusoid. Applications exist in which the carrier signal is a square wave with a fundamental frequency f_c . The harmonics of f_c inherent in the square wave are dealt with by low-pass filtering the modulated signal. The mixing process mentioned earlier can be thought of as a multiplication operation. Therefore, the trigonometric identity above may be employed to represent the mixing process as follows:

$$\cos(2\pi f_c t)\cos(2\pi f_m t) = \frac{1}{2}\cos[2\pi t(f_c + f_m)] + \frac{1}{2}\cos[2\pi t(f_c - f_m)] \quad (4.2)$$

Thus, the mixing of the message and carrier results in a transformation of the frequency of the message. The message frequency is translated from its original frequency to two new frequencies one greater than the carrier ($f_c + f_m$), and one less than the carrier ($f_c - f_m$), the upper and lower side bands, respectively. Furthermore, the translated signal undergoes a 6 dB loss (50 percent reduction) as dictated by the factor of $\frac{1}{2}$ appearing on the right hand side of the equality. The form of modulation just described is referred to as “double sideband modulation,” because the message is translated to a frequency range above and below the carrier frequency. Another form of modulation, known as single sideband modulation, can be used to eliminate either the upper or lower sideband.

A quadrature modulator mixes the message with two carriers. Both carriers operate at the same frequency, but are shifted in phase by 90° relative to one another (hence the “quadrature” term). This simply means that the two carriers can be expressed as $\cos(2\pi f_c t)$ and $\sin(2\pi f_c t)$. The message, too, is modified to consist of two separate signals: the original and a 90° phase shifted version of the original. The original is mixed with the cosine component of the carrier and the phase shifted version is mixed with the sine component of the carrier.

These two modifications result in the implementation of the single sideband function. Trigonometrically, this can be expressed as:

$$[\cos(x)\cos(y)] + [\sin(x)\sin(y)] = \cos(x - y)$$

Note that the right-hand side contains only the lower sideband. In the above equation, x is the carrier and y is the message. Incidentally, changing the sign of the operator on the left-hand side of the equation results in only the upper sideband appearing on the right hand side. However, the message is shown as a band-limited spectrum rather than a pure tone, which better represents a real-world application. Each constituent frequency in the message is translated to one or both sides of the carrier, as shown above.

4.4 Experimental Setup for Local Electrical Field Probe Technique

Figure 4.3 shows the schematic diagram of the local electric field probe for excitation and detection of surface acoustic wave in piezo-electric crystal on the same surface of the crystal.

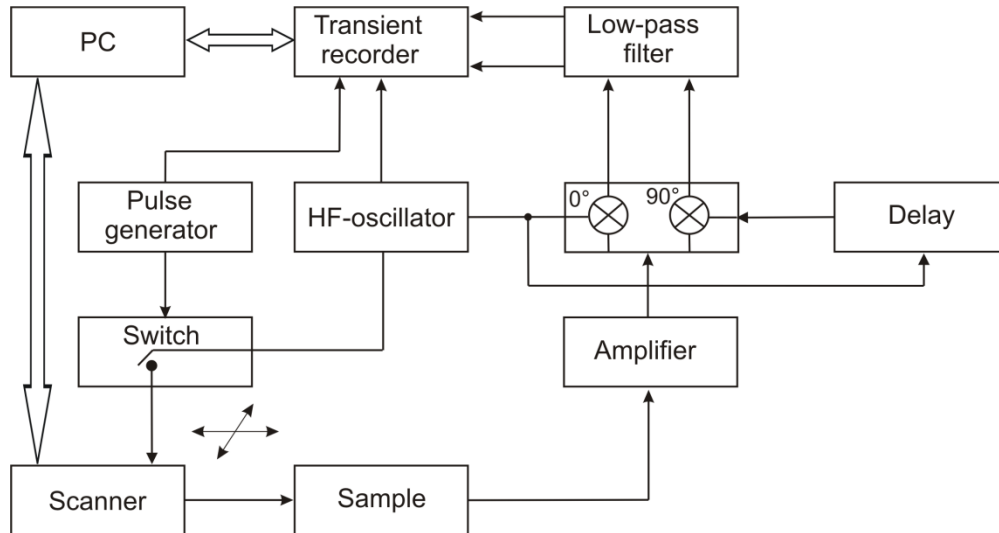


Figure 4.3: Schematic representation of the signal generation, detection, and processing for the Coulomb excitation and detection

The electrode for excitation and detection was fabricated from a 50 μm gold wire, wrapped around a bronze wire (figure 4.4). Two 200 μm bronze wires were crossed in order to form a triangular lever holding the electrode to insure that it was in contact with the sample.

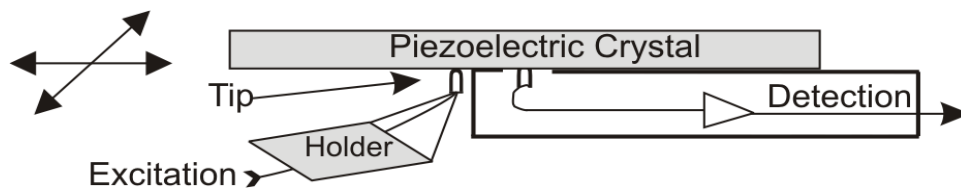


Figure 4.4: Schematic diagram of piezoelectric excitation and detection of ultrasound

The exciting electrode was positioned by a stepper motor driven 2D translation stage on the surface of the crystal. It was scanned line by line over the imaged surface region during the experiment. The distance between the lines was set to 10 μm . The receiving electrode was placed at a fixed position on the same surface of the sample. It connects to an amplifier in a metallic box acting as a Faraday cage. The minimum distance between the exciting and receiving probes is limited by the Faraday cage to about 0.5 mm. The scan area for the images displayed here has been set to 5 \times 5 mm².

An excitation burst with a carrier frequency of 89.9 MHz, gated to 220 ns (approximately, 20 oscillations) is cut from a continuous wave (CW) generated by a stabilized CW oscillator with the help of an electronic switch controlled by a pulse generator. The amplified signal is delivered to the moveable local electric probe employed for excitation. The exciting and receiving local electric probes together with the piezo-effect and

inverse piezo-effect of the crystal converts the electrical signal to mechanical oscillation and vice-versa. The received signal was amplified and processed by two channel quadrature detection (vector detection). For this purpose the received signals was submitted to the two-channel multiplier. In the first channel (0°), the signal was multiplied with a reference CW signal used for the exciting burst. A time delay corresponding to the 90° phase shift was introduced to the reference CW signal by an additional cable prior to feeding to the multiplier channel two (90°).

The multiplied signals were low-pass filtered in order to remove the high-frequency components (double the frequency of the oscillator and higher order contributions) generated by multiplication. After filtering the signals were digitized by a two channel 8 bit 89 MHz sampling rate transient recorder. From the two acquired waveforms, both amplitude as well as phase are determined using the Pythagorean theorem and the inverse tangent. The transient recorder operated with an external sampling clock derived from the stabilized CW oscillator, which, together with synchronization of the internal clocks of the pulse generator and CW oscillator allowed for “coherent” sampling and complete elimination of the jitter of the acquired signal.

The flow chart shown in fig 4.3 summarizes again the data acquisition. The raw input signal was an analog signal whose amplitude varies continuously over time. Dedicated software can display, manipulate and analyses the data in a wide variety of ways. Most of the parameters that affect acquisition can be set by the user through the software. In order to achieve a good image quality, the parameters must be appropriate for the signals being recorded. Sampling replaces the original continuous analog signal by a series of discrete values (samples) taken at regular time intervals. The appropriate sampling rate depends on the signal to be measured. If the sampling rate is too low, information is irreversibly lost and the original signal will not be represented correctly. If it is too high, there is no loss of information, but the excess data increases processing time. Recordings of periodic waveforms that have been sampled too slowly may be misleading as well as inaccurate because of aliasing.

For preventing aliasing, the sampling rate must follow the Nyquist theorem. Any analog waveform can be described mathematically as the sum of a number of pure sine waves at various frequencies and amplitudes (Fourier decomposition). A filter removes selected frequencies from a signal: for instance, a low-pass filter allows low frequencies to pass and

blocks high frequencies. Low-pass filters are commonly used to help reduce noise and give a smoother signal. A high-pass filter removes any steady component of a signal; it also removes slow fluctuations. Filtering can change the signal to some extent: its use must be balanced against the distortions it can remove, such as noise, baseline drift, and aliasing. Filtering can also be applied to the recorded digital data after acquisition. Smoothing functions help to remove noise, clutter, and unwanted high frequencies from signals. These act as simple low-pass filters by averaging adjacent data points, but shouldn't be used as substitutes for the correct low pass filter during recording. They are most useful in helping clean up signals recorded at high sampling rates.

5 Imaging of Acoustic Waves in Piezoelectric Ceramics by Coulomb Coupling

Summary

The transport properties of bulk and guided acoustic waves travelling in a 1 mm thick lead zirconate titanate (PZT) disc, originally manufactured to serve as ultrasonic transducer, have been monitored by scanned Coulomb coupling. The images are recorded by excitation and detection of ultrasound with local electric field probes via piezoelectric coupling. A narrow pulse with a width of 25 ns has been used for broad-band excitation. Broadband coupling is achieved since neither mechanical nor electrical resonances are involved. The velocity of the observed acoustic waves traveling along the plate is experimentally determined as 4610 ± 230 m/s and 3865 ± 95 m/s and compared with characteristic velocities calculated from material properties listed by the manufacturer of the PZT plate.

5.1 Introduction

Lead zirconate titanate $\text{Pb}(\text{Zr}_x\text{Ti}_{1-x})\text{O}_3$ (PZT) has emerged as a highly effective piezoelectric ceramic material for generation and detection of ultrasound for frequencies typically up to 30 MHz. It has a widespread use in ultrasonic transducers (G. H. Haertling, 1999, Foster et al., 1991). Extensive research has been conducted in the last decades for optimizing the piezo-electric properties and characterization of PZT. On the other hand PZT is considered to be an important ferroelectric thin film material and has developed rapidly in recent years due to its potential applications in excitation of ultrasonic waves (Fujii et al., 1995, Maeder et al., 1996). PZT has a high piezoelectric coefficient and a high dielectric constant (about 1700) (H. Fu & R. E. Cohen, 1900, Chen et al., 1995, Low & Guo, 1995).

Thin PZT films are traditionally characterized by neutron and X-ray diffraction (Griswold et al., 1995), Raman spectroscopy (Rouquette et al., 2006), dielectric measurements, double beam laser interferometry (Chen et al., 1995), nanoindentation (M. Alguero *et al.*, 2002), scanning electron microscopy (Maeder et al., 1996), electron diffraction measurements (Glazer et al., 2004), and many others. PZT components manufactured from piezo-sinter materials exhibit isotropic and anisotropic behavior depending upon the manufacturing procedures. However, often during sintering and

compaction processes in-homogeneities and anisotropy can be induced in the samples. The in-homogeneities of the grain orientations in the polycrystalline material may induce localized anisotropy in the ceramic. In anisotropic materials the velocity of the acoustic waves depends on the direction of propagation and orientation of the anisotropy. These features are observed by imaging with the aid of scanned Coulomb excitation (Shelke *et al.*, 2011a). Due to the high dielectric constant of PZT the electric field at the contact area is concentrated sufficiently to represent in that respect an almost ideal point like point spread functions for the wavelength observed here concerning generation and detection.

The main task of this paper is to determine the response of a PZT disc as typically used for ultrasound transducers in dependence of position and time for a highly localized excitation with an approximate Dirac pulse structure in time. By time sequential imaging also the velocities of the observed waves can be determined, allowing the identification of the actual modes. The monitoring of the Dirac response in space and time represents furthermore a basis for the determination of any excitation that can be derived by simple linear superposition and respective integration over any given generation and detection area, usually defined by respective electrodes, as established for synthesized array techniques. The transfer of electro-magnetic energy to acoustic energy by Coulomb coupling in piezoelectric materials is governed by the gradient of the electric field and the gradient of the piezoelectric properties (Jacobsen, 1960).

The electric field concentrated at the tip of the employed probes and the discontinuity of material properties at the surface lead to the highly localized excitation and detection in the employed Coulomb coupling scheme. The fact that the piezo effect is in essence not frequency dependent and that frequency dependencies usually observed for piezoelectric transducers are caused by resonances and geometric interferences, both not present for the localized excitation and detection scheme as realized by Coulomb coupling, lead to the large bandwidth, only limited in the sinter material by Rayleigh scattering from the grains.

5.2 Experimental Results and Discussion

The evolution of acoustic waves in the 1 mm thick piezoelectric sintered PZT-ceramic plate is presented in the time sequential images in figure 5.1.

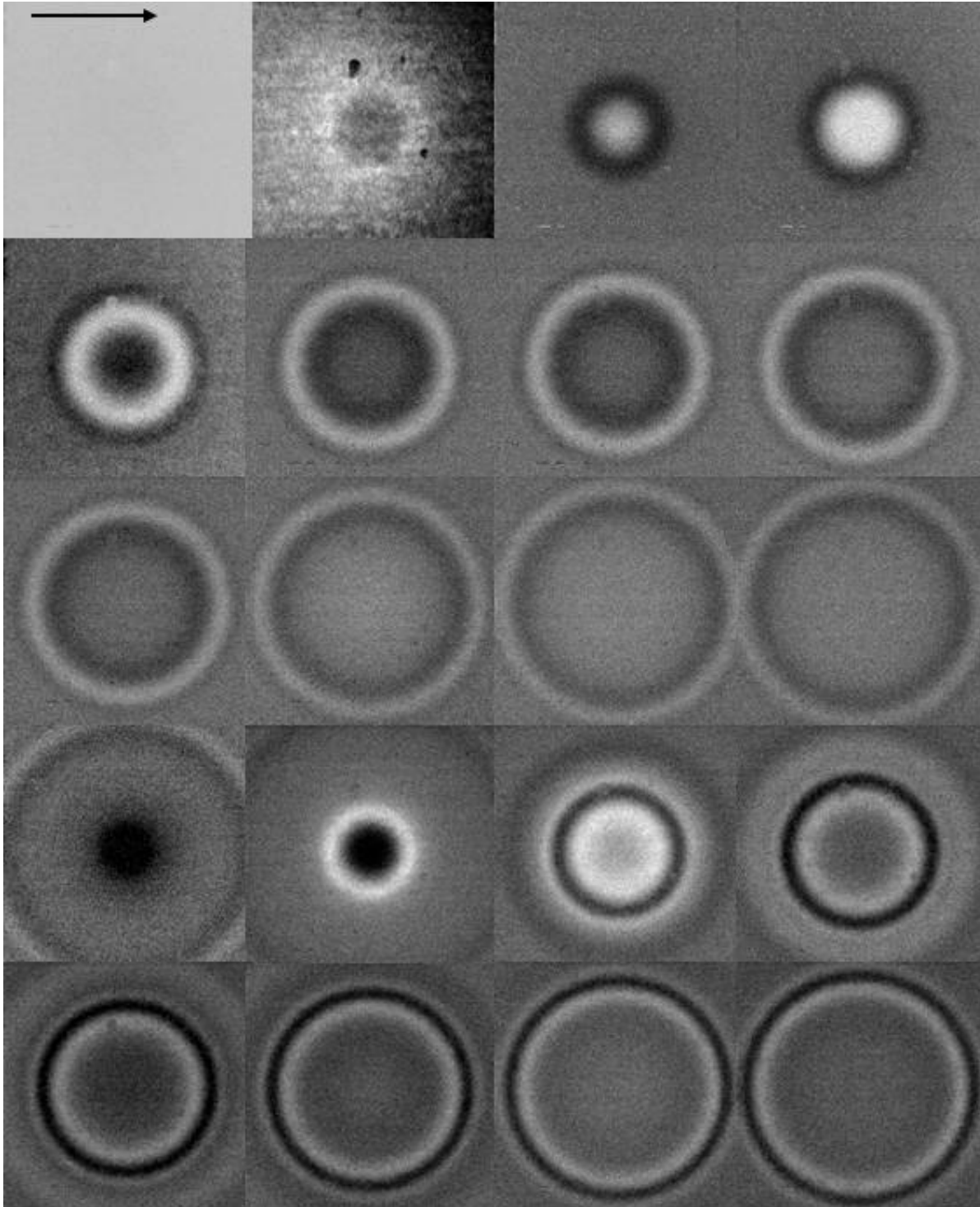


Figure 5.1: Transient evolution of magnitude of the propagating acoustic waves in a 1 mm thick piezo-sintered ceramic plate. The first response observed (2nd image from left in top row) is dominated by electrical crosstalk. Image size is each $3.5 \times 3.5 \text{ mm}^2$. Time steps between each frame are 55.5 ns

The second frame in the top row represents the signal dominated by electrical crosstalk from the excitation. The temporal response (figure 5.2) is dominated by crosstalk up to a time

of about 300 ns, depending in general on the position of the recording tip and dominantly determined by the time needed by the amplifier to recover from crosstalk. The black spots relate to non perfect material properties at the surface, leading to reduced sensitivity for the detection of acoustic waves. The brightness of the images relates to the amplitude observed with medium grey relating to zero.

The width of the pulse employed for excitation was 25 ns. The brightness of the images relates to the amplitude observed with medium grey relating to zero. The images represent a movie where the contrast relates to the amplitude of detected acoustic waves with 1 frame every 55.5 ns. Following the excitation the development of wave fronts traveling in radial direction along the scanned surface is observed. All observed acoustic waves show a circular structure with the center relating to the fixed position of the Coulomb probe employed for pick-up. Beside of a fine grained structure observed in the images the sample is homogeneous and furthermore isotropic concerning the transport properties of acoustic waves.

The normalized amplitude of the transient signal at a position of the scan, where the emitting and receiving probes are opposing each other, is displayed in figure 5.2. Beside of an intense overload from electrical cross talk from the excitation starting at time zero, an echo pattern is visible, relating to a repetition time of 636 ± 9 ns. Concerning a full roundtrip (2 mm) in the plane parallel 1-mm-thick sample (in normal direction to the scanned surface), this relates to a velocity of acoustic waves of 3144 ± 44 m/s.

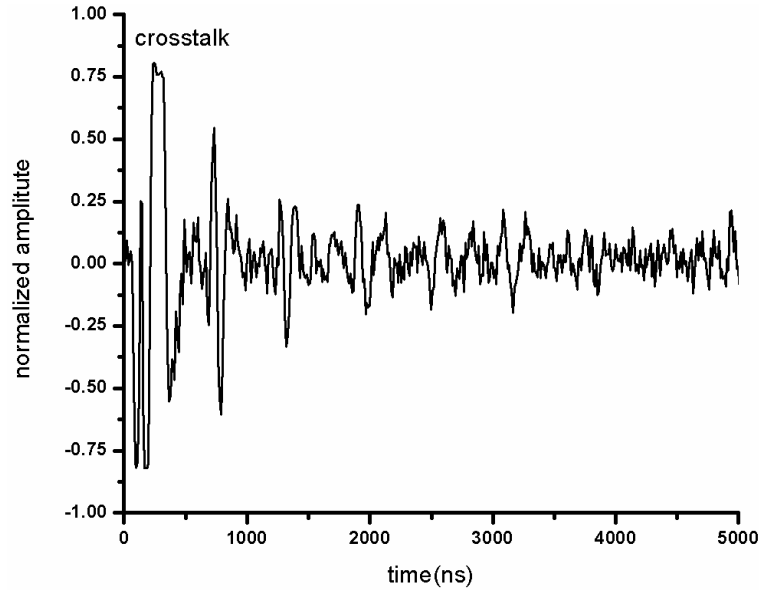


Figure 5.2: Normalized transient signal amplitudes recorded with the detecting Coulomb probe located at the opposing position with respect to the emitting probe on the other side of the piezo-sintered ceramic plate

From the material parameters supplied by the manufacturer of the sample (PI), the characteristic velocities have been derived (table 5.1).

Table 5.1: Characteristic velocities derived from material parameters

Material properties	Velocities (m/s)	
Density = 7.8 g/cm^3	Longitudinal bulk mode	4320
Young's modulus = $10 \times 10^{10} \text{ N/m}^2$	Transversal bulk mode	2170
Poisson's ratio = 0.33	Young's modulus limit	3550
	Surface acoustic wave	1950

The determined characteristic velocities represent asymptotic limit value for the dispersion relation of Lamb waves, displayed in figure 5.3.

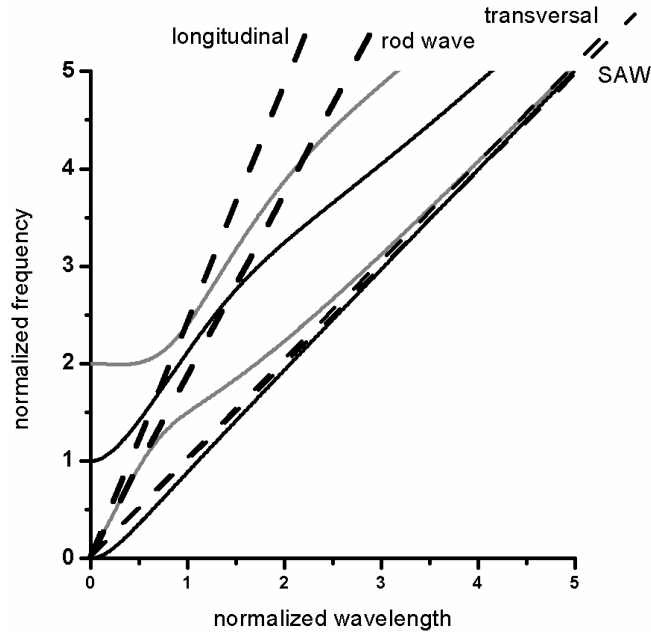


Figure 5.3: Dispersion relations for anti-symmetric (A0, grey) and symmetric (S0, black) Lamb wave modes for a 1 mm piezo-sintered ceramic plate

The determined characteristic velocities represent asymptotic limit value for the dispersion relation of Lamb waves, displayed in figure 5.3. In figure 5.3 the gray lines indicate anti-symmetric Lamb wave modes and black lines indicate symmetric Lamb wave modes. The dashed lines indicate, as identified, the dispersion relations for the respective surface and volume modes, respectively an idealized rod mode, as observed in the limit of an infinitely thin rod. These dispersion relations are linear since group and phase velocity depend both not on frequency for the displayed range. They are indicated since they represent limit values for the Lamb wave modes.

In order to determine the velocity of the observed acoustic waves traveling along the surface of the sample, a sequence of frames was analyzed for the first and second observed ring like structure traveling in radial direction. The results for the first and second ring is displayed in figure 5.4 and figure 5.5 together with a linear fit used to experimentally determine the bulk velocities in lateral direction.

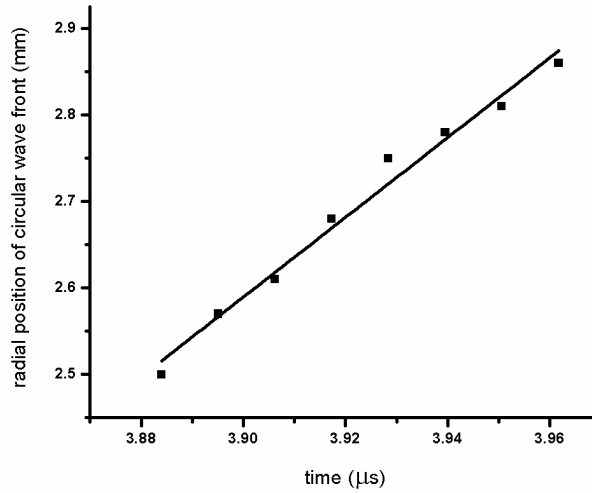


Figure 5.4: Experimentally determined position of acoustic waves traveling in lateral direction for first emitted ring. The velocities as determined by a least square fit are 4610 ± 230 m/s

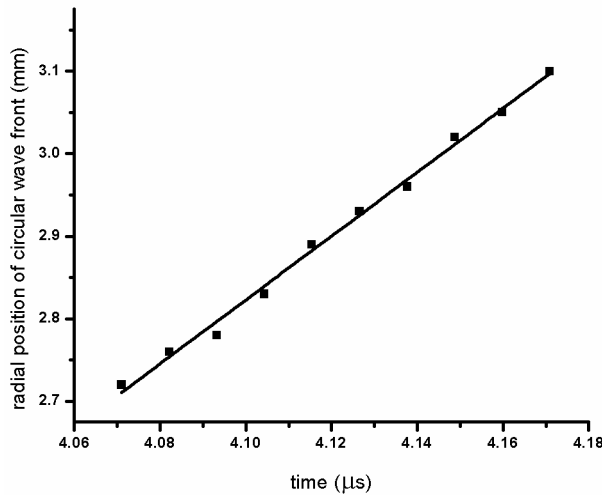


Figure 5.5: Experimentally determined position of acoustic waves traveling in lateral direction for second (right) emitted ring. The velocities as determined by a least square fit 3865 ± 95 m/s for the second ring

To present an image demonstrating NDT by coulomb imaging of not ideal samples, figure 5.6 shows the bulk wave propagation in a 1 mm thick PZT disc in the presence of adhering particles from conductive silver paint, which remained on the surface following incomplete removal of a conductive silver paint layer. Due to electrical conduction the conducting areas show a reduced contrast due to averaging and incomplete contact to the surface.

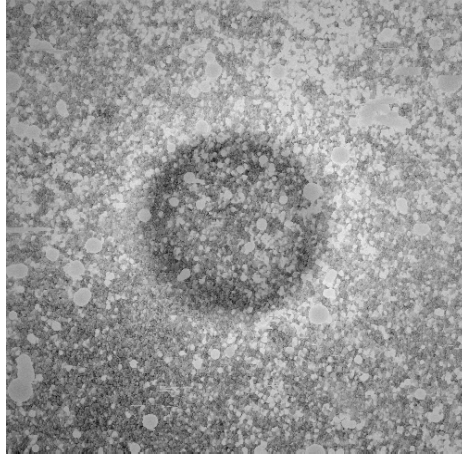


Figure 5.6: Transient evolution of magnitude of the propagating acoustic wave in piezo-sintered ceramic of 1 mm thick plate in presence of conducting silver paint as dirt. Image size is $5 \times 5 \text{ mm}^2$

5.3 Conclusion

Imaging of the propagation of acoustic waves in piezo-electric sintered PZT-ceramics is demonstrated with local probes for electric fields by Coulomb coupling. The time sequential monitoring of the acoustic waves excited by a short pulse reveal that the main contributions are emitted ring systems, where the first one observed close to the excitation travels with a velocity comparable to that of bulk waves if determined from the material parameters and the second one close to the velocity of S_0 Lamb waves in the long wavelength limit. The source of the periodic emission relates to a velocity of about $3144 \pm 44 \text{ m/s}$ for acoustic waves traveling normal to the plate surfaces. This velocity can not be clearly assigned to a bulk wave velocity, which may be due to deviations concerning the material parameters listed by the manufacturer of the material or to acoustic coupling of the spheres used for the Coulomb excitation and detection scheme. The observed ring like structures indicate the metamorphosis from the original localized excitation of bulk waves to guided waves, which are here only observed at the relatively close distance to the source, if compared to the thickness of the sample, for the second emitted ring structure, where the velocity has reached a value in accordance with the velocity of the S_0 mode of Lamb waves. Since similar plates are used as transducers for the excitation of Lamb waves in applications involving NDT and SHM by ultrasound, the here developed and applied method can be used as a basis for modeling by the experimentally gained point response observed by scanned imaging with Coulomb coupling.

6 Vector Contrast Imaging of Surface Acoustic Waves by Local Electric Field Probes

Summary

Excitation and detection of acoustic waves in piezoelectric materials relies on a gradient in the piezoelectric properties respectively a gradient in the electric field. The relatively weak coupling is usually enhanced for established practical applications by mechanical, geometrical and electrical resonances. Geometrical resonances, as present for the commonly used digital or inter-digital transducer (IDT), lead to limitations concerning the spatial and temporal resolution that can be achieved with local electric field probes. The propagation of surface skimming longitudinal waves (SSLW) and surface acoustic waves (SAW) on a 5 mm thick plate of lithium niobate (YZ cut) is monitored with spatial and temporal resolution. Excitation and detection are achieved with local electrical field probes at an excitation frequency of 89.9 MHz. The imaging is performed with switched sinusoidal excitation and quadrature detection, from which the magnitude and phase are derived. The wavelengths of SSLW and SAW are both determined from the observed phase rotation. The phase velocities for propagation along the Z-axis are $V_{\text{SSLW}}=(7.45\pm 0.1)$ km/s and $V_{\text{SAW}}=(3.56\pm 0.08)$ km/s, respectively.

6.1 Introduction

In physical acoustics, the visualization of individual acoustic wave fronts is one of the fundamental problems. The generation and detection of surface acoustic waves (SAWs) in piezoelectric crystals with the aid of digital or inter-digital transducer has attracted widespread scientific interest for signal processing and filtering applications (White & Voltmer, 1965). The velocity of acoustic waves (SAWs) is typically about five orders of magnitude smaller than that of electromagnetic waves. Due to these characteristics the SAW transducers can easily be manufactured by electrically conductive comb shaped structures (digital and inter-digital transducers; DT, IDT) in the frequency range varying from the upper MHz range to the lower GHz range (~ 2 GHz) (White & Voltmer, 1965). SAWs show a wave like behavior in the directions parallel to the surface and exhibit an exponential decay perpendicular to it.

For an effective excitation of the surface acoustic waves, the conventional combs like DT or IDT positioned on piezoelectric crystals are typically used. A wide range of experimental investigations on SAWs were implemented to detect and visualize the surface acoustic wave field, such as stroboscopic X-ray topography (Whatmore *et al.*, 1982, H. Cerva & W. Graeff, 1984, Capelle *et al.*, 2012), scanning acoustic force electron microscopy (Hesjedal *et al.*, 1999), immersed focusing transducers (Vines *et al.*, 1995), scanning electron microscopy (Roshchupkin *et al.*, 1994), and neutron scattering (Hamilton & Yethiraj, 1999). The SAW is also conventionally excited and detected using scanning acoustic microscopy (Ghosh *et al.*, 1997), scanning laser acoustic microscope (SLAM) (Robbins & Rudd, 1988), ultrafast optical excitation and detection (Sugawara *et al.*, 2002) and acoustic pulses on solid surfaces (Nishino *et al.*, 1993). At sufficiently low power densities, the excitation of acoustic waves is mainly due to thermal expansion within the crystal (Arnold *et al.*, 1985). The thermo elastic generated strains exist primarily parallel to the surface of the crystal. In addition to longitudinal and shear bulk waves, various SAW modes are also generated. However, the bandwidth of the excited SAWs in the plane of the crystal is limited due to temporal and spatial resolution of the laser spot (Hesjedal, 2010).

Wide band operation with angular independent emissivity respectively detected concerning phase velocities (v_p) can be realized with point like excitation or detection, where the actual diameter (given by D) of the local probe determines the upper cut-off frequency (ν)

given by

$$D = 2r_s = \frac{\lambda}{2 \cdot 0.12} = \frac{v_p}{0.24\nu}$$

Since the normal mask technology employed for IDT and DT requires conductive connections for contacting a local probe, represented by a respective circular conductive spot, this established technique is not well suited for point like excitation and detection. The technique introduced here relies on the third dimension to establish an electrically conductive link. The connecting conductor is kept at a sufficient distance from the surface with (low epsilon) air as dielectric, such that excitation or detection by the connecting paths is negligible (see figure 4.4 for principle of point probe design).

The main objective of this study is the application of the earlier developed Coulomb coupling scheme for the time dependent visualization of SAWs traveling on a piezoelectric crystal (LiNbO₃ 5 mm thick, both sides optically polished, YZ cut) by local electric field probes for excitation and detection. The local probes in combination with proper impedance

matching to avoid cable reflections are advantageous for wide band excitation and detection due to the absence of mechanical, geometrical and electrical resonances.

Phase and group velocities are derived from the propagation directions. The actual values are derived from the observed phase rotation per length of propagation. The group velocities relate to the direction of the vector connecting the origin with the point of observation and the periodicity of the phase observed in that direction. Only weak phonon focusing is observed when SAW caustics are not present as is the case for the employed crystal surface and therefore respective interferences do not occur.

6.2 Results and Discussions

The method presented visualizes the propagation of surface skimming longitudinal waves as well as SAWs propagating in the piezoelectric lithium niobate crystal under investigation. Figure 6.1 shows the normalized magnitude of the transient signal obtained at the midpoint of a line scan, 0.5 mm away from receiving electrode.

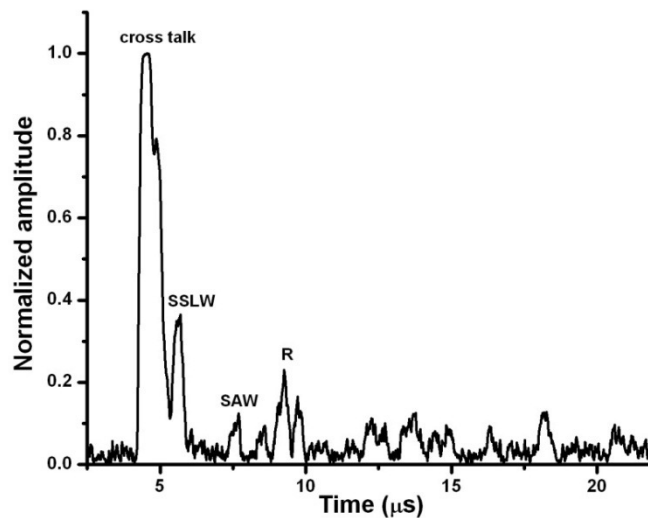


Figure 6.1: Normalized magnitudes of the transient signal recorded with an electrode located on the same side of the crystal as the exciting electrode

The evolution of surface skimming longitudinal and surface acoustic waves in the LiNbO_3 single crystal presented in the time sequential images of magnitude in figure 6.2

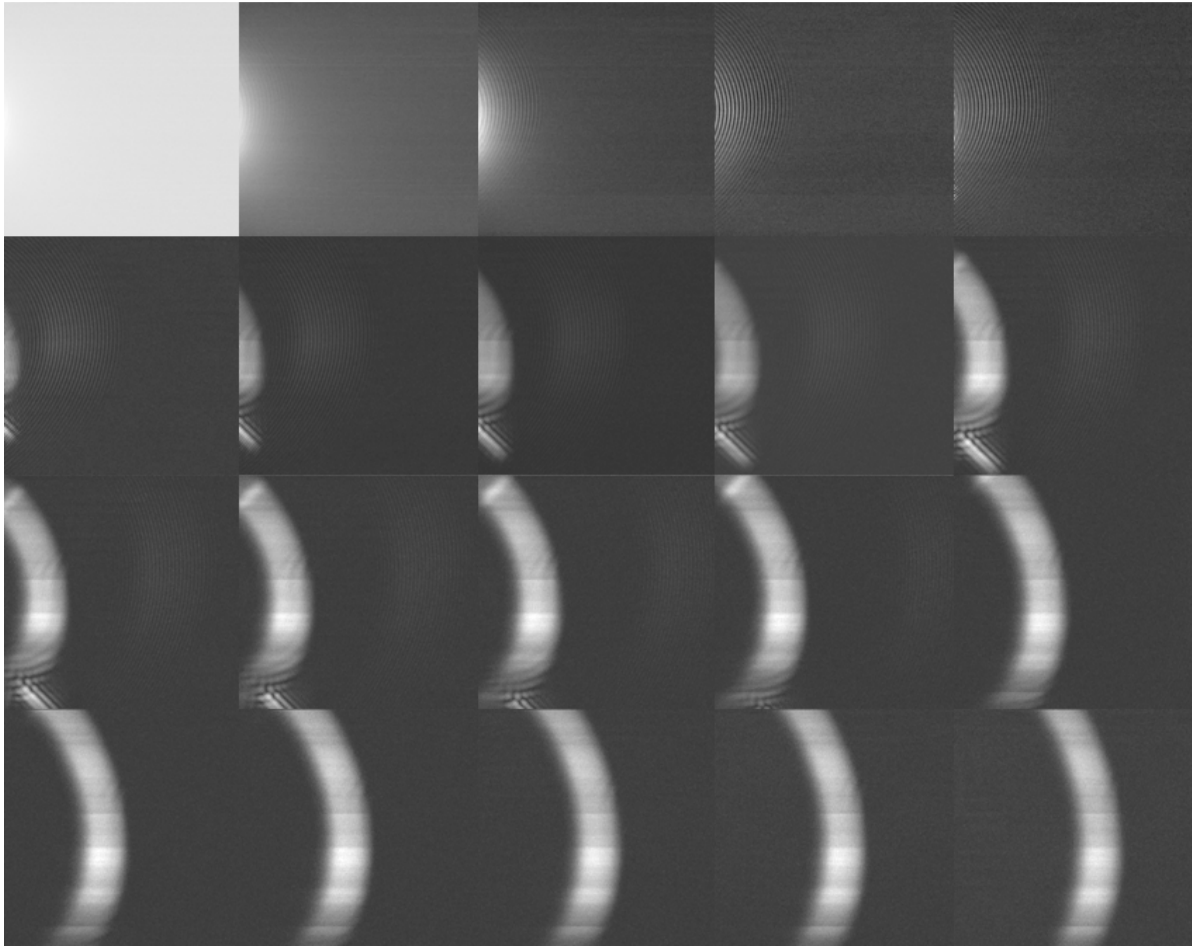


Figure 6.2: Transient evolution of magnitude of the propagating surface skimming longitudinal and acoustic waves in a LiNbO_3 single crystal. The first response observed (1st image from left in top row) is dominated by electrical crosstalk

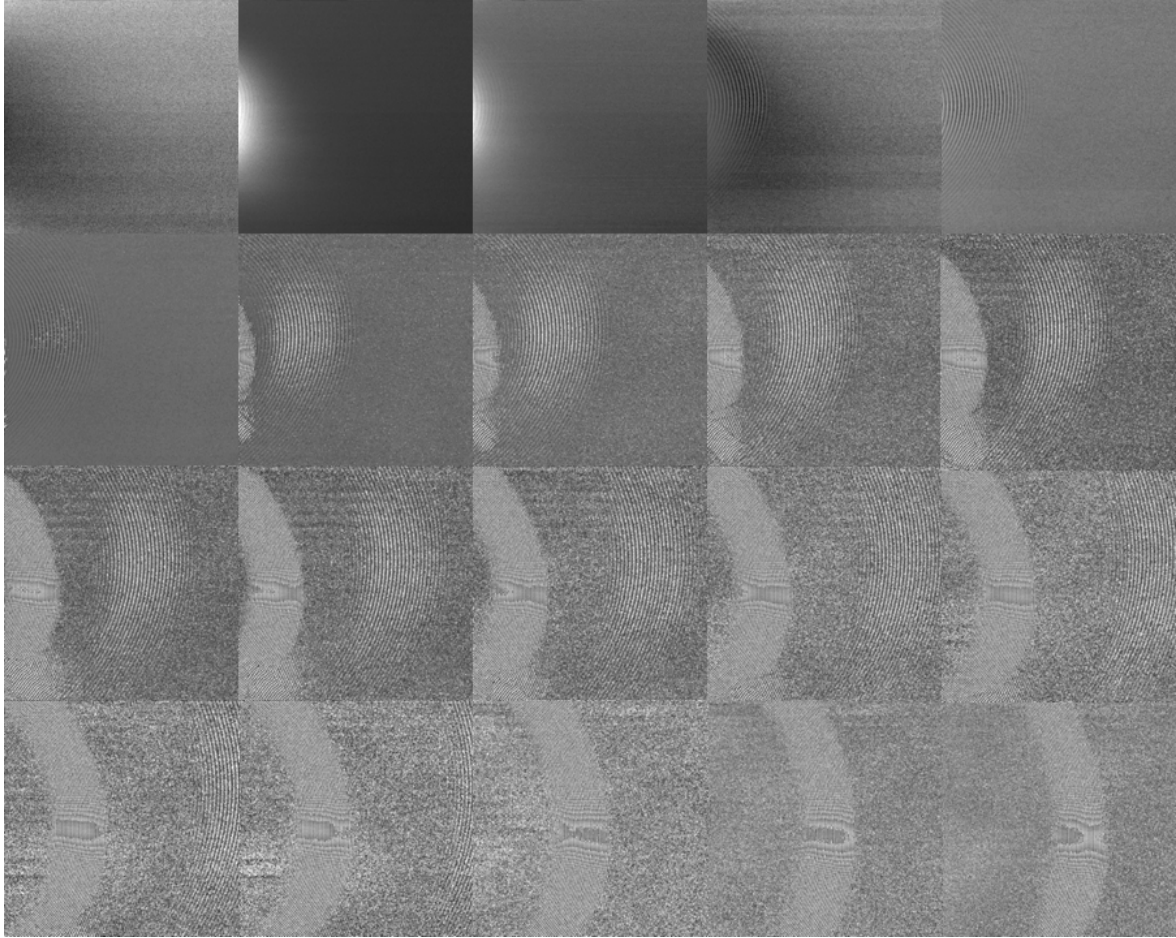


Figure 6.3: Transient evolution of phase contrast of the propagating surface-skimming longitudinal and surface acoustic waves in a LiNbO_3 single crystal. The first response observed (1st image from left in top row) is dominated by electrical crosstalk

Time gating applied to all acquired transient signals delivers the snapshots of the ultrasonic wave packages on the surface of the crystal. The first signal visible at $4.46 \mu\text{s}$ is due to electrical cross talk. This cross talk denotes the time of excitation (marked in figure 6.1). The subsequent signal at time $5.66 \mu\text{s}$ is due to the longitudinal polarized waves skimming along the surface (so called surface-skimming longitudinal waves, SSLW figure 6.4). Surface acoustic wave was observed at $7.69 \mu\text{s}$ in figure 6.5 (also marked by SAW in figure 6.1). At later time, bulk waves reach the surface under observation following reflections with and without mode conversions between the opposing surfaces of the plate (marked by R in figure 6.1).

In the experiment, the acoustic wave was recorded on the surface of a LiNbO_3 crystal. The group velocity of the longitudinal polarized acoustic bulk wave is about two times higher than that of the SAW's (Makkonen *et al.*, 2003). The surface acoustic waves are therefore

trailing the longitudinal waves travelling along the surface. This is also visible in the recorded transient (figure 6.1) and can also be observed in sequential images of magnitude and phase contrast in figure 6.1 and figure 6.2, respectively.

Figure 6.4 shows the phase and magnitude contrast image of the surface skimming longitudinal wave and surface acoustic wave propagation in the grey scale covering the range from 0 to 2π , encoding the phase rotation.

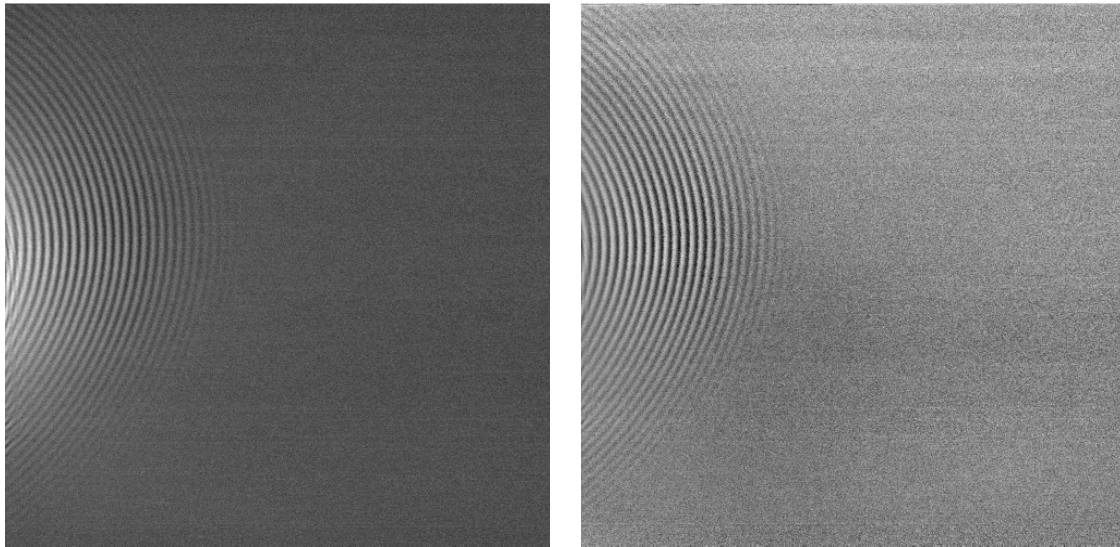


Figure 6.4: Scanned wave fields of the surface skimming longitudinal waves (SSLW). Image in magnitude contrast (left) and phase contrast (right) with full grey scale relating to 2π . The size of the images is $5 \times 5 \text{ mm}^2$

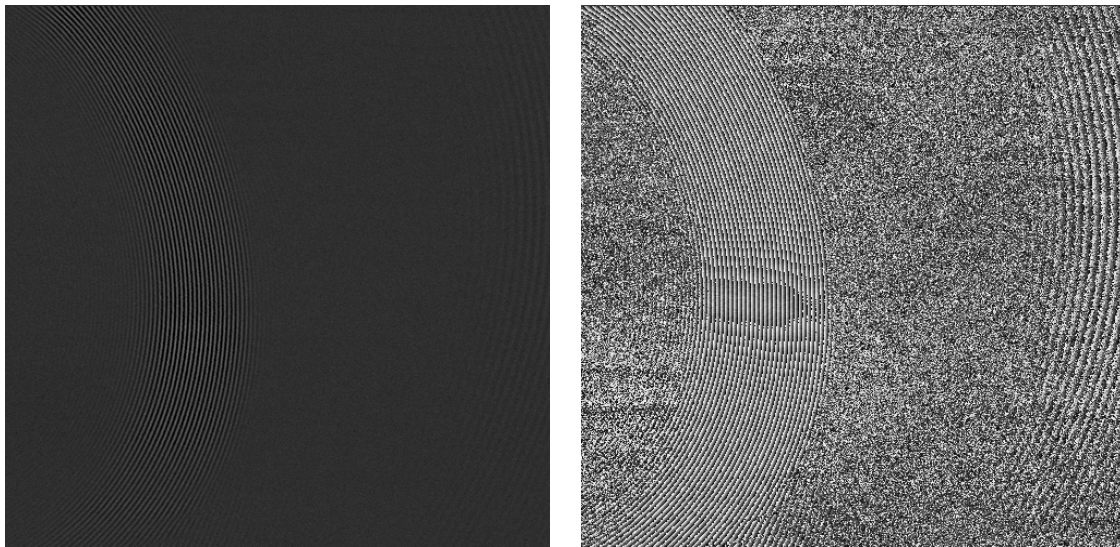


Figure 6.5: Scanned wave fields of the surface acoustic waves (SAW). The contrast in the image (left) is derived from the real part of the quadrature detection with medium grey

representing zero and phase contrast (right) with full grey scale relating to 2π . The size of the images is $5 \times 5 \text{ mm}^2$

The group velocity of the longitudinal waves is approximately twice the SAW velocity (Makkonen et al., 2003). Therefore, the longitudinal polarized waves precede the observed SAWs. On the other hand, the intensity of the longitudinal waves drops faster than that of the SAWs over the given characteristic length.

The wavelengths are determined from the change in phase of the observed wave packet. The wavelength of the longitudinal waves was $82.75 \pm 1.1 \mu\text{m}$ and the surface acoustic wave was $(39.6 \pm 0.88) \mu\text{m}$ for propagation along the Z-axis as determined from the phase images. The measured group velocity from the phase rotation (group and phase velocity are degenerate) of the surface skimming longitudinal waves is $V_{\text{SSLW}} = (7.45 \pm 0.1) \text{ km/s}$. The SAW velocity obtained from the measurement is $V_{\text{SAW}} = (3.56 \pm 0.08) \text{ km/s}$, in good agreement with values given in the literature (Joshi *et al.*, 2006, Wolfe, 1998). It has been shown that the surface skimming longitudinal waves have a higher phase velocity if compared to SAW (Jhunjhunwala, 1977).

Two dimensional wave fields in phase contrast (as represented in figures 6.2-6.5) have been recorded with the aid of Coulomb coupling. The stored data array containing the images is treated as samples of a complex valued field $\psi(x, y, t)$, that may be superposed, at any selected instant of time, from planar wave components of the type

$$\Psi(s_x, s_y) \exp[2\pi i(s_x x + s_y y)] \quad (6.1)$$

For a wave propagating to the positive x axis the Fourier amplitudes shall differ from zero only in the case $s_x > 0$. Fourier spectra of the 2D quadrature detection measurements performed in the elastic half space, $x > 0$, (by assumption that (0, 0) is the position of the source) is also asymmetric. In the figure 6.5, positions of maxima are related to the reciprocals of respective wavelengths or spatial frequencies (s_x, s_y) . By sampling in space with step of $\Delta x = \Delta y = 0.01 \text{ mm}$, the Nyquist spatial frequency is 50 mm^{-1} .

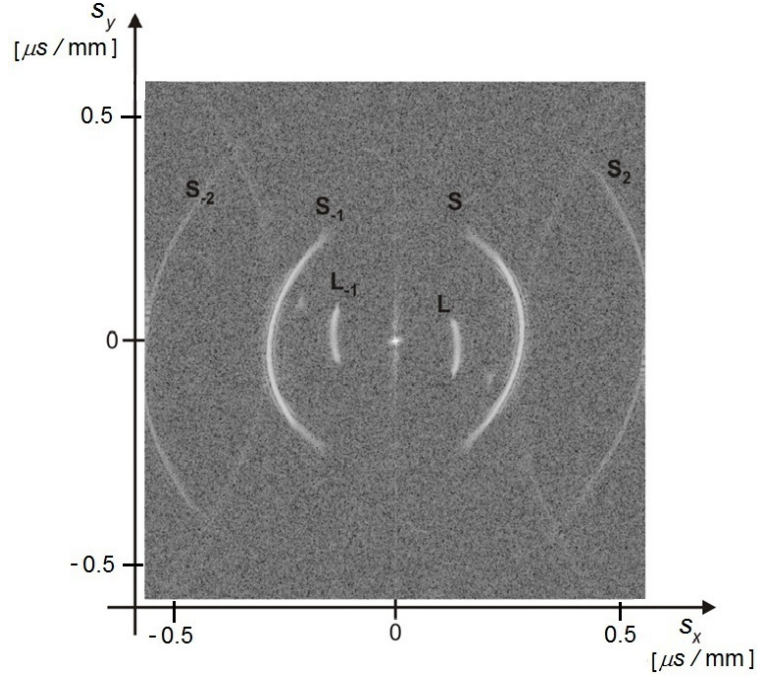


Figure 6.6: Two dimensional Fourier spectrum of registered complex valued field presented in negative logarithmic scale (maxima dark). L: spectrum of longitudinal wave, L_{-1} : weak 1st order spectrum of the longitudinal wave. S and S_2 respective orders of spectrum of the slower surface waves. S_{-1} and S_{-2} : relatively strong 1st order spectrum of the slower wave. Due to the aliasing effect some maxima for spatial frequencies $s_x > 0$ overlap with maxima for $s_x < 0$.

While sampling of the wave field fulfils that sampling criteria (we were collecting about four points per the shortest wave cycle), it is not fulfilled for higher harmonics. On one hand that causes the aliasing effect, but on the other hand positions of higher harmonics maxima could still bring additional information on the observed velocities. The respective wavelengths are calculated with the formula

$$\lambda = n / s_x \quad (6.2)$$

where $n = -1, 1, 2, 3$ is the order of the observed maximum. The respective velocities are calculated as $c = \lambda f$, where $f = 89.9 \text{ MHz}$ is the frequency applied in the experiment. Uncertainty of the result (visible in the figure 6.6 as the finite width of the maxima) is related to the finite length of applied excitation pulse. For equation 6.1 and 6.2 the group velocities of skimming longitudinal surface wave and surface acoustic waves are tabulated in table 6.1.

Table 6.1: Spatial frequencies, wavelength, and calculated velocities from the 2D Fourier spectrum of the wave field

Type of waves	$f_x \left(\frac{1}{mm} \right)$	$\lambda(\mu m)$	C (km/s)
L	12.1	82.6	7.42
L ₋₁	-12.3	81.2	7.3
S	25.6	39.1	3.51
S ₂	51.2	39.1	3.51
S ₋₁	-25.6	39.1	3.51
S ₋₂	76.7	39.1	3.51

6.3 Conclusions

The propagation of longitudinal polarized surface skimming bulk waves (SSLW) and SAWs was observed simultaneously by the local electric field probe technique. The scheme is independent of lithography procedures and overcomes the limitation of DT or IDT structures for excitation of surface wave. The developed technique allows for the variation of excitation frequency over wide range. The technique demonstrates the potential of holographic imaging to visualize acoustic wave fronts with Coulomb excitation and detection to study the electro-mechanical property of the crystal. The group velocities of SSLW and SAWs are determined as 7.45 ± 0.1 km/s and 3.56 ± 0.08 km/s, respectively. In addition, the individual acoustic wave modes and respective group velocities are validated from the two-dimensional Fourier transform of the acoustic wave fronts.

7 Scattering and Attenuation of Surface Acoustic Waves and Surface Skimming Longitudinal Polarized Bulk Waves Imaged by Coulomb Coupling

Summary

Coulomb coupling has been applied for vector contrast imaging of surface acoustic waves and surface skimming longitudinal polarized waves travelling on or in a 5 mm thick, Y-Z cut lithium niobate single crystal. The excitation and detection of acoustic waves was performed by Coulomb coupling. For excitation 20 oscillations at a frequency of 89.9 MHz were used. The scattering and attenuation of both, surface skimming and surface acoustic waves are studied by imaging in vector contrast. Objects employed for interaction with the waves are layers of absorptive and scattering materials. The interaction allows a clear differentiation of volume waves skimming the surface and guided waves traveling at the surface.

7.1 Introduction

The application of surface acoustic waves (SAW) in electronic devices such as modern telecommunications and filtering applications has stimulated considerable interest in the fundamental properties of ultrasonic waves (Hesjedal & Behme, 2001). The surface acoustic waves propagate oscillate in out-of-plane direction of crystal and their magnitude exponentially decays with depth. The increase in operating frequency has to compensate for the losses due to attenuation and scattering. The scattering of SAW waves is of particular interest when the wavelength of acoustic signal is less than 1/10 of the diameter size of the defects. For an effective excitation of the surface acoustic waves, the conventional comb like digital (DT) or interdigital transducers (IDT) positioned on piezoelectric crystals are typically used (White & Voltmer, 1965, Whatmore et al., 1982, H. Cerva & W. Graeff, 1984, Vines et al., 1995, Roshchupkin et al., 1994, Hamilton & Yethiraj, 1999, Hesjedal *et al.*, 1997). For DT and IDT transducers the frequency range and phase shifts are depending on the geometry. This leads in most cases to a complex temporal response function. The geometrical resonances of the conventionally used DT and IDT lead to limitations concerning the spatial and temporal resolution. An inherent problem of such comb like structure is that the electrodes also act as scattering objects, similar as the terminations of the electrodes (Hesjedal, 2010). In conventional IDT, the electrodes are manufactured from deposition of

gold and silver and act also as scatters. The scattering and attenuation by deposits is studied here with high spatial resolution, to provide detailed monitoring suitable to characterize the performance of SAW devices.

The attenuation and scattering of SAWs is a sensitive means of characterization of the surface of a crystal (Smith & Wickramasinghe, 1982). Variations in material properties such as surface and bulk defects lead to wave scattering, magnitude dependent conversion of energy from fundamental to harmonic frequencies in a nonlinear medium, or losses due to viscous contaminants on the surface (Hesjedal, 2010).

The main objective of this study is to introduce a new technique for visualization of SAW attenuation and scattering caused by surface deposits on a piezoelectric crystal (LiNbO_3 , 5 mm thick, both sides optically polished, YZ cut) by local electric field probes via scanned Coulomb excitation and detection. The developed technique of excitation and detection of ultrasonic waves with the help of local electrical field probes allows to observe the effect of scattering in the images and to segregate signals resulting from scattering with respect to the undisturbed propagation of the excited acoustic waves (Habib *et al.*, 2010). Furthermore excited parasitic modes, not desired for SAW filters, can be detected at the scanned surface.

7.2 Experimental Setup

A similar experimental set-up for the Coulomb excitation and detection for surface acoustic waves has been described in the experimental section 4.4. To observe the scattering on surface deposits a droplet of conducting silver paint was deposited on the surface of the LiNbO_3 crystal. In figure 7.1 shows the confocal laser scanning microscope image of the deposited silver paint on the surface of the LiNbO_3 crystal. The length of the conducting silver paint deposit was about 350 μm with a somewhat irregular shape.

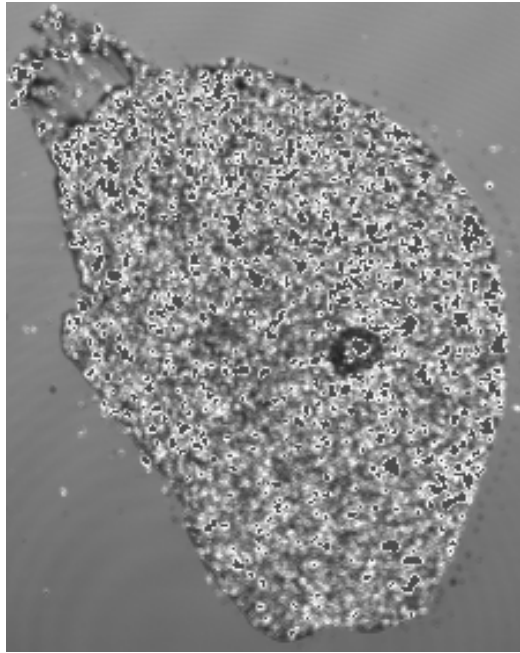


Figure 7.1: Confocal laser scanning microscopy image of the deposited silver paint on the surface of the LiNbO_3 crystal

In figure 7.2 the excitation and detection scheme is illustrated. The probes employed for excitation and detection were both fabricated from a $50\ \mu\text{m}$ gold wire, wrapped around a bronze wire (figure 7.2). Two $200\ \mu\text{m}$ bronze wires were crossed in order to form a triangular lever holding the tip and providing by spring action a suitable pressure to the contact area. The exciting electrode is scanned by a stepper motor driven 2D translation stage line by line across the surface of the crystal. The receiving electrode is placed at a fixed position on the same surface. It connects to an amplifier mounted in a metallic box acting as a Faraday cage. The minimum distance between the exciting and receiving probes is limited by the Faraday cage to about $1\ \text{mm}$. The scan area for the images displayed here has been set to $4 \times 4\ \text{mm}^2$.

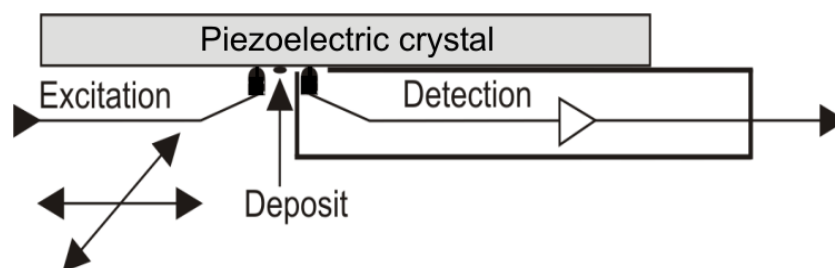


Figure 7.2: Schematic diagram for the piezoelectric excitation and detection of acoustic waves by Coulomb coupling

A burst with a carrier frequency of $89.9\ \text{MHz}$ with a length of $220\ \text{ns}$ is cut from a continuous wave generated by an oscillator with the help of an electronic switch controlled

by a pulse generator. Following amplification it is delivered to the scanned Coulomb probe for excitation. The electric field generated and picked up by the exciting and receiving Coulomb coupling probes together with the direct and inverse piezoelectric effect convert the electrical signals to mechanical oscillations and vice-versa. The multiplied signals are low-pass filtered in order to remove the high-frequency components (double the frequency of the oscillator) generated by multiplication. After filtering the signals were digitized by a two channel 8 bit, 89.9 MHz sampling rate transient recorder (Grill et al., 1996, Twerdowski, 2007).

7.3 Results and Discussions

The evolution of surface skimming longitudinal and surface acoustic waves in the LiNbO_3 single crystal presented in the time sequential images of magnitude in figure 7.3

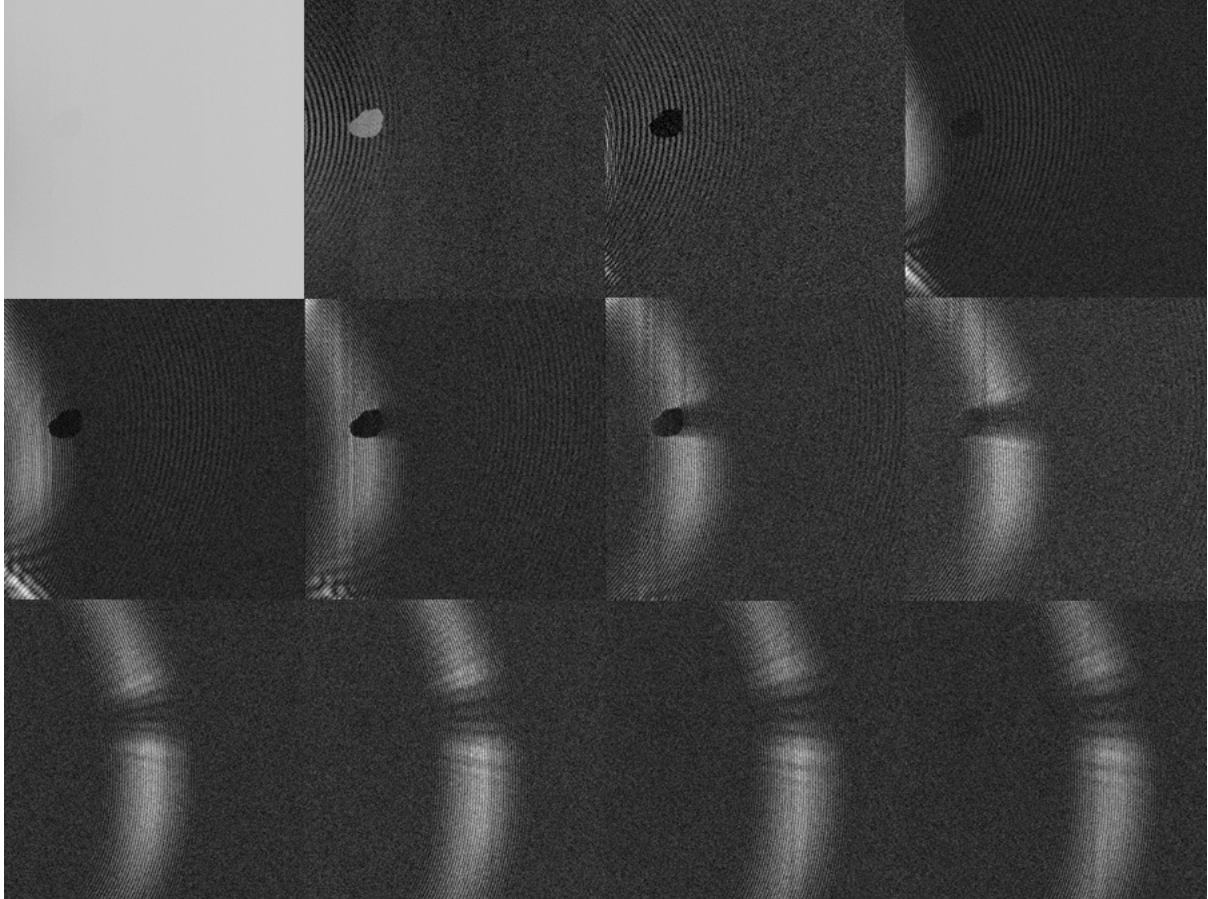


Figure 7.3: Transient evolution of magnitude of the propagating surface skimming longitudinal and acoustic waves in a LiNbO_3 single crystal. The first response observed (1st image from left in top row) is dominated by electrical crosstalk. Width of the each imaged area: 4.0 mm

Surface skimming longitudinal polarized bulk waves (SSLW) and surface acoustic waves (SAW) were both generated and detected at one of the surfaces of the disc shaped LiNbO_3 crystal. In figure 7.4 images obtained by scanning, timed for SSLWs passing the deposit, are displayed. The conductive silver paint deposit is visible in both types of contrast as an object with uniform brightness.

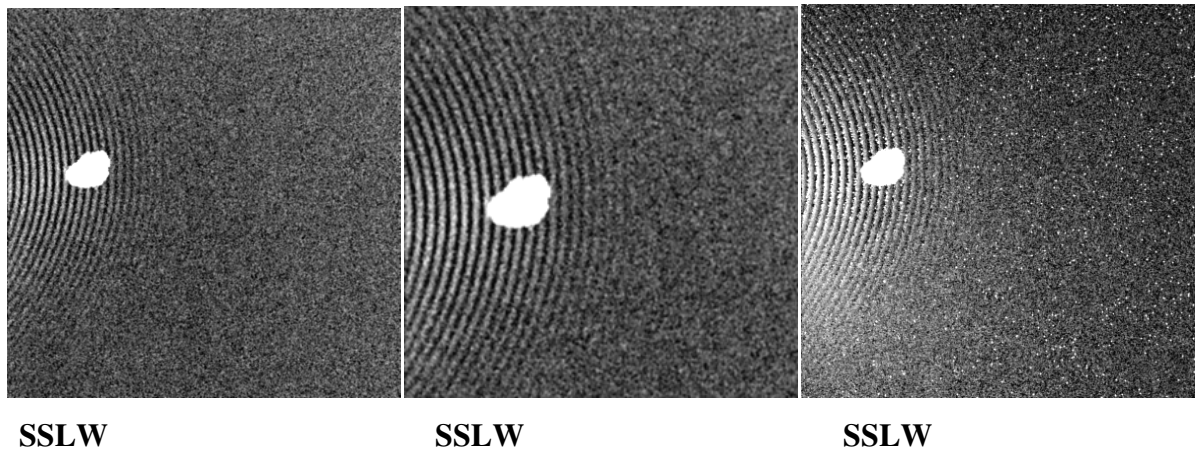


Figure 7.4: Scanned image timed to observe only travelling SSLWs. Left: Representation in amplitude contrast. The brightness is proportional to the amplitude with medium grey relating to zero amplitude. Center: Magnified view of left image. Right: Image in phase contrast with the full grey scale representing 2π on a linear scale. Width of the imaged area: 4.0 mm.

The group velocity of the longitudinal polarized acoustic bulk wave is about two times higher than that of the SAWs (Makkonen et al., 2003). The longitudinal polarized wave skimmed along the surface and their magnitude drops according to geometric effects within the volume during propagation. The SSLWs propagate beneath the sample surface and do not show any pronounced perturbation on its propagation due to the presence of the obstacle at the surface as depicted from figure 7.4. However, as displayed in figure 7.5, the SAWs, with most of the power travelling in the vicinity of the sample surface, exhibit a strong interaction with the conductive silver paint deposit. Different to skimming volume waves, surface acoustic waves are very sensitive to any perturbation of the free surface.

The incident SAW is attenuated at the surface covered by the thin conductive silver paint film. The size of the deposit is much bigger than the wavelength of the monitored acoustic waves. For SAWs extremely strong scattering is observed (figure 7.5). The viscous properties of the binding component of the paint induce attenuation of acoustic waves, which are additionally strongly scattered by the silver flakes exhibiting a large acoustic mismatch to the binding component. This way the deposit from conductive silver paint acts as a strongly scattering and attenuating media for SAWs at the selected frequency.

From figure 7.5 can be depicted that the SAWs are dominantly absorbed by the deposited conductive silver paint. The shadowed wave field is partially filled with waves resulting from diffraction by the absorptive deposit, as studied in rich detail historically for

optics and last not least waves on water. In figures 7.4 and 7.5, the images in amplitude contrast show in the entire area of the deposit a constant magnitude since the individual localized signal contributions are cancelled due to integration over an area large compared to the wavelength, caused by the electrical conductivity of the deposit.

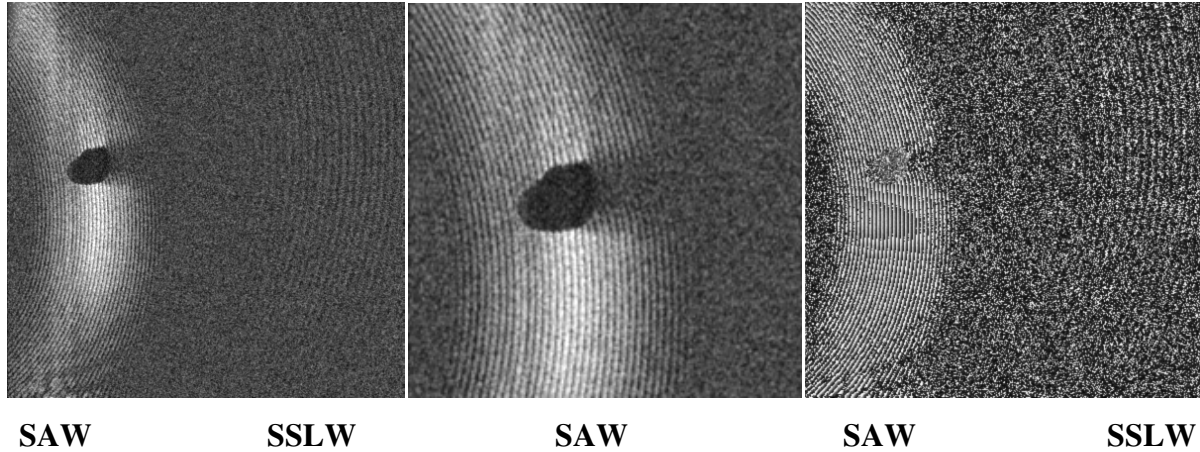


Figure 7.5: Scanned image timed to observe travelling SAWs and SSLWs. Left: Representation in amplitude contrast. Center: Magnified view of the region around the deposit. Right: representation in phase contrast. The contrast in the image in magnitude contrast varies slightly in horizontal direction in the left part due to some deterioration caused most likely by deposits on the tip of the scanning electrode. Width of the imaged area: 4.0 mm; contrast as in figure 7.5.

Similarly the image in phase contrast is influenced by the extended conductive surface deposit. As to be expected from absorbing respectively strong scattering obstacles and resulting diffraction, curved waves are observed behind the obstacle with a center of the curvature of the individual scattered wave-fields positioned at the location of the scattering at the obstacle. In the gathered images mainly two types of waves were formed; surface acoustic waves (SAW), which were strongly attenuated and scattered by the deposit on the surface of the crystal, and surface skimming longitudinal polarized bulk waves (SSLW), which exhibit only a negligible effect concerning scattering or absorption by the deposit.

In order to determine the velocities of the traveling waves the phase is tracked in the images along the direction of propagation of SAW and SSLW. Timing is derived from the known frequency. The velocity, determined by the product of frequency and observed wavelength, relates to the phase velocity projected on the surface concerning bulk waves. The velocity of SAWs as obtained from the measurement is $V_{SAW} = (3.6 \pm 0.2)$ km/s, in

reasonable agreement with values given in the literature (Joshi et al., 2006, Wolfe, 1998). Similarly, the velocity of surface skimming longitudinal waves is determined as $V_{SSLW} = (7.0 \pm 0.4)$ km/s.

7.4 Conclusion

Visualization of the attenuation of SAWs and scattering by a surface deposit of conductive silver paint on a LiNbO_3 crystal with the aid of a scanning local electric field probe via Coulomb excitation and detection has been demonstrated. The developed technique allows for the variation of the excitation frequency and type of signal over a wide range, since geometrical resonances are absent. The presented results demonstrate the potential of time gated holographic imaging to visualize the propagation and interaction of acoustic waves by attenuation and scattering. By the developed Coulomb excitation and detection scheme the electro-mechanical and acoustical properties of the material used for generation and propagation of SAWs and volume waves can be studied in detail. The initial work presented here demonstrates the rather strong and often undesired effects of SSLWs and the different behavior of SSLWs and SAWs concerning the interaction with deposits on surfaces. The obtained images quantify the influence of SSLWs, an often undesired parasitic byproduct in filter applications, and their interaction with deposits.

8 Conclusion and Outlook

Conclusions

The elastic property and ultrasonic characterization of the piezo-electric material is evaluated using scanning acoustic microscopy and Coulomb coupling technique. The highly c-axis oriented polycrystalline Aluminum nitride is grown on silicon substrate using rf-magnetron sputtering technique. The morphology, crystalline structure, and crystalline orientation of the AlN films significantly affect the acoustic velocities. The surface roughness, thickness and orientation of the thin film were determined using atomic force microscopy and scanning electron microscopy, respectively. The surface roughness and topological aberration significantly affects the propagation direction of ultrasonic waves and cause scattering and attenuation. The root mean square roughness R_a of the thin film was 6.5 nm which is three orders smaller than thickness of film and the wavelength of longitudinal wave mode ensuring low loss of energy during propagation. EDX was conducted to determine the composition of the AlN thin film. The localized elastic property of the thin film was determined using nanoindentation technique. The nanoindentation is not an appropriate tool for thin film characterization due to influence of substrate. Several other surface probing techniques such as AFAM are not suitable of thin film characterization with high elastic properties. Therefore, scanning acoustic microscopy at 1 GHz was performed for ultrasonic characterization of the thin film. The variation in reflectivity of the echo signal of ultrasonic waves with defocusing distance of the lens was used for evaluating the longitudinal and surface acoustic wave velocities. SAM has a potential for determining the delaminating due to internal stress of the film deposited in acoustic impedance mismatching layers (AlN-Silicon) unlike AFAM and nanoindentation. The mechanical property of the AlN was determined by SAM and Young's modulus of elasticity was 304 ± 3 GPa.

In ultrasonic nondestructive testing and structural health monitoring application the piezoelectric transducers are widely used for excitation and detection of Lamb waves for damage detection. The mechanical characterization of PZT is utmost needed for compatibility of acoustic impedance of sensor to that of the material under investigation. The ultrasonic characterization of PZT is conducted using SAM at 100 MHz excitation frequency. The scanning electron microscope (SEM) was performed to study the surface morphology, grain structure and grain boundaries. Relatively low frequency (100 MHz) was used for

determination of global bulk properties of PZT, as it is far more important than the localized bulk property. The ultrasonic characterization of PZT includes determination of velocities of leaky surface acoustic wave, surface skimming longitudinal acoustic wave and transversal wave. Similar to GHz microscopy, acoustic material signature (AMS) curve are used to determine bulk wave velocities. The AMS curve exhibits the interference of the waves due to defocusing. The surface acoustic waves were difficult to identify in PZT due to higher relative roughness compared to the grain size. The qualitative knowledge derived through SEM and quantitative information from SAM coupled together provides the propagating and scattering behavior of the acoustic waves in PZT. The longitudinal wave velocity and elastic property of the PZT was determined as 5359 ± 190 m/s and 183 ± 12 GPa.

Scanning acoustic microscopy is remarkable technique for determining elastic property of bulk material as well as thin films. However, determination of electro-mechanical material constant in piezo crystal is still challenging through SAM. In SAM, the ultrasonic waves are weakly coupled with piezoelectric property of material and therefore only uncoupled mechanical properties are determined. Therefore, a new technique is developed for excitation and detection of SAW and bulk waves in piezoelectric crystals using Coulomb coupling principal. The technique explores the possibility of exciting the coulomb field in the piezo material, coupling its piezoelectric property to mechanical property within the material. A potential application is the determination of elastic and piezoelectric constants, including elastic constants with rather small values associated with a slight deviation from a higher crystal symmetry class.

PZT sintered plates are used as transducers for the excitation of Lamb waves in applications involving NDT and SHM by ultrasound, have been mechanically characterize by scanned Coulomb coupling. Coulomb coupling technique has been performed for generation and detection of ultrasonic waves in PZT. The time sequential monitoring of the acoustic waves excited and detected by a short pulse reveals that the main contributions are emitted ring systems. The grain size of piezo-sintered ceramic was 4.6 micron has been measured from SEM images. The large diameter grains of PZT ceramics causes wave scattering. The acoustic wave propagation in PZT, the first ring observed close to the excitation travels with a velocity comparable to that of bulk waves determined from the material parameters. On the other hand the second ring close to the velocity of S₀ Lamb waves in the long wavelength limit. The velocities as determined by a least square fit are 4610 ± 230 m/s for the first and 3865 ± 95 m/s for the second ring. The developed and applied method can be used as a basis

for modeling by the experimentally gained point response observed by scanned imaging with Coulomb coupling.

Surface acoustic waves in piezoelectric materials are propagated on the surface of materials, and are well known tool surface characterization of in interface science. The wavelengths of SAW are localized on the surface and exponentially decay in the depth of the material. The presented scheme is independent from complicated lithography procedure for fabrication of the IDT on the surface of the crystal and allow us to visualize the time dependent SAWs propagation on a piezoelectric materials. The imaging of the acoustic waves is performed with switched sinusoidal excitation and quadrature detection, from which the magnitude and phase are derived. In the magnitude images highly sensitive information on the piezoelectrically stiffened elastic tensor is obtained for directions, in which an interference resulting from a superposition of contributions from group velocities with different absolute values but identical directions is observed. For the phase contrast image, highly sensitive information is obtained in any direction and here favorably in the absence of interference. The available vector contrast with separate images for magnitude and phase is well suited to quantitatively determine the acoustic waves velocities in piezoelectric materials. The wavelengths of surface skimming longitudinal and surface acoustic waves are both determined from the observed phase rotation. The phase velocities for propagation along the Z-axis are $V_{SSLW}=(7.45\pm 0.1)$ km/s and $V_{SAW}=(3.56\pm 0.08)$ km/s, respectively.

Scattering and attenuation of the SAWs on piezoelectric crystal are of great fundamental importance due to their application as delay line and SAW filters. The investigation was carried out to study the scattering and attenuation phenomena of surface acoustic wave. The scattering of SAW is of particular interest when the wavelength of the ultrasonic waves is much smaller than the size of the defect. In order to address this issue the local electrical field probe technique has been employed for generating and detection of SAWs waves and imaged with sub-micron resolution. The relatively wide-gate width (220 ns) was selected for excitation to visualize the selective frequency response and its interaction with arbitrary defect size. A conducting silver paint was deposited on the surface of the LiNbO_3 single crystal which acted as both acoustic scatterer and attenuator. The size of the scatterer was 350 microns and the SAW wavelength was 39.6 μm . The scatterers were almost 100 times bigger than wavelength and act as a bulk scatterers. Highly resolved spatial and temporal imaging was performed to study the interaction of surface skimming longitudinal and surface acoustic waves. The deposit does not show any perturbation as the

surface skimming longitudinal wave as they skimmed beneath the surface and does not show strong interaction with surface waves or surface defect. On the other hand, the silver deposit causes the attenuation of the SAWs which leads the deterioration of the propagating wave in the forward direction. The silver deposit alters the direction of propagation of SAW and scatters the wave. The amplitude of SAW decreases after interaction with silver paint due to absorption of energy.

Outlook:

Further developments of this project are the followings:

- ❖ Uniaxially c-axis oriented epitaxial films of having a optimize thickness on Si and as an inter-layer nanocrystalline diamond
- ❖ Designing and fabrication of IDT using focused ion beam (FIB)
- ❖ Excitation and detection of SAW's to detect surface and subsurface defects. Inter-digital transducer of frequency 600 MHz will be fabricated on the AlN film using focused ion beam (FIB). An acoustic wave field will be generated on the surface (8.1) of an AlN film by a piezoelectric transducer (IDT). In the near field of the IDT, an *in-situ* crack will be initiated using piezo stack (PI). The piezo-stack will operate at 120 V to produce nominal displacement of 10 μm normal to the plane of propagation of excitation of SAW.

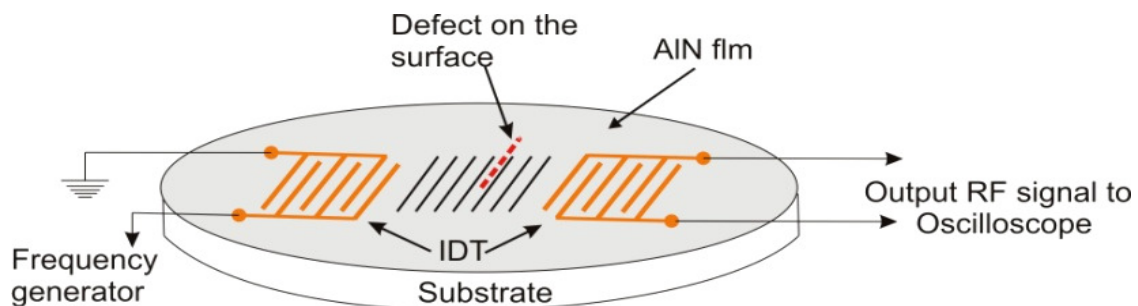


Figure 8.1: Experimental set up for the defect detection on the surface of the AlN films using surface acoustic waves

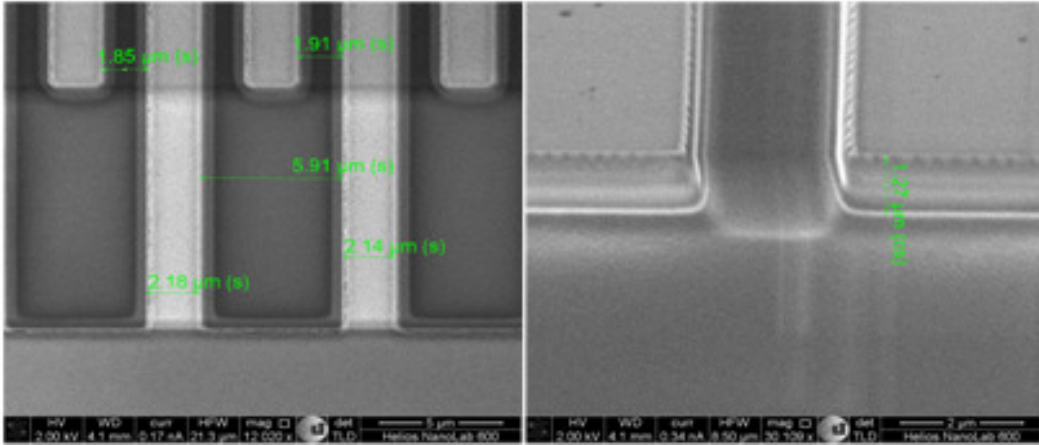


Figure 8.2: Top view (left) and side view (right) under 52° tilt of a fabricated IDT structure using the Ga⁺ focused ion beam (FIB) etching of a 2 μm thick AlN film

Modeling and Simulation: The transient finite element modeling and simulation would be conducted to simulate delta pulse on AlN films using for IDT. The time harmonic excitation would enable for visualization of acoustic wave front on surface and bulk of the crystal. The bulk wave and Lamb wave dispersion behavior can be studied by Christoffel's equation and commercial software disperse. The material model can also be derived from the experimental results conducted using IDT and SAM. The finite element modeling would provide a comprehensive knowledge about the wave propagation, dispersion, attenuation and scattering in piezo-materials.

Acknowledgements

Praise be to God; Most Gracious, Most Merciful.

First of all, my utmost gratitude goes to my wonderful supervisor, Prof. Dr. Ullrich Pietsch for giving me the opportunity to join his Festkörperphysik group. Rather than that, I would like to thank for his constant support and unflinching encouragement during my whole dissertation period. Thank you so much for your advices and motivation. I would like to specially thank Prof. Dr. Wolfgang Grill for his overall support during the experiments and allowing me to use his lab. I would like also to thank you to teach and shaped my view in acoustics. My high regard to Dr. Amit Shelke, who patiently answered my all questions, guided me and helped me through numerous discussions we had during the experiments. Your enthusiasm has deeply inspired me.

I would like to acknowledge Dr. M. Pluta for the valuable discussions on the problem and his support throughout my stay in Leipzig.

Special thanks to Prof. Dr. T. Kundu for the fruitful discussions and collaboration.

I would like to thank PD. Dr. Reinhold Wannemacher for your encouragements for last several years.

I would like to thank to the following professors who have given me an opportunity to use their laboratories and their scientific coworker who have helped me during the various purposes.

- ❖ Prof. Dr.-Ing. Peter Haring Bolívar and Dr.-Ing. Heiko Schäfer Eberwein for IDT fabrication.
- ❖ Prof. Dr. Xin Jiang and Michael Vogel for various kinds of thin films, SEM, AFM, and nanoindentation measurements.

Acknowledgements

Not to forget to my family, millions of lovely thanks to them for their perpetual support and encouragement.

I would like to thank all the former and present members of Solid State Physics group at University of Siegen for the friendly environment in the group.

And I would like to thank my beloved wife Shanta, for her love and patience.

Bibliography

Curriculum vitae

Bibliography

Bibliography

Achenbach, J. D. (2004) Ultrasonic characterization of thin film material constants and defects. *Key Engineering Materials*, 270, 8-13.

Als-Nielsen, J. & McMorrow, D. (2001) *Elements of modern X-ray physics*, Wiley, West Sussex.

Arnold, W., Betz, B. & Hoffmann, B. (1985) Efficient generation of surface acoustic waves by thermoelasticity. *Appl. Phys. Lett.*, 47, 672-674.

Auld, B. A. (1993) *Acoustic fields and waves in solids*, John Wiley, New York.

Bamber, M., Cooke, K., Mann, A. & Derby, B. (2001) Accurate determination of Young's modulus and Poisson's ratio of thin films by a combination of acoustic microscopy and nanoindentation. *Thin Solid Films*, 398, 299-305.

Benetti, M., Cannata, D., Di Pictrantonio, F. & Verona, E. (2005) Growth of AlN piezoelectric film on diamond for high-frequency surface acoustic wave devices. *IEEE Trans. Ultrason. Ferroelectr. Freq. Control.*, 52, 1806-1811.

Bergman, L. & Nemanich, R. J. (1996) Raman spectroscopy for characterization of hard, wide-bandgap semiconductors: Diamond, GaN, GaAlN, AlN, BN. *Annu. Rev. Mater. Sci.*, 26, 551-579.

Bjurström, J., Katardjiev, I. & Yantchev, V. (2005) Lateral-field-excited thin-film Lamb wave resonator. *Appl. Phys. Lett.*, 86, 154103.

Brand, S., Raum, K., Czuratiss, P. & Hoffrogge, P. (2007) 9D-6 Signal Analysis in Scanning Acoustic Microscopy for Non-Destructive Assessment of Connective Defects in Flip-Chip BGA Devices. In: *Ultrasonics Symposium*. IEEE, New York, NY

Briggs, A. (1992) Acoustic microscopy-a summary. *Reports on Progress in Physics*, 55, 851.

Briggs, A. & Kolosov, O. (2009) *Acoustic microscopy*, Oxford University Press, USA.

Bibliography

Capelle, B., Epelboin, Y., Soyer, A. & Détaint, J. (2012) Observation of surface acoustic waves using synchrotron radiation X-ray topography. *IEEE*.

Carlotti, G., Gubbiotti, G., Hickernell, F., Liaw, H. & Socino, G. (1997) Comparative study of the elastic properties of polycrystalline aluminum nitride films on silicon by Brillouin light scattering. *Thin Solid Films*, 310, 34-38.

Carlotti, G., Hickernell, F., Liaw, H., Palmieri, L., Socino, G. & Verona, E. (1995) The elastic constants of sputtered aluminum nitride films. *IEEE*.

Chen, H. D., Udayakumar, K. R., Gaskey, C. J. & Cross, L. E. (1995) Electrical properties maxima in thin films of the lead zirconate–lead titanate solid solution system. *Appl. Phys. Lett.*, 67, 3411-3413.

Corker, D., Glazer, A., Whatmore, R., Stallard, A. & Fauth, F. (1998) A neutron diffraction investigation into the rhombohedral phases of the perovskite series. *J. Phys.: Condens. Matter*, 10, 6251-6269.

Drescher-Krasicka, E. & Willis, J. R. (1996) Mapping stress with ultrasound.

Encyclopedia, T. W. B. o. (1999) The speed of sound in various mediums, Distilled Water at 77 °F (25 °C), 1496 m/s, 4908 ft/s" 1496 m/s. Chicago: World Book.

Every, A. G. & Deschamps, M. (2003) Principal surface wave velocities in the point focus acoustic materials signature $V(z)$ of an anisotropic solid. *Ultrasonics*, 41, 581-591.

Farnell, G. (1970) Properties of elastic surface waves. *Physical acoustics*, 6, 109-166.

Foster, F. S., Ryan, L. K. & Turnbull, D. H. (1991) Characterization of lead zirconate titanate ceramics for use in miniature high-frequency (20-80 MHz) transducers. *IEEE Trans. Ultrason. Ferroelectr. Freq. Control.*, 38, 446-453.

Friend, J., Jamieson, E., Pennell, M. & Huebner, W. (2001) Ultrasonic characterization of poling in lead zirconate titanate ceramics. *Appl. Phys. Lett.*, 79, 2794.

Fujii, T., Watanabe, S., Suzuki, M. & Fujiu, T. (1995) Application of lead zirconate titanate thin film displacement sensors for the atomic force microscope. *J. Vac. Sci. Technol. B*, 13, 1119-1122.

Bibliography

G. H. Haertling (1999) Ferroelectric ceramics: history and technology. *J. Am. Ceram. Soc.*, 82, 797-818.

Gebhardt, S., Seffner, L., Schlenkrich, F. & Schönecker, A. (2007) PZT thick films for sensor and actuator applications. *J. Eur. Ceram. Soc.*, 27, 4177-4180.

Gerlich, D., Dole, S. L. & Slack, G. A. (1986) Elastic properties of aluminum nitride. *J. Phys. Chem. Solids*, 47, 437-441.

Ghosh, T., Maslov, K. & Kundu, T. (1997) A new method for measuring surface acoustic wave speeds by acoustic microscopes and its application in characterizing laterally inhomogeneous materials. *Ultrasonics*, 35, 357-366.

Gilmore, R. (1996) Industrial ultrasonic imaging and microscopy. *Journal of Physics D: Applied Physics*, 29, 1389.

Glazer, A., Thomas, P., Baba-Kishi, K., Pang, G. & Tai, C. (2004) Influence of short-range and long-range order on the evolution of the morphotropic phase boundary in $\text{Pb}(\text{Zr}_{1-x}\text{Ti}_x)\text{O}_3$. *Phys. Rev. B*, 70, 184123-184129.

Glegg, S. (1980) *Ultrasonics* (Wykeham Science Series No. 55) 1980, by AP Cracknell. London: Wykeham Publications (London) Ltd.(New York: Crane Russak & Company, Inc.) 200 pp. *J. Sound Vibration*, 72, 565-565.

Grill, W., Hillmann, K., Würz, K. U. & Wesner, J. (1996) Scanning ultrasonic microscopy with phase contrast. *Advances in acoustic microscopy*, 2, 167-218.

Griswold, E. M., Weaver, L., Sayer, M. & Calder, I. D. (1995) Phase transformations in rapid thermal processed lead zirconate titanate. *J. Mater. Res.*, 10, 3149-3159.

H. Cerva & W. Graeff (1984) Contrast investigations of surface acoustic waves by stroboscopic topography. I. Orientation contrast. *Phys. Status Solidi (a)*, 82, 35-45.

H. Fu & R. E. Cohen (1990) Polarization rotation mechanism for ultrahigh electromechanical response in single-crystal piezoelectrics. *Nature*, 403, 281-283.

Habib, A., Amjad, U., Pluta, M., Pietsch, U. & Grill, W. (2010) Surface acoustic wave generation and detection by Coulomb excitation. In: *SPIE*. San Diego, USA.

Bibliography

Habib, A., Shelke, A., M. Pluta, T. Kundu, U. Pietsch & Grill., W. (2012a) Imaging of acoustic waves in piezoelectric ceramics by Coulomb coupling. *Jpn. J. Appl. Phys.*, 51.

Habib, A., Shelke, A., Pietsch, U. & Kundu, T. (2012b) Mechanical characterization of sintered piezo-electric ceramic material using scanning acoustic microscope. *Ultrasonics*.

Habib, A., Shelke, A., Vogel, V., Brand, S., Jiang, X., Kundu, T. & Pietsch, U. (2012c) Ultrasonic characterization of AlN film using scanning acoustic microscopy.

Habib, A., Twerdowski, E., v. Buttlar, M., Pluta, M., Schmachtl, M., Wannemacher, R. & Grill, W. (2006) Acoustic holography of piezoelectric materials by Coulomb excitation. In: *SPIE*. San Diego, USA.

Haertling, G. H. (1999) Ferroelectric ceramics: history and technology. *J. Am. Ceram. Soc.*, 82, 797-818.

Hamilton, W. A. & Yethiraj, M. (1999) Effects of traveling surface acoustic waves on neutron Bragg scattering from perfect crystals. *Phys. Rev. B*, 59, 3388.

Hesjedal, T. (2010) Surface acoustic wave-assisted scanning probe microscopy—a summary. *Rep. Prog. Phys.*, 73, 016102.

Hesjedal, T. & Behme, G. (2001) High-resolution imaging of surface acoustic wave scattering. *Appl. Phys. Lett.*, 78, 1948.

Hesjedal, T., Chilla, E. & Fröhlich, H. J. (1997) Scanning acoustic force microscope investigations of surface acoustic waves. *Surface and interface analysis*, 25, 569-572.

Hesjedal, T., Chilla, E. & Fröhlich, H. J. (1999) Scanning Acoustic Force Microscope Investigations of Surface Acoustic Waves. *Surf. Interface Anal.*, 25, 569-572.

Hildebrand, J. A. & Lam, L. K. (1983) Directional acoustic microscopy for observation of elastic anisotropy. *Appl. Phys. Lett.*, 42, 413-415.

Hirsekorn, S. & Pangraz, S. (1994) Materials characterization with the acoustic microscope. *Applied physics letters*, 64, 1632-1634.

Bibliography

- Huang, C., Wang, S., Peng, C., Shieh, J., Chang, C. & Lin, T. (2006) Microstructures and dielectric properties of PZT thick films prepared by aerosol plasma deposition with microwave annealing. *Materials Science and Engineering: B*, 133, 181-185.
- Jacobsen, E. H. (1960) Sources of sound in piezoelectric crystals. *J. Acoust. Soc. Am.*, 32, 949.
- Jaffe, B., Cook, W. R. & Jaffe, H. (1971) *Piezoelectric ceramics*, Academic Press London.
- Jhunjhunwala, A. (1977) Theory of surface acoustic waves. University of Maine.
- Joshi, S., Zaitsev, B., Kuznetsova, I., Teplykh, A. & Pasachhe, A. (2006) Characteristics of fundamental acoustic wave modes in thin piezoelectric plates. *Ultrasonics*, 44, 787-791.
- Kino, G. S. (1987) *Acoustic waves: devices, imaging, and analog signal processing*, Prentice-Hall Englewood Cliffs, NJ.
- Kopycinska, M., Ziebert, C., Schmitt, H., Rabe, U., Hirsekorn, S. & Arnold, W. (2003) Nanoscale imaging of elastic and piezoelectric properties of nanocrystalline lead calcium titanate. *Surface science*, 532, 450-455.
- Kundu, T. (1992) A complete acoustic microscopical analysis of multilayered specimens. *J. Appl. Mech.*, 59, 54-60.
- Kundu, T. & Jørgensen, C. S. (2002) Measuring elastic properties of bones and silicon from V(z) curve generated by multiply reflected signals. *Ultrasonics*, 39, 515-524.
- Kundu, T., Mal, A. K. & Weglein, R. D. (1985) Calculation of the acoustic material signature of a layered solid. *J. Acoust. Soc. Am.*, 77, 353-361.
- Kushibiki, J. & Chubachi, N. (1985) Material characterization by line-focus-beam acoustic microscope. *IEEE Trans.Sonics Ultrason.*, 32, 189-212.
- Kushibiki, J., Chubachi, N. & Tejima, E. (1989) Quantitative evaluation of materials by directional acoustic microscope. In: *Ultrasonics International*.

Bibliography

Kushibiki, J., Maehara, H. & Chubachi, N. (1982) Measurements of acoustic properties for thin films. *J. Appl. Phys.*, 53, 5509-5513.

Kushibiki, J., Matsumoto, Y. & Chubachi, N. (1983) Attenuation measurements of leaky waves by the acoustic line-focus beam. *Electron. Lett.*, 19, 512-514.

Kushibiki, J., Ohkubo, A. & Chubachi, N. (1981) Anisotropy detection in sapphire by acoustic microscope using line-focus beam. *Electron. Lett.*, 17, 534-536.

Lemons, R. & Quate, C. (1974) Acoustic microscope—scanning version. *Appl. Phys. Lett.*, 24, 163-165.

Liaw, H. M. & Hickernell, F. S. (1995) The characterization of sputtered polycrystalline aluminum nitride on silicon by surface acoustic wave measurements. *IEEE. T. Ultrason. Ferr.*, 42, 404-409.

Lin, C. M., Lien, W. C., Felmetger, V. V., Hopcroft, M. A., Senesky, D. G. & Pisano, A. P. (2010) AlN thin films grown on epitaxial 3C-SiC (100) for piezoelectric resonant devices. *Appl. Phys. Lett.*, 97, 141907-141907-141903.

Liu, J., Lakin, K. & Wang, K. (1975) Growth morphology and surface-acoustic-wave measurements of AlN films on sapphire. *J. Appl. Phys.*, 46, 3703-3706.

Low, T. S. & Guo, W. (1995) Modeling of a three-layer piezoelectric bimorph beam with hysteresis. *J. Microelectromech. Syst.*, 4, 230-237.

M. Alguero, A. J. Bushby, M. J. Reece & A. Seifert (2002) Anelastic deformation of Pb (Zr, Ti) O thin films by non-180° ferroelectric domain wall movements during nanoindentation. *Appl. Phys. Lett.*, 81, 421.

Maeder, T., Muralt, P., Sagalowicz, L., Reaney, I., Kohli, M., Kholkin, A. & Setter, N. (1996) Pb (Zr, Ti) O thin films on zirconium membranes for micromechanical applications. *Appl. Phys. Lett.*, 68, 776-778.

Makkonen, T., Plessky, V. P., Steichen, W. & Salomaa, M. M. (2003) Surface-acoustic-wave devices for the 2.5-5 GHz frequency range based on longitudinal leaky waves. *Appl. Phys. Lett.*, 82, 3351.

Bibliography

Medcyclopaedia http://www.medcyclopaedia.com/library/topics/volume_i/q/quadrature_detection.aspx. In: *Quadrature detection*.

Nishino, H., Tsukahara, Y., Nagata, Y., Koda, T. & Yamanaka, K. (1993) Excitation of high frequency surface acoustic waves by phase velocity scanning of a laser interference fringe. *Appl. Phys. Lett.*, 62, 2036-2038.

Okano, H., Tanaka, N., Takahashi, Y., Tanaka, T., Shibata, K. & Nakano, S. (1994) Preparation of aluminum nitride thin films by reactive sputtering and their applications to GHz-band surface acoustic wave devices. *Applied physics letters*, 64, 166-168.

Olivares, J., González-Castilla, S., Clement, M., Sanz-Hervás, A., Vergara, L., Sangrador, J. & Iborra, E. (2007) Combined assessment of piezoelectric AlN films using X-ray diffraction, infrared absorption and atomic force microscopy. *Diamond Relat. Mater.*, 16, 1421-1424.

Oliver, W. C. & Pharr, G. M. (1992) An improved technique for determining hardness and elastic modulus using load and displacement sensing indentation experiments. *J. Mater. Res.*, 7, 1564-1583.

Pearce, L. G., Gunshor, R. L. & Pierret, R. F. (1981) Aluminum nitride on silicon surface acoustic wave devices. *Appl. Phys. Lett.*, 39, 878-879.

Pensala, T., Makkonen, T., Vartiainen, J., Knuutila, J., Kaitila, J., Holmgren, O. & Salomaa, M. M. (2002) Laser interferometric measurement of Lamb wave dispersion and extraction of material parameters in FBARs. IEEE.

Penza, M., De Riccardis, M., Mirengi, L., Tagliente, M. & Verona, E. (1995) Low temperature growth of rf reactively planar magnetron-sputtered AlN films. *Thin Solid Films*, 259, 154-162.

PI http://piceramic.com/datasheet/Piezo_Material_Datasheet_Coefficients_Temperature_Measurements.pdf.

PI http://www.physikinstrumente.com/en/products/error_productsFWD.php.

Piazza, G., Stephanou, P. J. & Pisano, A. P. (2006) Piezoelectric aluminum nitride vibrating contour-mode MEMS resonators. *J. Microelectromech. Syst.*, 15, 1406-1418.

Bibliography

- Rabe, U., Amelio, S., Kopycinska, M., Hirsekorn, S., Kempf, M., Göken, M. & Arnold, W. (2002) Imaging and measurement of local mechanical material properties by atomic force acoustic microscopy. *Surf. Interface Anal.*, 33, 65-70.
- Rayleigh, L. (1885) On waves propagated along the plane surface of an elastic solid. *Proceedings of the London Mathematical Society*, 1, 4-11.
- Robbins, W. P. & Rudd, E. P. (1988) Measurement of surface acoustic wave slowness curves with a scanning laser acoustic microscope. *J. Appl. Phys.*, 64, 1040-1043.
- Roshchupkin, D. V., Brunel, M., Tucoulou, R., Bigler, E. & Sorokin, N. G. (1994) Reflection of surface acoustic waves on domain walls in a LiNbO₃ crystal. *Appl. Phys. Lett.*, 64, 164-165.
- Rouquette, J., Haines, J., Bornand, V., Pintard, M., Papet, P. & Sauvajol, J. L. (2006) Use of resonance Raman spectroscopy to study the phase diagram of PbZr_{0.52}Ti_{0.48}O₃. *Phys. Rev. B*, 73, 224118.
- Sasaki, Y., Endo, T., Yamagishi, T. & Sakai, M. (1992) Thickness measurement of a thin-film layer on an anisotropic substrate by phase-sensitive acoustic microscope. *Ultrasonics, Ferroelectrics and Frequency Control, IEEE Transactions on*, 39, 638-642.
- Shelke, A., Habib, A., Amjad, U., Pluta, M., Kundu, T., Pietsch, U. & Grill, W. (2011a) Metamorphosis of bulk waves to Lamb waves in anisotropic piezoelectric crystals. In: *SPIE*.
- Shelke, A., Kundu, T., Amjad, U., Hahn, K. & Grill, W. (2011b) Mode-selective excitation and detection of ultrasonic guided waves for delamination detection in laminated aluminum plates. *IEEE Trans. Ultrason. Ferroelectr. Freq. Control.*, 58, 567-577.
- Sklar, Z., Briggs, G., Cawley, P. & Kinloch, A. (1995) Quantitative acoustic microscopy of anodized and coated aluminium at frequencies up to 1 GHz. *J. Mater. Sci.*, 30, 3752-3760.
- Slobodnik, A. J. (1973) *Microwave Acoustics Handbook. Surface Wave Velocities*, DTIC Document.

Bibliography

Smith, I. R. & Wickramasinghe, H. K. (1982) SAW attenuation measurement in the acoustic microscope. *Electron. Lett*, 18, 955-956.

Sokolov, S. Y. (1949) The Ultrasonic microscope. *Dokl. Akad. Nauk.SSSR*, 64, 333-335.

Sugawara, Y., Wright, O., Matsuda, O., Takigahira, M., Tanaka, Y., Tamura, S. & Gusev, V. (2002) Watching ripples on crystals. *Phys. Rev. Lett.*, 88, 185504.

Thokala, R. & Chaudhuri, J. (1995) Calculated elastic constants of wide band gap semiconductor thin films with a hexagonal crystal structure for stress problems. *Thin Solid Films*, 266, 189-191.

Tsui, T. Y. & Pharr, G. M. (1999) Substrate effects on nanoindentation mechanical property measurement of soft films on hard substrates. *J. Mater. Res.*, 14, 292-301.

Twerdowski, E. (2007) Ultrasonic transmission and holographic imaging in anisotropic media. In: *Faculty of Physics and Earth Sciences*. University of Leipzig, Leipzig.

Twerdowski, E., Wannemacher, R., Razek, N., Schindler, A. & Grill, W. (2006) Application of spatially and temporally apodized non-confocal acoustic transmission microscopy to imaging of directly bonded wafers. *Ultrasonics*, 44, 54-63.

Vines, R., Tamura, S. & Wolfe, J. (1995) Surface acoustic wave focusing and induced Rayleigh waves. *Phys. Rev. Lett.*, 74, 2729-2732.

Wang, J. S. & Lakin, K. M. (1982) Low temperature coefficient bulk acoustic wave composite resonators. *Appl. Phys. Lett.*, 40, 308-310.

Wang, Z., Zhu, W., Zhu, H., Miao, J., Chao, C., Zhao, C. & Tan, O. K. (2005) Fabrication and characterization of piezoelectric micromachined ultrasonic transducers with thick composite PZT films. *IEEE Trans. Ultrason. Ferroelectr. Freq. Control.*, 52, 2289-2297.

Weglein, R. D. (1979) A model for predicting acoustic material signatures. *Appl. Phys. Lett.*, 34, 179-181.

Whatmore, R., Goddard, P., Tanner, B. & Clark, G. (1982) Direct imaging of travelling Rayleigh waves by stroboscopic X-ray topography. *Nature*, 299, 44-46.

Bibliography

White, R. M. & Voltmer, F. W. (1965) Direct piezoelectric coupling to surface elastic waves. *Appl. Phys. Lett.*, 7, 314-316.

Wolfe, J. P. (1998) *Imaging phonons: acoustic wave propagation in solids*, Cambridge Univ Pr.

Yonenaga, I., Shima, T. & Sluiter, M. H. F. (2002) Nano-indentation hardness and elastic moduli of bulk single-crystal AlN. *Jpn. J. Appl. Phys.*, 41, 4620-4621.

Yu, G. (2001) Properties of Advanced Semiconductor Materials GaN, AlN, InN, BN, SiC, SiGe. (eds. M. E. Levinshteĭn, S. L. Rumyantsev & M. Shur). John Wiley & Sons, Inc., New York.

Eidesstattliche Erklärung

Eidesstattliche Erklärung

Ich versichere hiermit an Eides statt, dass ich die vorliegende Arbeit ohne fremde Hilfe und ohne Benutzung anderer als der angegebenen Hilfsmittel angefertigt habe. Alle Ausführungen, die wortlich oder sinngemäß aus fremden Quellen übernommen wurden sind als solche gekennzeichnet. Die Arbeit wurde bisher in gleicher oder ähnlicher Form noch keiner anderen Jury vorgelegt und wird noch nicht kommerziell genutzt.

Ich bin bewusst dass eine falsche Erklärung den Ausschluss aus dem verfahren zur Folge haben wird.

Siegen, 27.03.2013

Ort, Datum

Unterschrift